Applications of Synthetic Aperture Radar (SAR)/ SAR Interferometry (InSAR) for Monitoring of Wetland Water Level and Land Subsidence

by

Jin Woo Kim

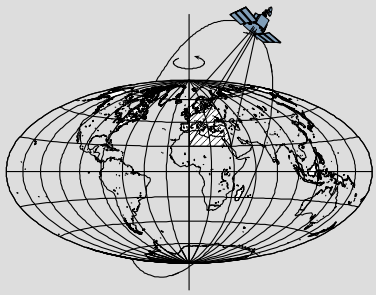

Report No. 503

Geodetic Science

The Ohio State University
Columbus, Ohio 43210

August 2013

Applications of Synthetic Aperture Radar (SAR)/ SAR Interferometry (InSAR) for Monitoring of Wetland Water Level and Land Subsidence

by

Jin Woo Kim

Report No. 503

Geodetic Science

The Ohio State University

Columbus, Ohio 43210

August 2013

Preface

This report was prepared for and submitted to the Graduate School of the Ohio State University as a dissertation in partial fulfillment of the requirements for the PhD degree.

This research is conducted under the supervision of Professor C.K. Shum, Division of Geodetic Science, School of Earth Sciences, The Ohio State University. This research is primarily supported by NASA's Earth and Space Science Fellowship (NESSF, No. NNX10AN54H), and by grants from National Geospatial-Intelligence Agency's (NGA's) University Research Initiatives (NURI) Program (HM1582-07-1-2024 and HM1582-10-BAA-0002), the United States Geological Survey (G12AC20468), NASA Geodetic Imaging Program (NNX12AQ07G), and the Ohio State University's Climate, Water and Carbon program.

Abstract

Development of coastal wetlands and arid areas had negative impacts on the natural hydrological processing on the surface and underground, and it resulted in disappearance of wetlands that buffer severe flooding and function as home for various wildlife in the wetlands, and groundwater depletion in the desert areas. Continuously monitoring the surface change caused by human activities requires radar remote sensing with the in-situ measurements. The intensity and phase components of Synthetic Aperture Radar (SAR) data provide valuable information on the characteristics of surface change and ground deformation. First of all, in this study, we demonstrated that the wetland water level changes in the Atchafalaya Basin of the Louisiana can be effectively observed by integrating Interferometric SAR (InSAR) results and radar altimetry data. When the hydrologic flow between wetlands is disrupted by levees or dams, InSAR processing cannot appropriately resolve the absolute water level changes from unwrapped phases. The fusion of the two radar technologies enables one to accurately estimate absolute water level change while avoiding inconsistent phase unwrapping. Secondly, the water level in the Everglades is measured by monitoring stations, and the measurement is often disturbed by abrupt water level rise. The L-band SAR backscatter coefficient in Everglades has the characteristics that SAR intensity is inversely proportional with water level in the freshwater marsh. The linear relationship enables one to estimate water level from SAR backscattering coefficients. The correlation between two parameters over the sawgrass was high, and it implied that water level estimation from the ALOS L-band SAR backscatter coefficients is possible. The final study demonstrated the use of small baseline subset (SBAS) InSAR processing technique to effectively measure the ground subsidence caused by groundwater depletion in Tucson, Arizona. The SBAS processing suppresses atmospheric artifacts affected by turbulent mixing that appears random in time and space and estimates topographic error terms from multiple InSAR pairs. The SBAS InSAR-derived vertical deformation gives information on the spatial extent and magnitude of subsidence. The groundwater level decrease of tens of meter caused the ground subsidence of tens of centimeters over a 17-years time period. InSAR results indicate that the subsidence has recently slowed down possibly due to the artificial recharge of water into surrounding aquifers near Tucson, Arizona.

Table of Contents

CHAPTER 1: Introduction

1.1 Radar remote sensing

Remote sensing is the acquisition of information about physical properties and phenomena without making any physical contacts. The remote sensing is classified into passive and active remote sensing, and the passive sensors detect microwave, visible, and infrared signals emitted from earth surface. The aerial photography, optical satellite, and passive microwave satellite are included in a device for passive remote sensing. The sensors for active remote sensing transmits microwave or laser signal toward a target, and the sensors detect the radiation reflected or backscattered from a target or measure a time delay related to distance between a sensor and a target. Data from passive sensors have been used for various applications of creating orthographic maps, classifying the types of land surface, detecting the effect of global warming in Arctic region, and monitoring inundated areas in low-lying region of deltas or seasonally flooded basins. However, the obstacle for more extensive application of passive remote sensing is that its observation is depending on the existence of light during days and cloud blocks the signals emitted from the land surface. If the sensor is not designed for weather forecasting, a large amount of optical satellite data covered by clouds is not appropriate for applications in many fields. In contrast to passive remote sensing, the microwave sensors of Synthetic Aperture Radar (SAR) are not affected or less affected by light and weather condition. The radar remote sensing includes from high resolution and large coverage of SAR to accurate point-wise measurements on the sea surface by radar geometry. In particular, SAR usually uses the microwave bandwidth of X-, C-, L-, and P-band, and, due to the characteristics of long wavelength, the microwave signal of SAR is relatively less influenced by exterior conditions. SAR data have been applied to imaging land surface on Earth, Moon, or Venus, detecting seasonally inundated areas beneath dense canopy in tropical region of the Amazon, Louisiana, and Congo, estimating the spatial extent flooded by abrupt water level change, and classifying land types of vegetation, urban, and agriculture.

1.2 Synthetic Aperture Radar

A SAR is advanced radar system that utilizes image processing techniques to synthesize a large virtual antenna, which provides much higher spatial resolution than is practical using a real-aperture radar (Curlander and McDonough, 1991). A SAR system transmits electromagnetic waves at a wavelength that can range from a few millimeter to tens of centimeters. Because a SAR system actively transmits and receives signals backscattered from the target area and the radar signals with long wavelengths are mostly unaffected by weather or clouds, a SAR can operate effectively during day and night and under most weather conditions.

A chirp signal, in which the frequency is linearly modulated, is used for SAR processing, because a large bandwidth in range-time domain highly improves a range resolution and signal-to-noise ratio (SNR). Transmitted chirp signal ($s(t)$) has the form of Equation (1.1):

$$s(t) = rect(\tfrac{t}{T}) \cdot \exp\{2\pi f_0 t + \pi k t^2\} \tag{1.1}$$

where *rect* is a rectangular function, T is pulse duration, t is range-time variable (seconds), f_0 is a center frequency of radar sensor (Hz), and k is a chirp slope. Because a chirp signal cannot be infinite in range-time domain, a windowed pulse is used and chirp bandwidth (range bandwidth) is defined by chirp slope and pulse duration. The sampling frequency should be larger than the chirp bandwidth to avoid aliasing, and the chirp bandwidth is directly proportional to range resolution. Doppler bandwidth and related signal processing in the azimuth direction of synthetic aperture radar is a key factor to improve azimuth resolution into approximately half length of antenna without utilizing a physically large antenna of a real aperture radar, resolution of which is proportional to the size of antenna.

$$(\delta_{az})_{\max} = \frac{L_{az}}{2} \tag{1.2}$$

where $(\delta_{az})_{\max}$ is a maximum azimuth resolution, and L_{az} is an antenna length in azimuth direction. The maximum azimuth resolution (see Equation 1.2) is the highest available resolution through Doppler processing in azimuth-time and Doppler domain. After the transmitted chirp signals are backscattered toward an antenna, the radar pulse is affected by time delay and the conversion from a raw signal to images requires SAR signal processing in range and azimuth direction. The SAR processing includes several steps to compress and filter the radar signal, and the Range-Doppler and chirp scaling algorithm is the most popular processor. The Range-Doppler algorithm (RDA) is generally used in the commercial or freeware SAR processing software, because each processing step is straightforward, range migration compensation is relatively facile in range and Doppler domain, and the steps can be easily modified for better implementation. The first step of RDA is a range compression by using a matched filter ($s_{out}(t)$) in range direction, while calculating correlation by multiplying original signal with a conjugate of estimated signal (reference function) in frequency domain.

$$s_{out}(t) = \int_{-\infty}^{\infty} s_r(u) g^*(u-t)\, du \tag{1.3}$$

where s_r is the received signal and *g(t)* is reference function estimated from original radar signal and its phase delay. Equation 1.3 is the matched filter operation, corresponding to convolution of received signal and conjugate of reference function. The matched filter in Equation 1.3 can be easily implemented as multiplication in frequency

domain. And then, a range-migration is compensated from range-compressed signals, because each point follows a parabolic range trajectory. Doppler centroid at the point closest to a target is estimated from returned signal, because the antenna beam is tilted in most cases and the Doppler centroid is non-zero. Azimuth spectrum is at a peak around Doppler centroid, and estimated Doppler centroid and pulse repetition frequency (PRF) as Doppler bandwidth are used for azimuth compression in a similar way like a range compression. The PRF is an important parameter for SAR processing. The PRF functioning as sampling frequency in azimuth-time domain should be larger than azimuth signal bandwidth to avoid aliasing, and should be small to avoid range ambiguity. After the received signal is processed by range-compression, range migration compression, and azimuth compression, the baseband signal $s_0(\tau,\eta)$ from a single point target in two dimension of range time and azimuth time domain becomes the following complex signal,

$$\begin{aligned} s_0(\tau,\eta) &= w_r(\tau - 2R(\eta)/c)\cdot w_a(\eta-\eta_c) \\ &\quad \times \exp\{-j\,4\pi f_0 R(\eta)/c\}\cdot\exp\{j\pi k(\tau-2R(\eta)/c)^2\} \end{aligned} \tag{1.4}$$

where w_r is the window function for range-time domain, w_a is the window function for azimuth time domain, τ is range-time, η is azimuth-time, c is the light velocity, η_c is the azimuth time at the center of beamwidth, f_0 is center frequency of SAR platform, and k is the chirp slope (Cumming and Wong, 2005). The azimuth compressed signal corresponding to Equation 1.4 is the final product of SAR image, and both the intensity and phase of the radar signal backscatter from ground resolution element is combined into a complex-valued SAR image that represents the radar reflectivity of the ground surface (Curlander and McDonough, 1991; Cumming and Wong, 2005). The intensity of the SAR image is corresponding to the terrain slope, surface roughness, and dielectric constant in the land surface, and the phase of the SAR image is related to the apparent distance from satellite to ground resolution elements as well as the interaction between radar waves and scatterers within resolution element of the imaged area.

1.3 SAR Interferometry

InSAR uses the phase components of co-registered SAR images of the same area to estimate the topography and measure the surface change in the hazard area of earthquake and volcano. Also, InSAR is useful for identifying anthropologic deformation caused by mining and oil/gas extraction, and deformation by melting of permafrost. The multiplication of a single look complex (SLC) data in the first date and a conjugate of SLC data in the other acquisition date generates an interferogram, which contains topographic, atmospheric effect, baseline error, and noise components.

$$\phi_{ifgs} = \phi_{topo} + \phi_{def} + \phi_{baseline} + \phi_{atm} + \phi_{noise} \tag{1.5}$$

where ϕ_{ifgs} is an observed interferometric phase, ϕ_{topo} is topographic phase, $\phi_{baseline}$ is a baseline error phase, ϕ_{atm} is an atmospheric phase, and ϕ_{noise} is a noise phase. Removing other phase components except deformation phase is called, differential InSAR (DInSAR) processing. Topographic phase is removed by other available elevation sources, and elevation data with small grid is preferred. 1-arcsec Shuttle Radar Topography Mission (SRTM) or National Elevation Dataset (NED) for USA territories and 3-arcsec SRTM or 1-arcsec Advanced Spaceborne Thermal Emission and Reflection (ASTER) GDEM outside the USA is generally utilized. In some cases, Uninhabited Aerial Vehicle Synthetic Aperture Radar (UAVSAR)-derived DEM or LiDAR DEM can be used for DInSAR processing over vegetated area, arctic region, or mountains. When the sufficient SAR data acquired by tandem mission or a single-pass SAR observation is available, the subtraction of two sets of SAR observation can represent temporal deformation with high resolution. The orbit information is important for estimating a perpendicular baseline from InSAR pair, and the perpendicular baseline is used for image co-registration and removing the components of flat earth phase. Because the orbit information of European Remote Sensing Satellite (ERS) and Environmental Satellite (ENVISAT) is not accurate enough, supplemental precise orbit is being provided by Delft Institute for Earth-Oriented Space research (DEOS) and other research institutes such as DeutschesGeoForschungsZentrum Potsdam (GFZ Potsdam). In case of Radarsat or ALOS PALSAR, the operating space agencies of Japan Aerospace Exploration Agency (JAXA) and MacDonald Dettwiler and Associates (MDA) claim that the orbit information is sufficiently accurate. Unfortunately, most operated SAR sensors do not have high-accuracy of orbit information, even after precise orbit data have been applied to InSAR processing. The inaccuracy of estimating a perpendicular baseline from coordinates of the satellite at the specific time leads into inappropriate removal of flat earth phase. The baseline error phases exist as the form of 1^{st} or 2^{nd} order polynomials in an interferogram, and a least square adjustment is used for removing residual phases. Recent satellite data like TerraSAR-X has much improved orbital accuracy due to better GPS and clocks, and the baseline error term of an interferogram is not prominent. Figure 1.1 and 1.2 describes the DInSAR processing to obtain deformation phases from an interferogram. The InSAR pair is acquired by ENVISAT Advanced SAR (ASAR), and Figure 1.1 is corresponding to removing the components of topographic phase and baseline error. And, Figure 1.2 is wrapped differential interferogram as an output by DInSAR processing.

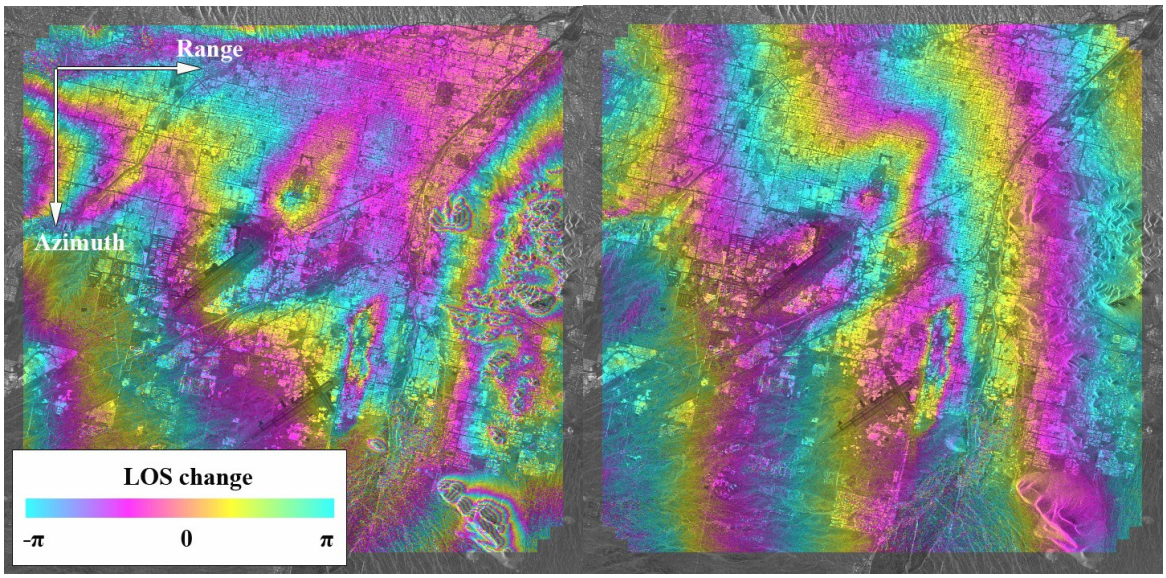

Figure 1.1. Interferogram from a single ENVISAT InSAR pair, and each fringe is colored by the cycle of –π to π. (Left) Because topographic phase was not removed, phase components in the interferogram are in the mix of topographic, atmospheric deformation, and noise terms. (Right) After topographic phase is removed by using 1-arcsec SRTM, the phase related to baseline error is still remaining and least-square adjustment is used for removing in accurate flat earth phase.

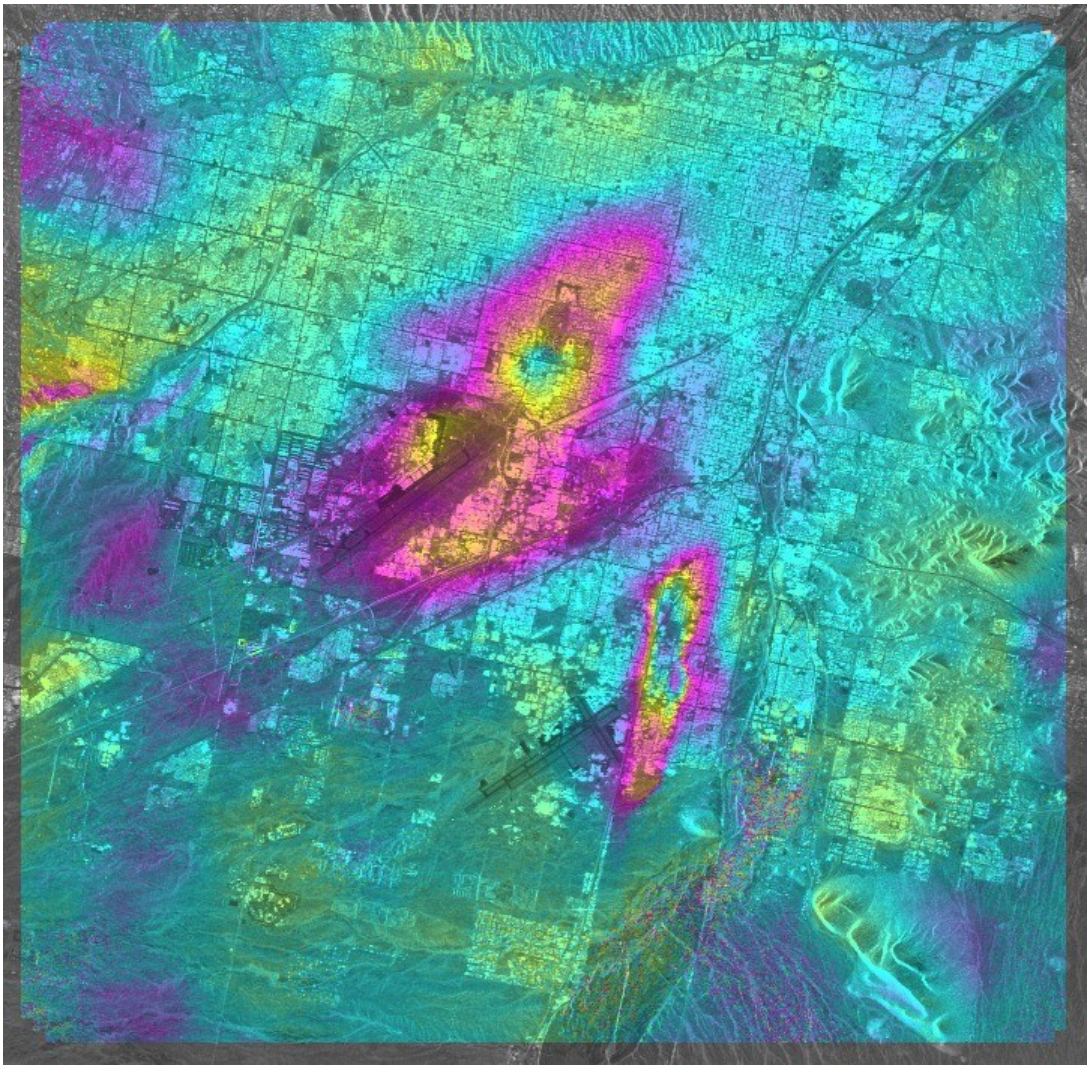

Figure 1.2. Differential interferogram including deformation phase. After topographic phase and baseline error phase are removed from an interferogram, deformation phase due to ground subsidence is remaining. The color scale is identical with Figure 1.1.

The components of atmospheric phase term is critical for InSAR processing, because the phase term can add the estimated subsidence as much as several centimeters. The phase term is classified into turbulent mixing and vertical stratification contributions (Hanssen, 2001). The vertical stratification is expressed as a linearly variant fringe proportional to elevation. A simple linear regression between elevation and the phase components enables to reduce the phase term related to vertical stratification. The vertical stratification can exist in most SAR pairs with C-, X-, or L-band. The turbulent mixing is represented as a random phase of interferograms in time and space, and temporal and spatial smoothing filters can help to reduce the turbulent mixing. Specially, SBAS InSAR or PSInSAR is great for reducing the atmospheric effect from interfergrams, because

multiple InSAR pairs with large dataset of long time span enable to identify the atmospheric phase and suppress its effect. To some researchers, the atmospheric phase can be a concern, and the comparison of SAR interferogram and GPS signal can give a clue on the distribution of ionosphere and troposphere at the specific time. However, many researchers want to detect temporal deformation by natural hazards or human activities without any unnecessary effects. The noise can be suppressed by adaptive filtering (Goldstein and Werner, 1998) and multi-looking, and wrapped differential interferogram in Figure 1.2 is smoothed interferogram by two filters. Two images in Figure 1.3 show the difference between before and after smoothing. The multi-looking can be practiced by moving average filter with window size that makes each pixel become a square considering radar geometry. The Goldstein adaptive filter (Goldstein and Werner, 1998) is implemented by using the response of the adaptive filter *H(u,v)*. Two-dimensional FFT of the complex form of interferogram and its absolute value generates the power spectrum for each patch with window size a power of 2.

$$H(u,v) = \left|Z(u,v)\right|^{\alpha} \qquad (1.6)$$

where H is the power spectrum, u and v are frequency domain in range and azimuth direction, and α is a smoothing parameter. The multiplication of the power spectrum (H) and spectrum of the original interferogram in the frequency domain and its inverse two-dimensional Fourier transform generates the smoothed interferogram (see Figure 1.3).

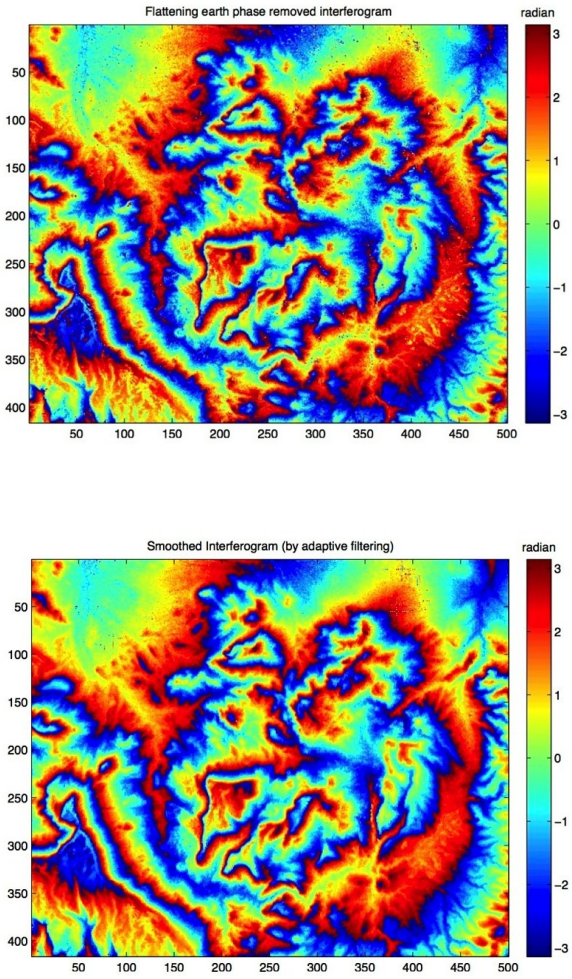

Figure 1.3. (Top) Wrapped interferogram before smoothing. (Bottom) Wraaped interferogram after smoothing. The smoothing was applied by Goldstein adaptive filtering.

In Figure 1.3, the upper image is the original interferogram before smoothing, and lower image is interferogram smoothed by the adaptive filter. As shown in two figures, much noise in the interferogram disappeared as a result of filtering. Therefore, the adaptive filtering has been generally used for suppressing low coherence and reducing noise in an interferogram. As the window size and smoothing parameter is large, the effect of filtering becomes strong. On the other hand, it can cause the loss of many meaningful detailed phases in an interferogram. The choice of window size and smoothing parameter is important for obtaining reliable interferogram.

The noticeable advantage of InSAR is that it can utilize multiple mode data from fine-beam (or stripmap) or ScanSAR mode. Usually, InSAR uses fine-beam mode data for getting more detailed information over a land surface. Instead, ScanSAR mode data can help to fill up temporal gaps between acquisitions, and its large coverage enables to

monitor inundated areas over a huge river basin like the Amazon basin. Because ScanSAR mode acquires the data in a sequence with gaps to cover large areas, the gaps between bursts should be filled with zero padding. Then, a similar method (full-aperture algorithm) to process a stripmap is applied to the zero-padded ScanSAR data, and then ScanSAR SLC image can be generated. The ScanSAR data is useful for ScanSAR-ScanSAR (see Figure 1.4) or ScanSAR-stripmap interferometry (see Figure 1.5), while calculating interferometric phases from ScanSAR and stripmap data.

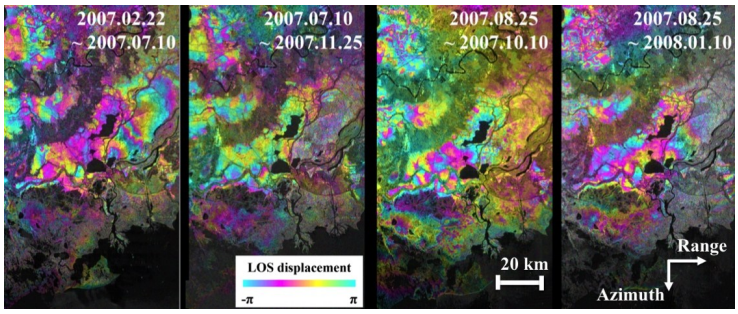

Figure 1.4. ALOS PALSAR ScanSAR-ScanSAR interferograms (in radar geometry) over Louisiana wetland.

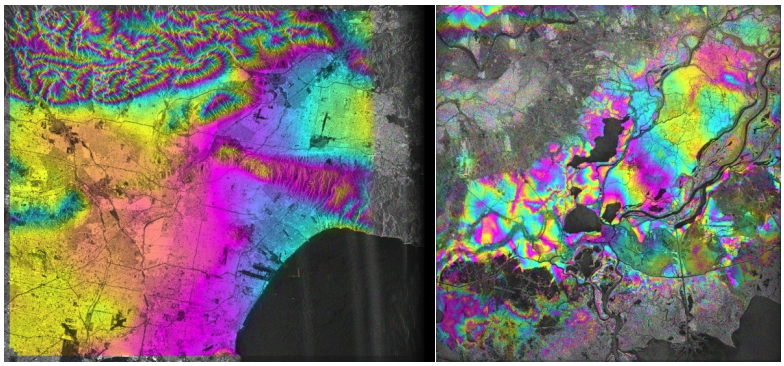
Figure 1.5. ALOS PALSAR ScanSAR-stripmap interferogram over Los Angeles (left) and Louisiana (right). The color scale is same as Figure 1.4.

The phase unwrapping is necessary to reconstruct the actual phases, because the interferometric phases from differential interferogram is only known modulo 2π. The phase unwrapping can be problematic in low coherence areas, because discontinuities and inconsistencies cause a wrong estimation of an integer fraction. Such problems are represented as phase jumps exceeding 2π difference with nearby pixels. Therefore, low coherence areas are masked out or smoothed by a strong filtering. The phase unwrapping is often implemented by a branch-cut region growing algorithm or minimum cost flow (MCF) techniques, and final unwrapped interferograms should be carefully checked to avoid inconsistencies. Figure 1.6 is an unwrapped interferogram processed by the MCF algorithm, and each fringe on the left image corresponds to the LOS change due to Tohoku earthquake. Phase unwrapping is a final step to estimate vertical or horizontal deformation. Unwrapped phase on right image of Figure 1.6 corresponds to hydrography (elevation) of land surface.

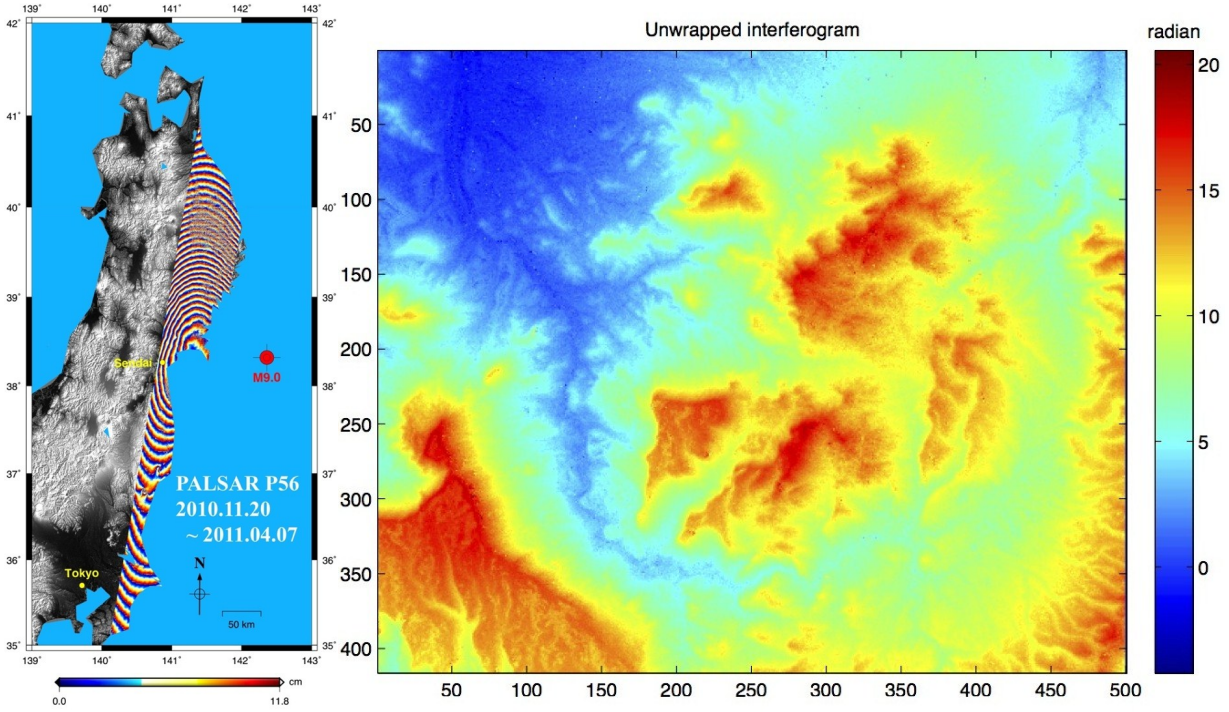

Figure 1.6. Unwrapped PALSAR interferogram. (Left) The fringes, where are colored by the cycle of 11.8 cm represents the deformation in line-of-sight (LOS) direction, which was caused by M9.0 magnitude of earthquake in Tohoku. (Right) Unwrapped interferograms. The unwrapped phases correspond to the topography of land surface.

1.4 SAR and InSAR application

The use of SAR data depends on the characteristics of the intensity, which can be converted into backscatter coefficient that reflects the terrain slope, moisture, and roughness in the ground surface and scattering mechanism between radar signal and objects within resolution element. The SAR can be used for various purposes, military purpose (reconnaissance, surveillance, and targeting), vegetation monitoring, change detection and land classification, environmental monitoring on ocean surfaces and agriculture, and interferometry.

Due to the characteristics of all-weather and day-and-night observing sensor, SAR can provide high resolution to identify terrain features and military targets of tanks, airports, and missile launch pads. Usually, high-frequency SAR sensor is used for obtaining high-resolution images, and the sensor is installed on airplane or satellites. The vegetation monitoring depends on the scattering mechanism of SAR signal. The scattering mechanism on the forests is not dominated by a single type, but mixed with multiple mechanisms. The major scattering mechanism is surface, volume, and double-bounce scattering. The surface scattering occurs in the bare earth or canopy top in forested region, and volume scattering takes a place inside the vegetation. The double-bounce scattering is a phenomenon that a signal is doubly bounced from land surface and erected objects, and the tree trunks in vegetation or buildings in the urban region function as a corner reflector. The polarization of electromagnetic waves makes difference in the response between microwave signals and forest structure. Therefore, SAR images of different polarization of HH, HV, VV, and VH creates different backscatter coefficient over forested areas.

Based on backscatter coefficient, the classification of land type is available. The scattering mechanism differently occurs in distinct objects and targets. The change detection using SAR images includes speckle tracking method to measure offsets between two SAR intensity images from calculated correlation. Speckle tracking method is very similar to image matching of optical images like aerial photography or Landsat (see Figure 1.7).

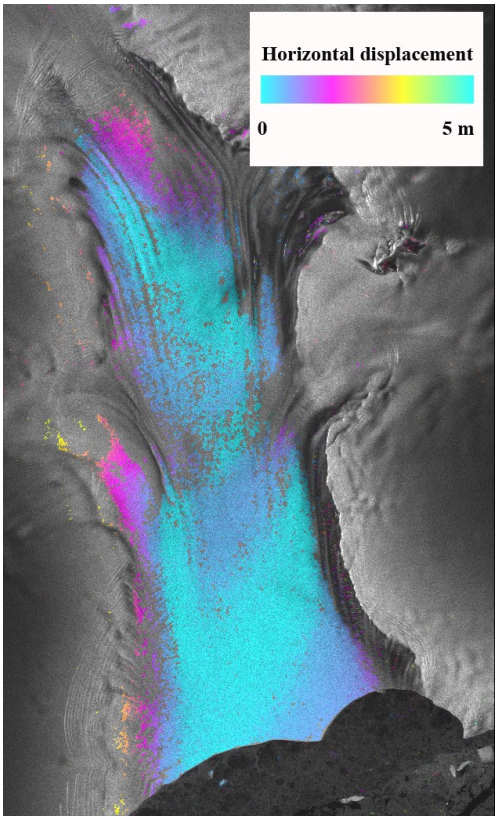

Figure 1.7. Horizontal displacement using speckle matching algorithm over ice stream in the Antarctica.

In Figure 1.7, the offsets between two SAR intensities are induced by ice stream flow. Also, the change detection in forested region is possible by distinguishing backscatter coefficients by different scattering algorithm. The double-bounce scattering is important for classifying flooded and non-flooded areas from SAR intensity data. The flooded forest areas have high backscattering coefficient and the flooded region looks bright. Also, tree height is another factor, and a tall tree is required for double-bounce scattering. A sawgrass with a short height is not a good medium for the scattering mechanism. Scattering in open water is also important for classifying SAR intensity data. In open water, the radar signal is bounced off the water surface, and returned signal is very weak. It means that areas with open water have a small backscattering coefficient and the area looks dark in the SAR scenes. Therefore, areas with small backscatter coefficient except shadow by radar geometry are classified into flooded regions, rivers, lakes, or oceans. Figure 1.8 and 1.9 is an example for describing the change of SAR intensity data by abrupt natural hazard. Tsunami hit the Sendai city in the Japan, and many areas were submerged and damaged. When backscattering coefficient was decreased, the region is inundated by open water. Red-colored region in right image of Figure 1.9 indicated the spatial extent of submerged region using TerraSAR-X intensity data. When forest areas are inundated by severe flooding, the SAR intensity is dominated by double-bounce

scattering and the region can be identified as inundated areas. In Figure 1.10, blue-colored region is classified as open water of river or lakes, and green-colored region represents submerged area in the inland. Due to the severe flooding in the Amazon Basin, the run-off from increased river causes the inundation of inland forests.

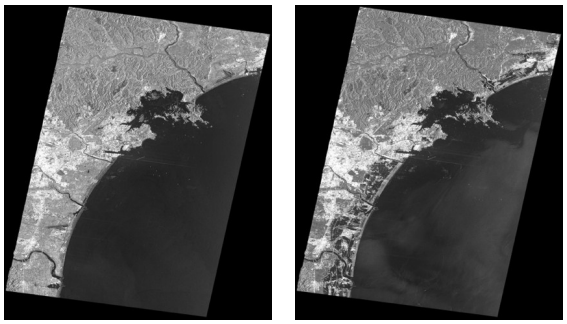

Figure 1.8. TerraSAR-X intensity data over Sendai City, Japan. (Top) Intensity data before Tsunami (2010.10.20). (Bottom) Intensity data after Tsunami (2011.03.12).

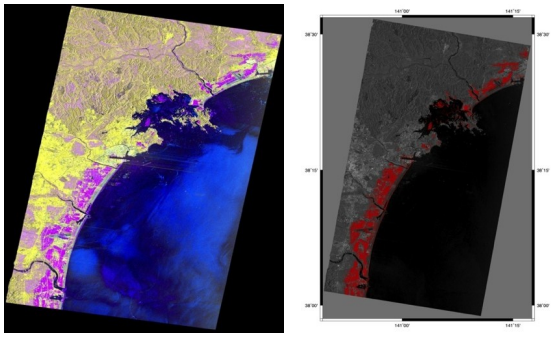

Figure 1.9. (Left) RGB difference map of two TerraSAR-X intensity data before and after tsunami in Figure 1.8. Purple-colored region represents decreased backscatter coefficient by flooding. (Right) The red areas are Tsunami damaged region.

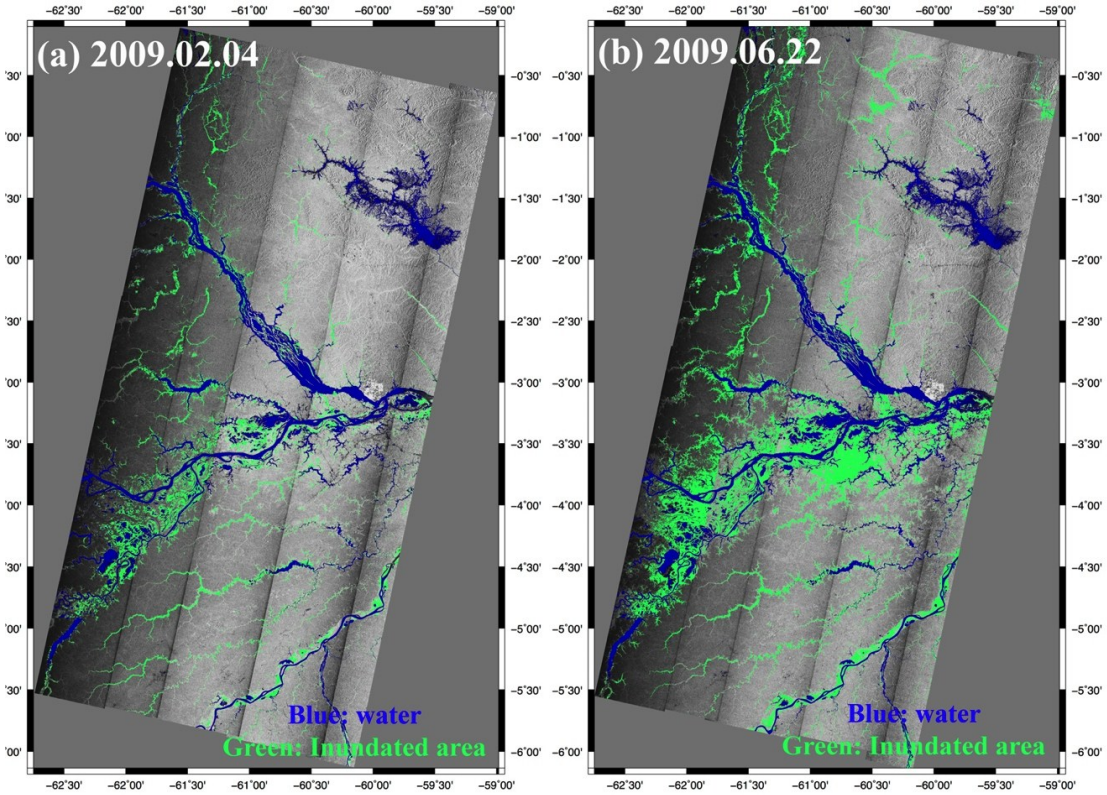

Figure 1.10. Inundation map over the Amazon Basin around the confluence of Solimoes and Negro River, which are estimated from classification of ALOS PALSAR ScanSAR imagery. Blue colored region is water and green represents the inundated wetland. (a) Inundated regions in 2009.02.04 (low water) and (b) in 2009.06.22 (severe flooding).

The SAR intensity image can be used for a wide variety of environmental application on the ocean surface and agriculture. Oil spills can be detected in SAR imagery because the oil changes the backscatter characteristics. Radar backscatter from the ocean results primarily from capillary waves through what is known as Bragg scattering (constructive interference from the capillary waves being close to the same wavelength as the SAR). The presence of oil dampens the capillary waves, thereby decreasing the radar backscatter. Thus, oil slicks appear dark in SAR images relative to oil-free areas (Sandia National Laboratories http://www.sandia.gov/radar/sarapps.html). In Figure 1.11 shows oil slick detected by ALOS PALSAR ScanSAR imagery, and the oil slick appears darker than other oil-free ocean surfaces (see Figure 1.11 and 1.12).

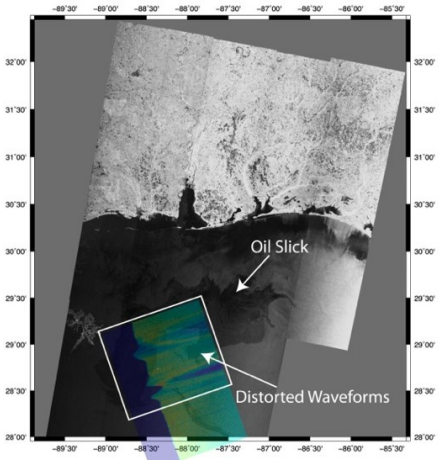

Figure 1.11. Oil slick detected by ALOS PALSAR ScanSAR image, and the oil slick looks darker than other oil-free ocean surfaces.

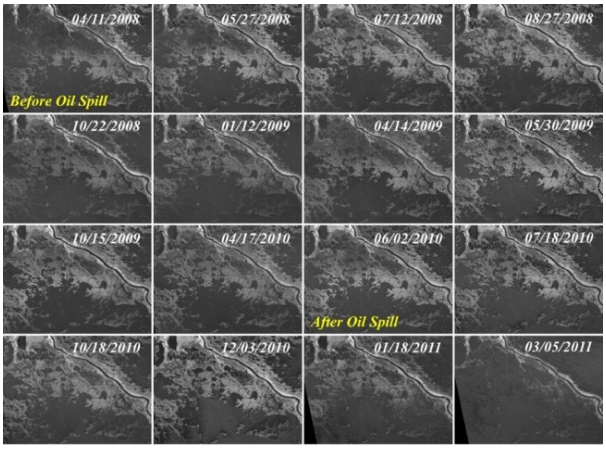

Figure 1.12. Oil slick monitoring around coastal wetlands by using ALOS PALSAR imagery.

Unlike the applications of SAR, the InSAR is using the phase signature related to the apparent distance between a platform of a satellite and airplane and a ground element. The InSAR application includes to measure tectonic deformation of earthquakes, detect volcanic deformation with eruptions, measuring ground subsidence caused by oil and water extraction from subsurface, estimate the velocity of ice stream flow, and generating digital elevation model such as SRTM. When using InSAR for various purposes, interferometric coherence is one of the most important parameter. Coherence is a qualitative assessment of correlation of SAR images acquired at different times. It determines the amount of phase error and the accuracy of deformation estimates or DEM products. Constructing a coherent interferogram requires that SAR images should correlated with each other (Lu, 2007). High coherence means that scattering

characteristics between two SAR acquisitions were not changed, and reliable estimation of deformation from InSAR products needs high coherence. Also, coherence itself can give valuable information on the vegetation type or land types. For example, coherence over urban regions lasts for a several years, but vegetated areas lose coherence within a few days or few years. Loss of coherence is referred to decorrelation. There are three primary sources of decorrelation, (a) thermal decorrelation, caused by the presence of uncorrelated noise sources in radar instruments, (b) spatial decorrelation, which results when the target is viewed from different positions, and (c) temporal decorrelation, which is due to environmental changes such as vegetation and snow (Lu, 2007). The coherence is the biggest obstacle for InSAR processing, and the decorrelated interferogram is often masked out. Also, the Goldstein adaptive filter can be used to suppress low coherence to avoid decorrelation. On the other hand, most decorrelation cannot be avoided and the persistent scatterer InSAR (PSInSAR) or small baseline subset (SBAS) InSAR, which is utilizing the only high coherent pixels, is recently emerging as the future of InSAR. Unlike conventional InSAR, the PSInSAR relies on utilizing pixels, which remain coherent over a sequence of interferogram. The stack of interferogram is used for estimating topographic phase and atmospheric artifacts, and measuring point-wise temporal deformation (see Figure 1.13). The advantage of PSInSAR is that it is independent of a large perpendicular baseline and temporal decorrelation while picking only high coherence pixels. The disadvantage of PSInSAR is that the high density of high coherent pixels is required for reliable phase unwrapping, and most high coherent pixels are from objects constructed by human, such as roads or buildings, while losing coherence over forest regions or mountains with high slope.

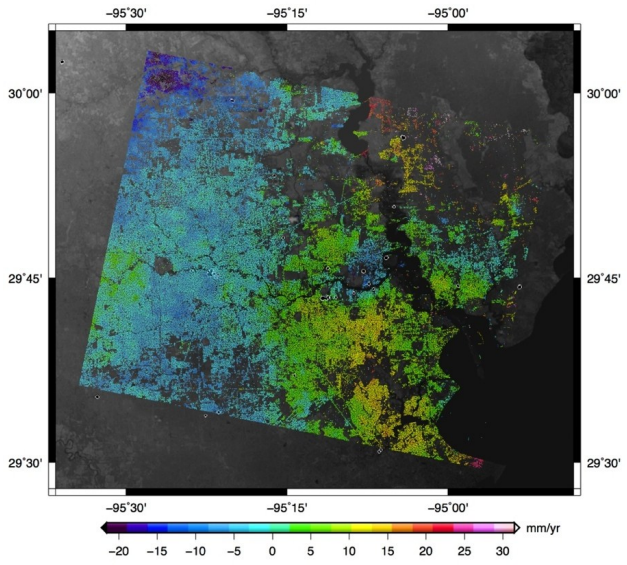

Figure 1.13. Deformation rate over Houston metropolitan areas using PSInSAR.

1.5 Problem definition and motivation of this study

This study focuses on two different regions of coastal wetlands and arid areas. Coastal wetlands contain sufficient surface water to sustain ecological system and supply water to nearby residents, but in arid areas like a desert, the surface water is disappearing and the municipal, agricultural, and industrial use of water is depending on groundwater extraction from the subsurface. The common thing between wetlands and arid areas is that human activities have disturbed the natural ecological and hydrological processing, and human′s negative impacts on the nature forced state or federal government to recover the original hydrological flow. The dam or levees were constructed in Louisiana and Florida wetlands, and the natural water flow was disrupted by the human structures. The ecology related to wetlands has been altered, and the inland water has been disappeared. In the Everglades, where originally sawgrass was dominant species, other vegetation prospered by using fertilizers in the agricultural field. In the Louisiana wetland, the careful management of hydrological flow between wetlands has been required to prevent the excessive water or drought in the inland wetlands. In arid areas of Arizona desert, the urban and agricultural field development needed the extreme demand for drinking water and irrigation. Due to the lack of surface water, the demand was met by the groundwater depletion, and the groundwater has been historically disappeared. In the southern Arizona, sink holes, cracks on the buildings, and earth fissures occurred in residential areas and roads.

The difference between coastal wetland and arid areas is that coastal wetland is vulnerable to sea level rising as a result of global warming and occasional severe storm surge and flooding events, but arid area is not subject to the same threat. The coastal wetland is functioning as the buffer against heavy rains or hurricanes, but the function became weak due to disappearance of coastal wetlands. Sea level rise inundated the saline marsh beyond the sustainable limit. In arid areas, there is no effect by climate change, but land subsidence by groundwater depletion is often permanent and it is difficult to recover the natural condition.

In coastal wetlands, river or tide gauge stations are constructed to monitor temporal variation of hydrological flow. However, most gauges are measuring water level in open water, not within inland wetland. Furthermore, the gauges do not provide sufficient information about water flow inside the wetlands and comprehensive assessment of flood hazards. Even the installed gauges are very sparse and not cost-effective. Although a variety of remote sensing technologies have been utilized for wetland application, data from optical satellites and SAR backscatter were only used for discriminating land cover and detecting the change of the extent in marshes and swamp forests. Due to insufficient gages in the wetlands, the relationship between parameters including water level change, biomass, and density and SAR backscatter has not been unveiled. Also, InSAR technology has limitation in monitoring the actual movement of water level in the wetlands, while estimating only relative water level changes in swamp forests. Generally, due to the limitation of each sensor, utilizing only a single technology cannot reach a high resolution and accuracy analysis. Therefore, the fusion of multiple radar sensor data from SAR/InSAR and radar altimetry is required for in-depth wetland studies.

In arid areas of the USA, the extensometers and GPS stations are constructed to monitor the land subsidence and the change of aquifer-system in the underground. The stations are also sparse and not cost-effective, and GPS survey campaigns are labor-intensive. The InSAR technology, which measures the variation of range in line-of-sight (LOS) direction, has a great advantage in measuring vertical displacement, and the estimated deformation has been used for modeling of seismic and volcanic activities. However, the conventional InSAR is not optimal for time-series analysis, because it is related to monitoring ground movement between two particular dates. For time-series analysis, both PSInSAR and SBAS InSAR technologies can be used through analyzing phase values from multiple InSAR pairs. Although PSInSAR relies on the use of point reflector, the sparse density of which restricts the accuracy of an analysis, SBAS InSAR better analyzes the distributed targets and maps the pattern of deformation in a large region. Therefore, when one has interest in evaluating highly detailed ground subsidence in the arid region, time-series analysis from SBAS InSAR belongs to one of the best possible technologies.

The SAR and InSAR technology can meet the requirements to monitor the surface change in a cost-efficient way with high accuracy and resolution. In Chapter 2, the water level change in the inland wetland was measured by integrating radar altimetry and InSAR technology. The inconsistency of phase unwrapping in the wetland is problematic, and the problem can be solved by using radar altimetry as an absolute reference datum. The fusion of two radar technologies enables one to map the absolute water level change in Louisiana wetland. In Chapter 3, the water level in the Everglades is estimated by using backscatter coefficients from ALOS PALSAR. In the grass-dominated areas, water level and backscatter coefficient are inversely proportional due to the effect of double-bounce scattering. When temporal or spatial decorrelation prevents obtaining a proper interferometric phase over vegetation, using the backscatter coefficient can aid to estimate hydrological change in the inland wetland like the Everglades. In Chapter 4, the SBAS InSAR technology was used to measure ground subsidence caused by groundwater depletion in the Tucson, Arizona. The SBAS InSAR enables one to obtain highly detailed spatio-temporal ground subsidence, and the spatial extent and magnitude of the deformation can be estimated.

CHAPTER 2: Integrated Analysis of PALSAR/Radarsat-1 InSAR and ENVISAT Altimeter for Mapping of Absolute Water Level Changes in Louisiana Wetland

2.1 Introduction

Modern landscapes are highly fragmented based on ownership priorities and land-use preferences. The Lower Mississippi River valley is an important economic corridor of agricultural, fisheries, forestry, and oil and gas enterprises that have contributed to a highly dissected landscape of natural and built levees and dredged canals aiding access, transport, and flood control. Efforts to reconnect dissected parcels into larger conservation planning units for the benefit of wildlife and floodway management require more comprehensive knowledge of how water resources are stored and exchanged between these segregated land units. In most cases, knowledge of water levels and flow patterns is lacking due to insufficient monitoring or gauge equipment on private and public lands within floodplain settings. Existing gauge networks maintained by State and Federal agencies are almost exclusively placed in navigable rivers and rarely in backswamp areas behind flood control levees. Only in recent decades have wetland scientists realized the lack of hydrological coupling in adjoining land units within and between floodways and the need for explicit monitoring of backswamp water levels. Unfortunately, the resources are lacking to deploy and maintain extensive gauge networks that would improve the understanding of the hydrological coupling within highly dissected floodplain settings.

The Lower Atchafalaya River basin is a major distributary diverting nearly 30% of the Mississippi River flow through forested and marsh wetlands at the coastal margin of the Gulf of Mexico. During high floods these wetlands receive nutrient-enriched river water that is believed beneficial for plant growth and for reducing the nutrient load that contributes to offshore hypoxia. Because these wetlands are also near sea-level in upper estuary settings, they are also prone to meteorological tides and surge events from landfalling tropical storms. Remote satellite telemetry observations are being used to interpret water level conditions in oceanic and inland settings. Forest cover and habitat type complicates the ability to use any one remotely sensed platform or instrument for accurate water level reconstructions. New methodologies and protocols are needed to use combined remotely sensed observations to improve the ability to monitor continuous water level or distinguish habitat type or other characteristics of wetland environments.

Interferometric Synthetic Aperture Radar (InSAR) has been proven to be useful to measure centimeter-scale water level changes over the floodplain. The L-band SAR satellites such as Shuttle Imaging Radar-C (SIR-C) and Japanese Earth Resources Satellite 1 (JERS-1) were utilized for detecting water changes within the Amazon floodplain (Alsdorf et al., 2000, 2001), and Everglades wetlands in Florida (Wdowinski et al., 2004). Furthermore, the C-band SAR images from European Remote Sensing satellite (ERS-1/2) and Radarsat-1 were used for revealing water changes beneath

Louisiana swamp forests, and it has been shown that polarization was an important factor in wetland application as Radarsat-1 images with HH polarization were more coherent than ERS-1/2 images with VV polarization over the swamp forests (Lu et al., 2005; Lu and Kwoun, 2008). This is based on the fact that the water beneath the swamp forest can provide double-bounce backscattering, which allows InSAR coherence to be maintained. Over the past few years, satellite radar altimetry has also been successfully used for water level monitoring over large inland water bodies such as the Great Lakes (Morris and Gill, 1994; Birkett, 1995) and the Amazon Basin (Birkett, 1998; Birkett et al., 2002), which have higher chances to be processed as ocean-like radar return. However, significant amount of data loss can occur during the periods of stage minima (lowest water level) due to the interruptions to the water surface by the surrounding topography. Furthermore, the radar return from a relatively small water body can be distorted. These limitations can be overcome by retracking individual return waveform (Berry et al., 2005; Frappart et al., 2006). Specifically, wetland water level variation beneath various types of vegetation (e.g., swamp forest, saline marsh, brackish marsh) in coastal Louisiana can be observed using retracked TOPEX/POSEIDON radar altimetry with an aid of 10-Hz *stackfile* data processing procedure (Lee et al., 2009).

In this study (Kim et al., 2009), we utilized Phased Array type L-band Synthetic Aperture Radar (PALSAR) and C-band Radarsat-1 SAR images, and ENVIronmental SATellite (ENVISAT) radar altimetry data together for the water level monitoring beneath the swamp forest in the Atchafalaya Basin (see Figure 2.1). Differential InSAR (D-InSAR) method can provide relative water level changes with high spatial resolution (~40 m), but a vertical reference is necessary to convert these to absolute water level changes. Most *in situ* water level gauges are located not in the swamp forests, but in the river channel; thus they cannot be used to resolve the absolute water level changes beneath the swamp forest. However, it has been shown that radar altimetry can provide absolute water level changes along its high-rate (10-Hz for TOPEX, 18-Hz for ENVISAT, corresponds to along-track sampling of 750 m and 417 m, respectively) nominal ground track (Lee et al., 2009). Hence, it can be used as the geocentric reference to enable estimation of the absolute water level changes. Finally, we then verified this technique using *in situ* water level gauges located within the swamp forest.

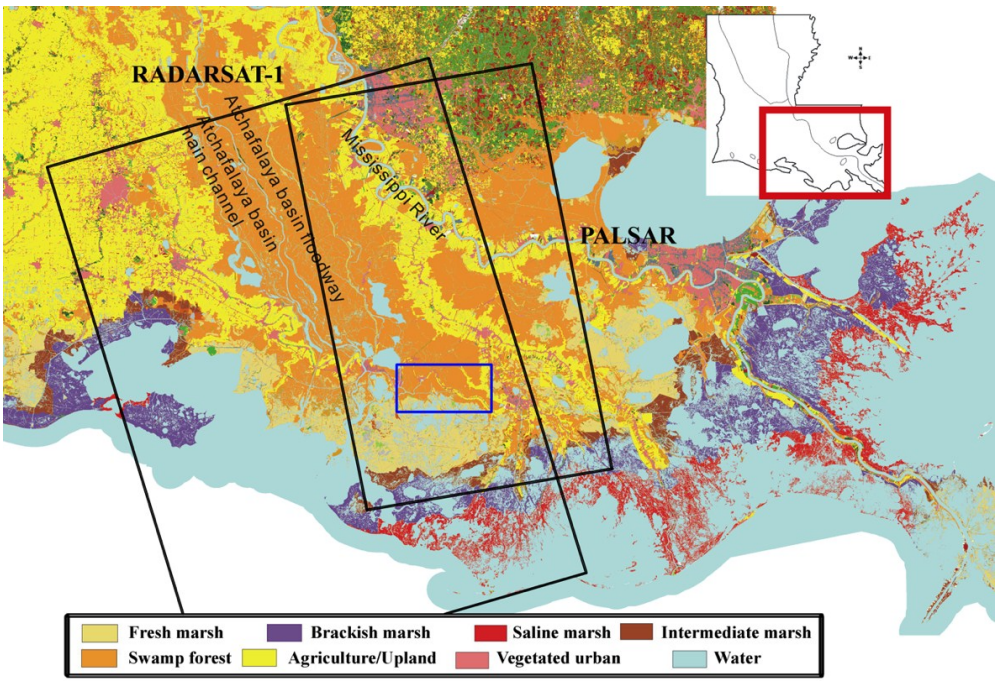

Figure 2.1. Thematic map, modified from Gap Analysis Program (GAP) and 1990 U.S. Geological Survey National Wetlands Research Center (USGS-NWRC) classification results, showing major land cover classes of the study area. Polygons represent extents of InSAR images shown in Table 2.1 for the PALSAR and Radarsat-1 tracks, respectively.

2.2 Data

For InSAR processing, eight scenes of PALSAR L-band and four scenes of Radarsat-1 C-band are used, as given in Table 2.1. Six scenes among the PALSAR scenes and all Radarsat-1 scenes are horizontal-transmit and horizontal-receive (HH) polarized, and the other two PALSAR scenes are horizontal-transmit and vertical-receive (HV) polarized. As illustrated in Figure 2.1, the SAR images cover southeastern Louisiana, which consists of swamp forests, marsh, upland forests, and agricultural field. The incidence angles of PALSAR and Radarsat-1 scenes are approximately 38.7º from descending track and 27.6 º from ascending track, respectively. PALSAR and Radarsat-1 have different wavelengths (PALSAR: 23.62 cm, Radarsat-1: 5.66 cm). As shown in Table 2.1, we used Radarsat-1 InSAR pair with perpendicular baselines shorter than 400 m because longer perpendicular baseline can result in loss of coherence. However, the coherence was still maintained using PALSAR InSAR pairs with relatively longer baselines. Pairs 3 and 4 in Table 2.1 were used to compare the coherences obtained from HH and HV polarizations.

Pair	Master date	Slave date	Sensor	Polarization	Δt (days)	$B_\perp$ (m)
1	2007.06.28	2008.02.13	PALSAR L-band	HH	230	1538.75
2	2008.02.13	2008.03.30	PALSAR L-band	HH	46	25.75
3	2008.05.15	2008.06.30	PALSAR L-band	HH	46	-2446.24
4	2008.05.15	2008.06.30	PALSAR L-band	HV	46	-2446.24
5	2006.12.31	2007.02.17	Radarsat-1 C-band	HH	48	-203.48
6	2007.12.26	2008.01.19	Radarsat-1 C-band	HH	24	254.18

Table 2.1. Characteristics of PALSAR/ Radarsat-1 InSAR pairs (Δt : temporal baseline, $B_\perp$: perpendicular baseline).

The ENVISAT altimeter data used in this study are from the periods of September 2002 to July 2008. The ENVISAT orbits on a 35-day repeat cycle with 98.5° inclination. The ENVISAT Geophysical Data Record (GDR) contains 18-Hz retracked measurements, corresponding to a ground spacing of approximately 350 m. The instrument corrections, media corrections (dry troposphere correction, wet troposphere correction calculated by the French Meteorological Office (FMO) from the European Centre for Medium-Range Weather Forecasts (ECMWF) model, and the ionosphere correction based on Global Ionosphere Maps (GIM)), and geophysical corrections (solid Earth tide and pole tide) have been applied. The ionosphere corrections usually obtained by combining the dual-frequency altimeter measurement over ocean could not be used in this study because of land contaminations. Thus, the GIM ionosphere corrections, based on Total Electron Content (TEC) grids, in the GDR were used for this study. Additionally, the 5.6 m level Ultra Stable Oscillator (USO) anomalies for ENVISAT cycles 44-70 were corrected using the European Space Agency's (ESA) algorithm in the form of a table (Benveniste, 2002).

2.3 Methodology

Two-pass D-InSAR method utilizes two SAR images acquired at different times over the same area. The interferometric phase difference (ϕ) between two SAR images, called interferogram, includes the signatures by topography (ϕ_{topo}), displacement (ϕ_{disp}), atmosphere effect (ϕ_{atmo}), baseline error ($\phi_{baseline}$) and noise (ϕ_{noise}) such as:

$$\phi = \phi_{topo} + \phi_{disp} + \phi_{atmo} + \phi_{baseline} + \phi_{noise} \tag{2.1}$$

By removing other components, the phase difference by displacement, can be acquired. Topographic phase can be simulated from a Digital Elevation Model (DEM). The atmospheric effects can introduce spatially-correlated artifacts of a few centimeters, and the baseline error can be modeled and removed. The noise level of the interferometric phase depends on the coherence of the image pairs. In general, the volume and surface scattering over forested areas yield low coherence or decorrelation (loss of coherence). However, if the emitted radar signal is reflected twice from the water surface and vegetation, and returned back to the antenna, which is called "double-bounce" backscattering, it is possible to obtain a good coherence from inundated vegetation. As a result, the water level change ∂h can be obtained from the displacement phase as follows:

$$\partial h = -\frac{\lambda \phi_{disp}}{4\pi \cos\theta_{inc}} + n \tag{2.2}$$

where λ is the SAR wavelength, θ_{inc} is the SAR incidence angle, and n is the noise caused by the decorrelation effects (Lu and Kwoun, 2008).

It is important to note that the InSAR technique cannot detect spatially homogeneous water-level changes (Lu and Kwoun, 2008; Lu et al., 2009). For instance, the water levels at two locations, x_0 and x_1 can increase homogeneously as much as $\partial h \left(= h_1 - h_0\right)$ during a time interval, ∂t (see Figure 2.2(a)). In this case, the InSAR method cannot measure any water level changes unambiguously because it can only measure the phase difference between a pixel and the neighboring pixels from which only the relative surface displacement (Lu, 2007), which is zero in this case, can be estimated. On the other hand, when the water levels at two locations vary heterogeneously in space during the time interval ∂t (see Figure 2.2(b)), the relative water level change between two locations, or the gradient of the water level change $\left(\frac{\partial h / \partial t}{\partial x}\right)$ can be measured from the interferogram. However, the absolute water level changes, dh_0 / dt at x_0 and dh_1 / dt at x_1, cannot be derived from the InSAR measurement alone. As a result, the water level measurement at a location within the interferogram is necessary to convert the relative water level change into the absolute water level change. The conversion can be achieved from Equation 2.3 such as:

$$\begin{bmatrix} \frac{dh_1}{dt} = \frac{dh_0}{dt} + \frac{\partial h_1 / \partial t}{\partial x}\Delta x + \frac{\partial h_1 / \partial t}{\partial y}\Delta y + \varepsilon \\ \vdots \\ \frac{dh_n}{dt} = \frac{dh_0}{dt} + \frac{\partial h_n / \partial t}{\partial x}\Delta x + \frac{\partial h_n / \partial t}{\partial y}\Delta y + \varepsilon \end{bmatrix} \tag{2.3}$$

where dh_n / dt is the absolute water level change at the nth location, dh_0 / dt is the absolute water level change at location x_0 obtained from a gauge station or altimeter measurement to be used as the vertical reference, $\frac{\partial h_n / \partial t}{\partial x}$ and $\frac{\partial h_n / \partial t}{\partial y}$ are the gradients of the water level change (relative water level changes) in x and y directions obtained from the InSAR measurement, and ε is an additional error term due to inappropriate observation of radar altimetry or the gradient error of InSAR. Although the water level gauge can be an ideal source providing the absolute water level change to be used as the vertical reference, most gauges are located in the river channel, not in the swamp forest. Due to the fact that the water level change in the swamp forest can be different from that in the river channel (Lu et al., 2005; Lu and Kwoun, 2008), the water level gauges in the river channel are not appropriate to be used as the vertical reference in this study.

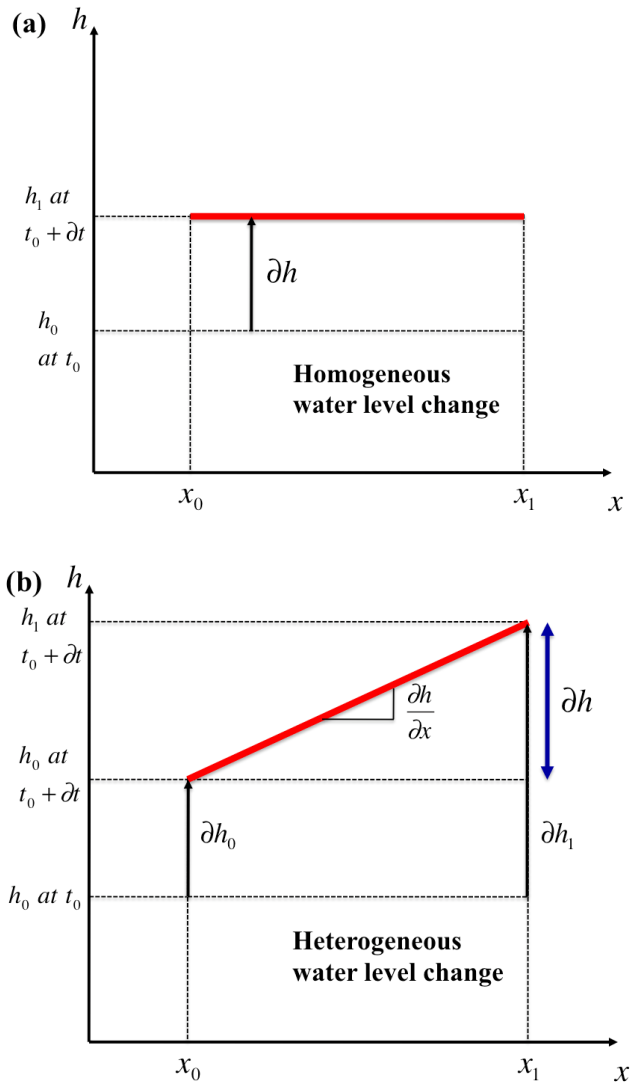

Figure 2.2. (a) Homogeneous water level change. x and h axes represent a spatial domain and the water level, respectively. During ∂t time interval at two points, x_0 and x_1 in the spatial domain, the water level increases constantly as much as $\partial h(=h_1-h_0)$. (b) Heterogeneous water level change within swamp forests. During ∂t time interval, the water level at point x_0 increases by dh_0, and the water level at point x_1 increases by dh_1. The difference dh_1-dh_0 is dented as ∂h.

Instead, the geocentric water level change measured from satellite radar altimetry can be used as the vertical reference. Along each 18-Hz ENVISAT nominal ground track (or *bin*), the absolute water level change time series can be generated from the ICE-1 retracked (Bamber, 1994) ENVISAT measurements with the regional *stackfile* method

(for details, see Lee et al., 2008, 2009). Hence, the radar altimeter, which passes over the swamp forest, can provide several observations of absolute water level changes denoted as $\left(\frac{dh_0}{dt}\right)_1,\cdots,\left(\frac{dh_0}{dt}\right)_n$ in Figure 2.3. When the wetlands are divided by levees or rivers, which can be commonly found in Louisiana, the water level changes among the divided wetlands (or water bodies) can be different. Therefore, a single vertical reference is needed to estimate the absolute water level change for each wetland body. The method of integrating InSAR and altimetery is to obtain the absolute water level change measurements from ENVISAT altimeter and use these to construct the absolute water level changes from InSAR.

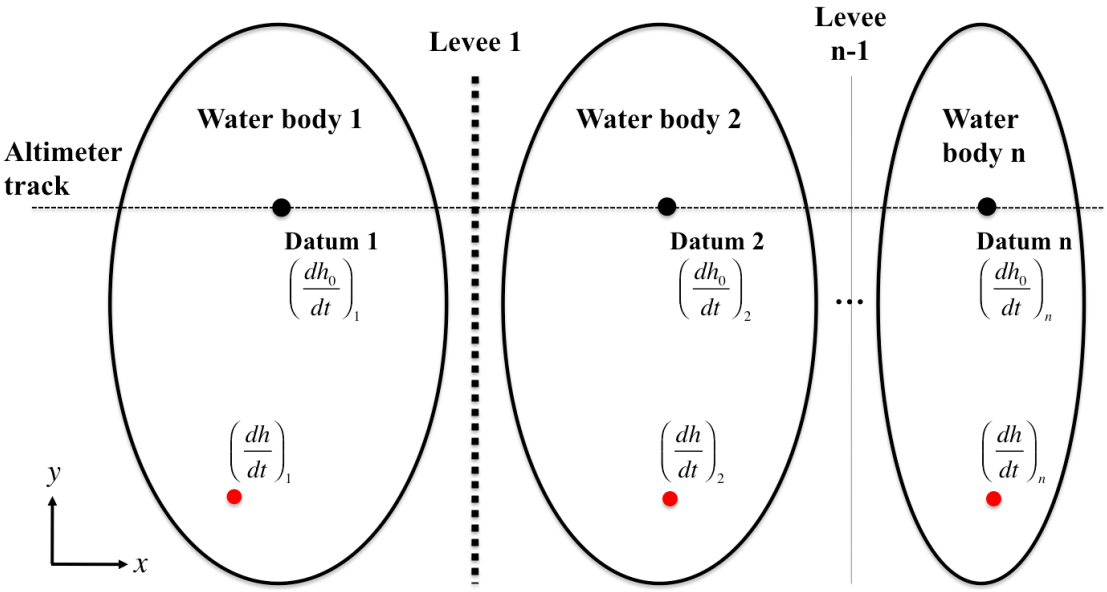

Figure 2.3. Schematic view of the Louisiana wetlands separated by several levees. $\left(\frac{\partial h/\partial t}{\partial x}\right)_1,\cdots,\left(\frac{\partial h/\partial t}{\partial x}\right)_n$ denote the gradients of the water level change over each water body. The vertical references, $\left(\frac{dh_0}{dt}\right)_1,\cdots,\left(\frac{dh_0}{dt}\right)_n$, over each water body can be obtained from satellite altimetry.

2.4. Results

2.4.1 InSAR processing and coherence/polarimetric analysis

First of all, co-registration of two SAR images, acquired at different times (master and slave data), is performed based on the correlation between the intensities (Rosen et al., 2000; Sheiber and Moreira, 2000). After differencing the co-registered SAR images, the interferogram is generated. The topographic phase is simulated from 30-m resolution C-band Shuttle Radar Topography Mission (SRTM) DEM and removed from the interferogram. The noise is also minimized by applying box-car and band pass filtering. Both PALSAR and Radarsat-1 images are deteriorated by the baseline errors due to inaccurate SAR satellite orbit information (Hanssen, 2000). Using fringe patterns over agriculture fields and urban areas, we estimated the best-fitting polynomial coefficients, which were used to remove the artifacts due to the baseline error. Figure 2.4 illustrates the wrapped differential interferograms, which contain primarily the displacement phase, and the corresponding coherences are shown in Figure 2.5. The mean coherences shown in Figure 2.5 are calculated over the swamp forest classified as in Figure 2.1 while excluded agricultural field, water channel, or upland forest. As can be seen from Figure 2.5, PALSAR has generally higher coherence than Radarsat-1. It could be due to the difference in their wavelengths as SAR signals with L-band (PALSAR) can penetrate vegetation deeper than C-band (Radarsat-1) signal. In Figure 2.5(b), it can also be seen that the L-band coherence decreases as the absolute value of perpendicular baseline ($\left|B_{perp}\right|$) increases. Although we cannot make a conclusion based on two Radarsat-1 pairs, Lu and Kwoun (2008) observed no dependence of coherence on baselines less than 350 m. Another interesting point shown in Figure 2.5(b) is the coherence difference between InSAR pairs with different polarizations. As PALSAR provides fine beam dual-polarization (FBD) mode, which acquires SAR images from both HH and HV polarizations contrary to fine beam single-polarization (FBS) mode using only HH polarization, the InSAR pair generated from the SAR scenes acquired on May 15, 2008 and June 30, 2008 are obtained by using two different HH and HV polarizations. It can be seen from Figure 2.5 that the InSAR pairs using HH and HV polarization have about 0.4 and 0.1 coherence, respectively. As Lu and Kwoun (2008) concluded that VV polarized ERS-1/2 images have lower coherence than HH polarized Radarsat-1 images, the result confirms that HH polarization is optimal for wetland application of InSAR.

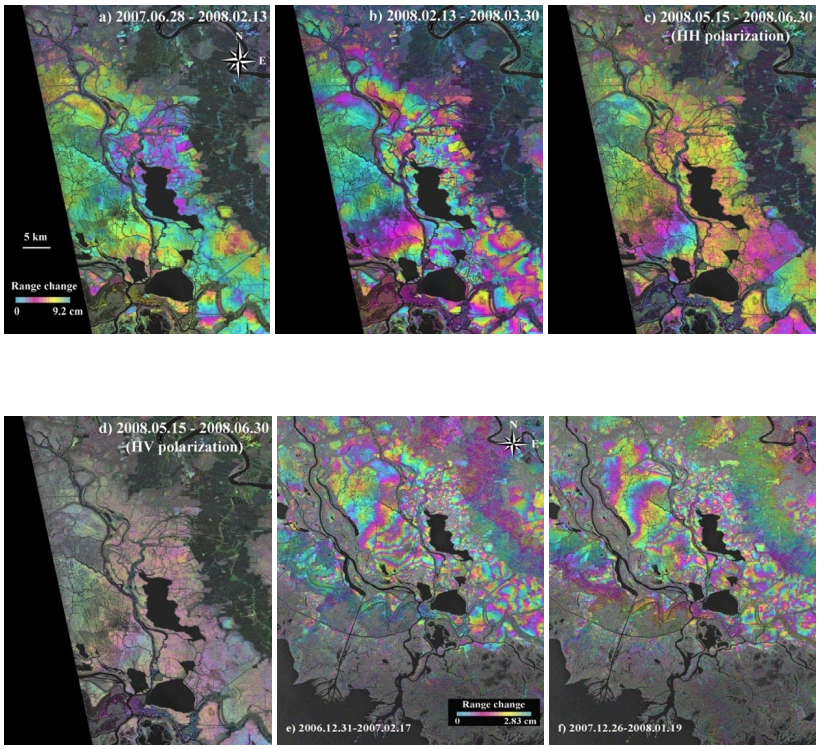

Figure 2.4. Wrapped interferograms after removing topographic phase, baseline errors and noise using PALSAR images (a) Jun 28 2007-Feb 13 2008 (b) Feb 13 2008-Mar 30 2008 (c) May 15 2008-Jun 30 2008 (HH polarization) (d) May 15 2008-Jun 30 2008 (HV polarization), and Radarsat-1 images (e) Dec 31 2006-Feb 17 2007 (f) Dec 26 2007-Jan 19 2008.

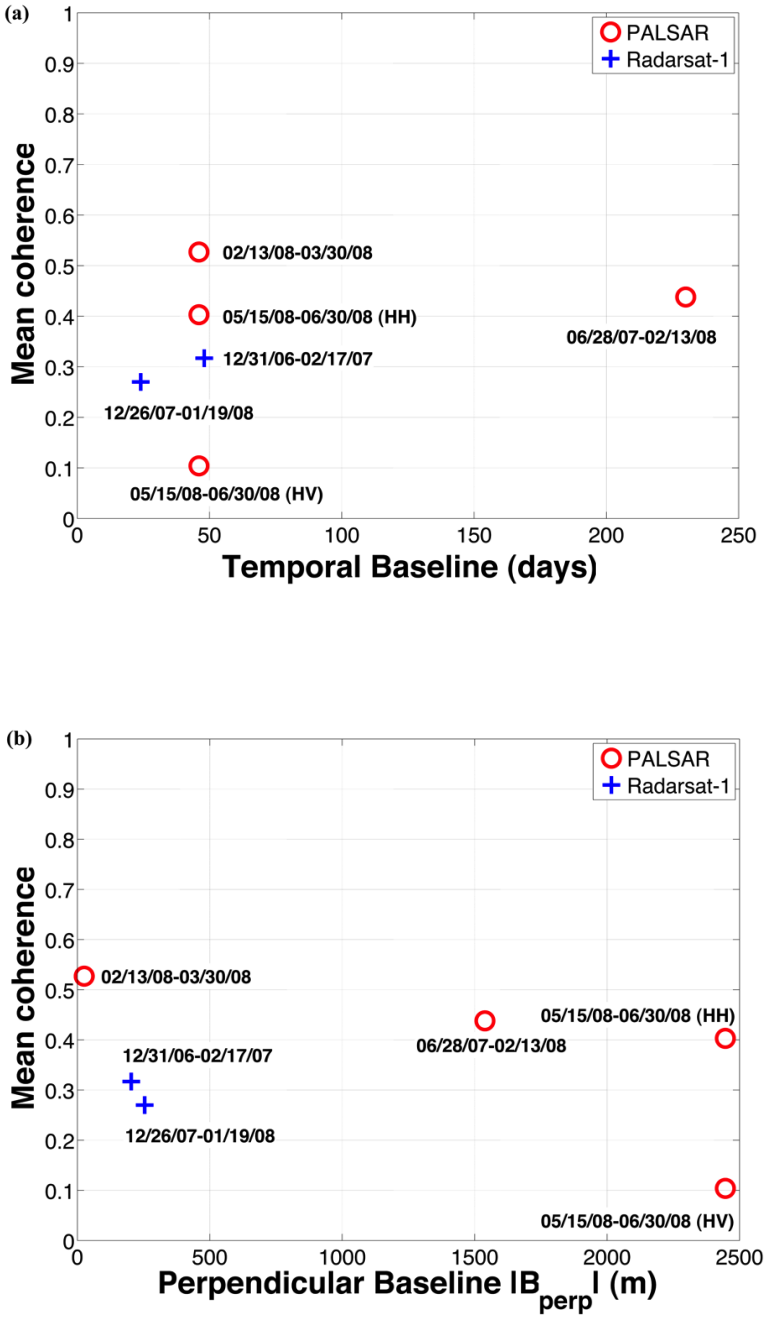

Figure 2.5. Mean coherences over the swamp forest of InSAR pairs with respect to (a) temporal baseline (days) (b) perpendicular baseline (m).

The co-polarized ratio, HH/HV ratio, can indicate the occurrence of double-bounce backscattering in the swamp forest. In general, the value of HH/HV increases constantly as double-bounce backscattering term increases (Freeman and Durden, 1998).

It is due to the fact that HH and HV polarizations are sensitive to double-bounce and volume backscattering, respectively. The area shown in Figure 2.6 is composed of swamp forest, fresh marsh, agricultural field, and upland forest. As shown in Figure 2.6, most of the swamp forest shows relatively high HH/HV ratio (0.4-1.0) indicated as red or yellow colors. This indicates that the primary scattering mechanism is the double-bounce backscattering. On the other hand, the upland forest is dominated by the volume scattering and thus it has small HH/HV. Buildings and cultivated areas in the agricultural field (i.e., harvested sugar cane field) show high ratio due to corner reflection and the similar scattering characteristics of HH and HV over the bare earth, respectively. Fresh marsh also shows double-bounce backscattering, but its strength is smaller than that of the swamp forest. This simple HH/HV ratio can help land surface classification in wetland because it enables us to identify the scattering characteristic.

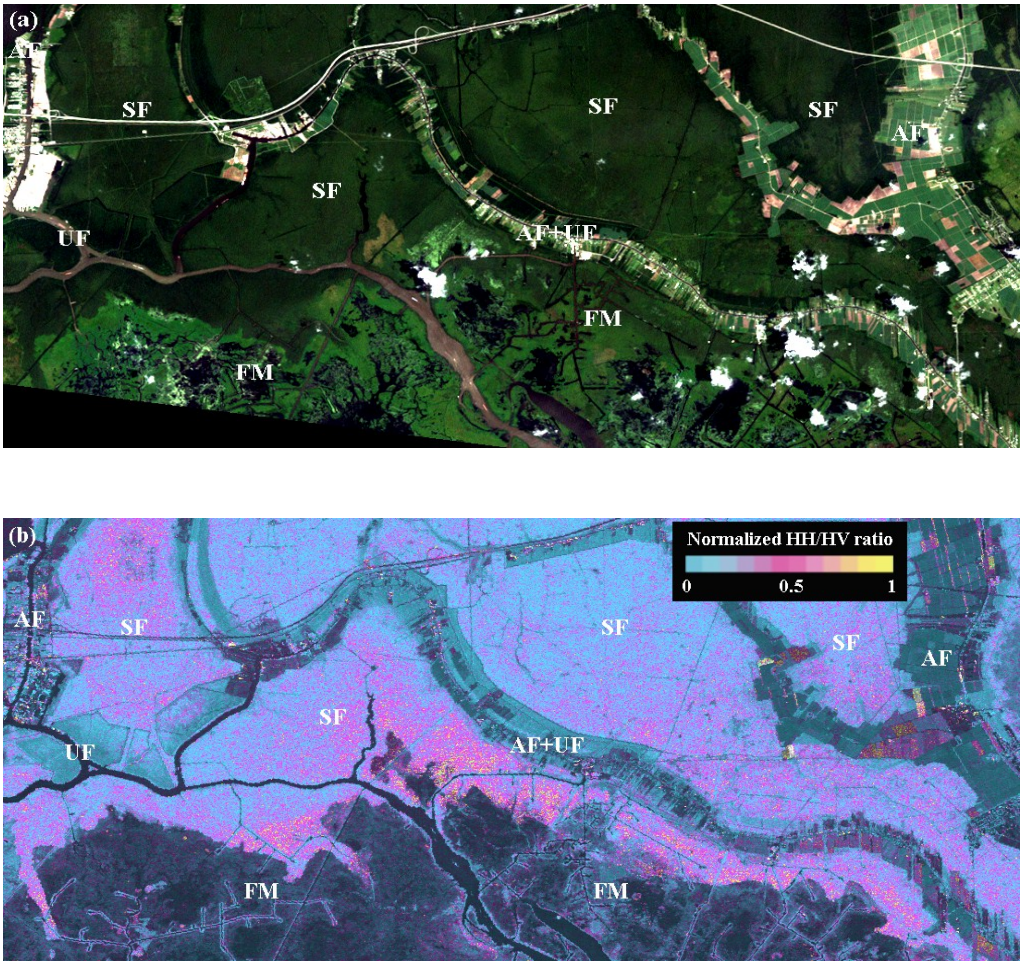

Figure 2.6. (a) Landsat ETM+ image (B: band 1, G: band 2, R: band 3, Aug 3 2001) over the area indicated by a blue box in Figure 2.1. (b) Normalized HH:HV ratio (PALSAR, Jun 30 2008); SF: Swamp forest, AF: Agricultural field, FM: Fresh marsh, UF: Upland forest.

Goldstein adaptive filtering (Goldstein and Werner, 1998) is further applied to reduce the noises in the interferogram, and the minimum cost flow (MCF) method (Costantini, 1998) is used for phase unwrapping. However, a priori information about the study area, the Atchafalaya Basin, is necessary for precise phase unwrapping with no phase jumps. Plenty of levees constructed to prevent flooding can be found in the basin, and this can result in different water level change patterns over the separated water bodies. A priori information is that area A shown in Figure 2.7 has smaller number of water channels which yield relatively wide and simple fringe patterns whereas area B has more water channels which yield relatively narrow and complex fringe patterns. Generally, complex and steeply wrapped fringe can cause the phase jump, which is a critical error in the procedure of phase unwrapping. To overcome the phase jump, the phase unwrapping of areas A and B is done separately. Specifically, the small water channels in area B, which can cause the phase jump, have been masked out. The final unwrapped interferograms in areas A and B are merged into one interferogram as shown in Figure 2.7.

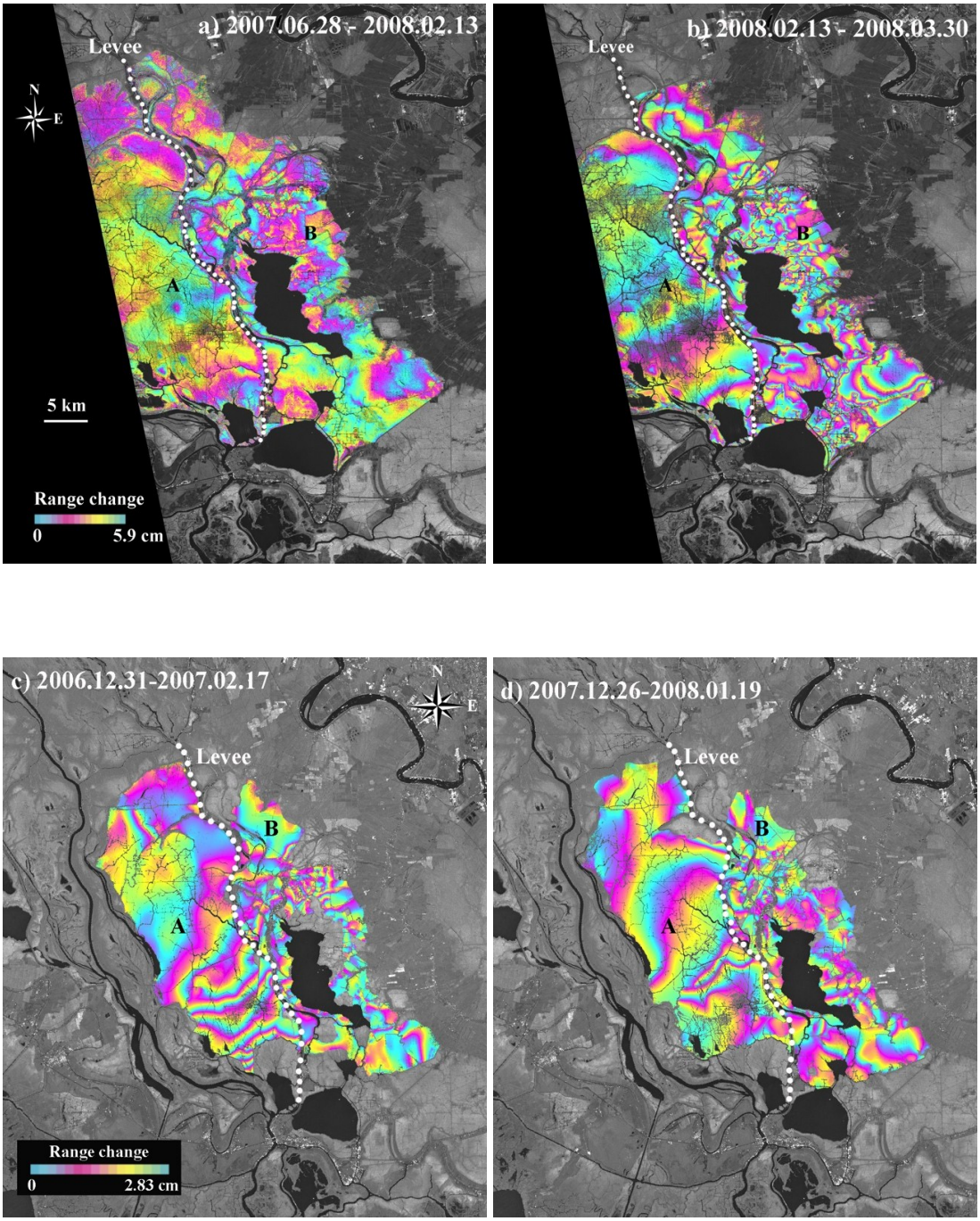

Figure 2.7. Unwrapped interferograms over the swamp forest from (a) (b) PALSAR, and (c) (d) Radarsat-1 InSAR. White dotted line indicates the levee separating the areas A and B.

2.4.2 Water level change from ENVISAT altimetry

Figure 2.8 illustrates the 18-Hz nominal ENVISAT ground track over the study area. Background is Landsat ETM+ band 4 (near-infrared) image, and it can help to classify different land cover types such as swamp forests, agricultural field, and open river channel along with the thematic map shown in Figure 2.1. Figure 2.9 shows the profiles of absolute water level changes from ENVISAT altimetry corresponding to a-d and e-j points in Figure 2.8.

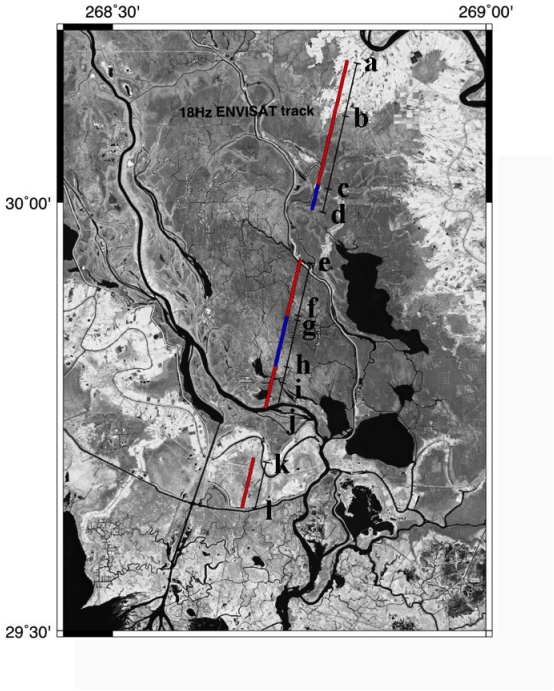

Figure 2.8. 18-Hz ENVISAT altimetry nominal ground track over the study area. Background is Landsat ETM+ band 4 image. Blue dots indicate the altimetry data points used for integration with InSAR.

Due to the different repeat periods of the satellites (ENVISAT: 35 day, PALSAR: 46 day, Radarsat-1: 24 day), ENVISAT measurements are interpolated to estimate the water level changes between the InSAR pair acquisition dates along each 18-Hz ENVISAT nominal ground track. It can be seen from Figure 2.9(a) that the surface elevation along section a-b shows large variation. This is due to the fact that the radar signal is backscattered from the agricultural field as can be seen from Figure 2.1 and 2.8, which may result in spurious height changes. Furthermore, the surface height changes along most parts of b-c can be influenced by the nearby agricultural field due to the large altimeter footprint (~2 km in diameter over flat surface). Hence, the water level changes over section c-d, which is apparently over the swamp forest, are chosen to be the vertical reference in area B. On the other hand, larger water level variation is observed along

sections e-f and i-j, which cover edges of the swamp forest (Figure 2.9(b)). It can be seen from Figure 2.8 that those profiles include not only the swamp forest but also the levee and open river channel. Therefore, the water level changes along the profile g-h are selected to be used as the vertical reference over area A.

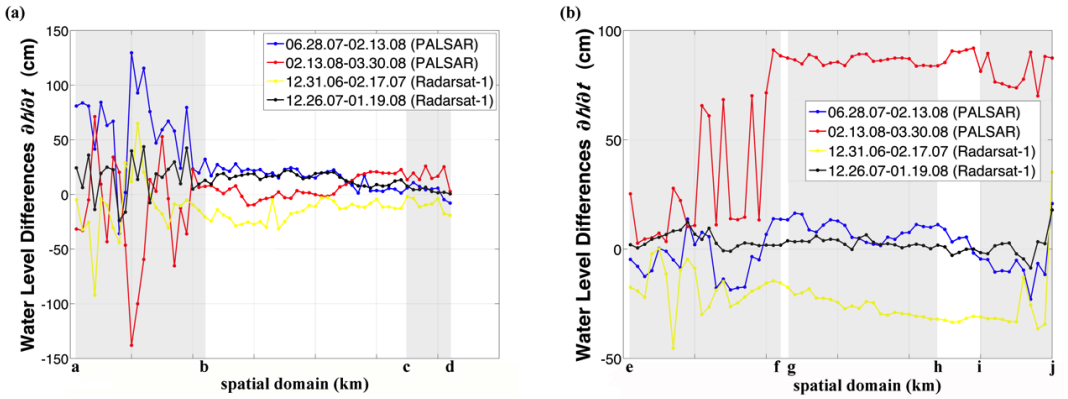

Figure 2.9. Absolute water level changes from ENVISAT altimetry. The water level changes are interpolated to be correspondent to InSAR acquisition dates. (a) Profile of water level changes along profile a-d shown in Figure 2.8 (b) Profile of water level changes along profile e-j shown in Figure 2.8.

2.4.3 Integration of InSAR and altimetry

Unwrapped interferograms in Figure 2.7 can only provide the gradient of water level changes between the InSAR acquisition times. Only the difference between the neighboring pixels can be used to estimate the surface displacement due to water level changes. Thus, the vertical reference is needed to convert the relative water level change to absolute water level change. Water level gauge data are the ideal data source to serve as the vertical reference; however, water level gauges are sparsely distributed and most of them are located in the river channel, and not in the wetlands. Blue dots in Figure 2.10 indicate the selected ENVISAT altimetry points, which are averaged to be used as the vertical references for area A and B $\left(\left(\frac{dh_0}{dt} \right)_A, \left(\frac{dh_0}{dt} \right)_B \right)$. These are used to generate the high-resolution (~40 m) absolute water level change maps shown in Figure 2.10. As can be seen from Figure 2.9, areas A and B have different patterns of absolute water level change. Specifically, from Figure 2.10(b), while area A has the water level change between 70 and 90 cm, the variation in area B ranges between 10 and 30 cm. The difference can be due to the existence of a levee between areas A and B, which blocks the water flow between them. Future work will incorporate the absolute water-level measurements from the altimeter as well as the water-level gradients from the altimeter to calibrate InSAR water-level measurements.

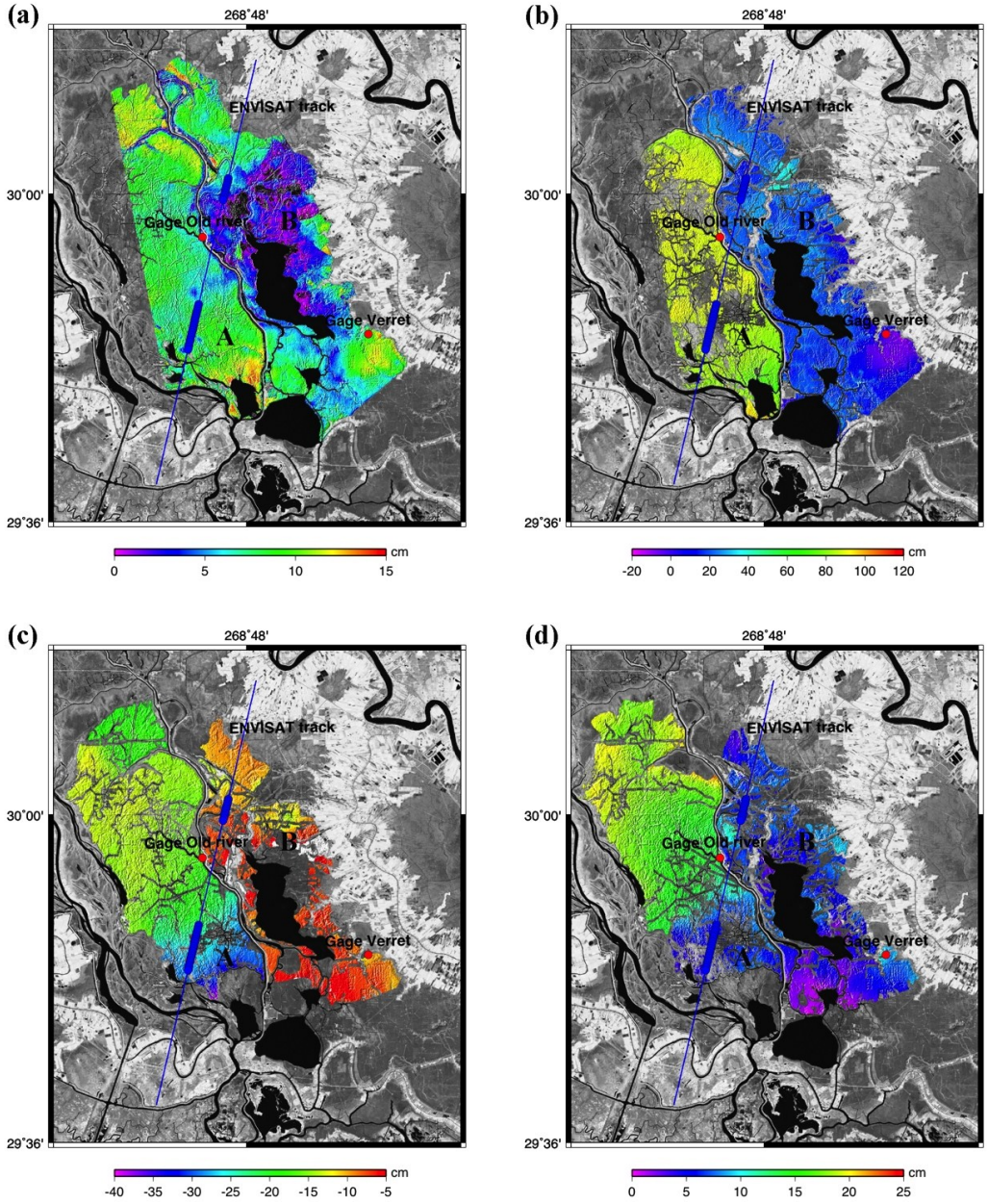

Figure 2.10. Maps of the absolute water level change over the swamp forest generated from the integration of ENVISAT altimetry with PALSAR L-band InSAR (a) Jun 28 2007 – Feb 13 2008 (b) Feb 13 2008 – Mar 30 2008, and Radarsat-1 C-band InSAR (c) Dec 31 2006 – Feb 17 2007 (d) Dec 26 2007 – Jan 19 2008. Blue line is the altimetry track and the blue dots indicate the data points used as the vertical reference. Red dots show the locations of water level gauges. Old river gauge is located in the river channel and Verret gauge is located within the swamp forest.

The absolute water level changes estimated from the integration of InSAR and altimetry can be validated by the water level gauges. Red dots in Figure 2.10 indicate the locations of the water level gauges. Old river gauge is located at the Atchafalaya River channel, and Verret gauge is located within the swamp forest in area B. Therefore, the Verret gauge can be used for the direct comparison in area B. Although the Old river gauge is located along the river channel, the comparison in area A is also attempted. The absolute water level changes at or near the gauges can be estimated from interferograms and Equation 2.3. The absolute water level changes, $\frac{dh_{Old\ river}}{dt}$ and $\frac{dh_{Verret}}{dt}$ at the Old River gauge and the Verret gauge can be estimated using $\left(\frac{dh_0}{dt}\right)_A$ and $\left(\frac{dh_0}{dt}\right)_B$, respectively. As the Old river gauge is not located within the swamp forest, the absolute water level change at the nearest pixel is used to be compared. The differences between the water level gauge measurements and the absolute water level changes from the integration method are shown in Table 2.2. It is remarkable to see that the differences at the Verret gauge are 2.23, 0.14, and 1.67 cm between the gauge data and the InSAR/altimetry integrated measurements. It is also interesting to see that the Radarsat-1 C-band InSAR provided a commensurate accuracy with the PALSAR L-band InSAR. Although the water level changes at the Old river gauge do not agree well as expected, they reveal the different water level changes in areas A and B. Specifically, during the time interval between Feb 13 2007 and March 30 2008, the water level at the Verret gauge shows decrease as much as 1.53 cm whereas it increases as much as 124.05 cm at the Old river gauge. This difference can demonstrate that a single vertical reference cannot be used in the wetlands which are divided by the levees or river channels.

Date	Sensor	$\frac{dh}{dt}$ at Verret (gauge)	$\frac{d\hat{h}}{dt}$ at Verret	Differ -ence	$\frac{dh}{dt}$ at Old river (gauge)	$\frac{d\hat{h}}{dt}$ at Old river	Differ -ence
2007.06.28 - 2008.02.13	PALSAR/ ENVISAT Altimetry	6.38	8.60	-2.23	3.96	2.69	1.27
2007.02.13 - 2008.03.30	PALSAR/ ENVISAT Altimetry	-1.53	-1.39	-0.14	124.05	83.84	40.21
2006.12.31 - 2007.02.17	Radarsat-1/ ENVISAT Altimetry	NA	-10.97		NA	-17.80	
2007.12.26 - 2008.01.19	Radarsat-1/ ENVISAT Altimetry	7.26	8.94	-1.67	1.22	13.36	-12.14

Table 2.2. Comparisons of the absolute water level changes from water level gauge data and InSAR/Altimeter method between InSAR acquisition times. $\frac{dh}{dt}$ is the absolute water level change from the water level gauge and $\frac{d\hat{h}}{dt}$ is the absolute water level change estimated from the integration of InSAR and altimetry.

2.5 Conclusion of the Integration between InSAR and radar altimetry

The wetland in coastal Louisiana has suffered from frequent flooding and severe storms, and has lost its area due to human activities and natural subsidence. Water level gauge networks located in open river channels cannot help monitor the water level change beneath the swamp forest due to the spatial variations in water level change. The integration of InSAR and altimetry has been demonstrated to be useful to generate the high-resolution absolute water level change maps over the swamp forest. The conclusion of this study can be summarized as follows:

1. The integration of InSAR and altimetry provides high-resolution absolute water level change maps. If more InSAR pairs are used, denser time series of water level maps can be generated.
2. 18-Hz retracked ENVISAT radar altimetry data can play a role as the vertical reference to convert the relative water level change to the absolute water level change. However, the radar return can be contaminated by the signals from open water or human structures due to its large footprint.
3. The absolute water level changes obtained from C-band InSAR shows commensurate accuracy with the water level change observed by L-band InSAR. C- and L-band SAR images have their own advantages and disadvantages. L-band data have deeper

penetration depth in the swamp forest and consequently maintain higher coherence, but they are more vulnerable to ionosphere refraction errors. C-band SAR images are less coherent, but also less influenced by the ionosphere effect. As both C- and L-band InSAR images can be utilized, we can estimate water level changes using either or both frequency SAR sensors together with radar altimetry.

4. This study shows that PALSAR HH polarization obtains higher coherence over the swamp forest than the PALSAR HV polarization mode. Generally, HH polarization is more sensitive to the double-bounce backscattering while HV polarization is more susceptible to the volume scattering inside the canopy. Therefore, HH polarization is preferred for wetland application of InSAR.

CHAPTER 3: Monitoring Everglades Freshwater Marsh Water Level Using L-band Synthetic Aperture Radar Backscatter

3.1 Introduction

Wetlands provide significant ecosystem services including flood control, water quality improvement, waterfowl and rare plant habitat provision, and unique recreational opportunities. However, almost half of the wetland area in the United States has been converted to other land uses, since major portions of the wetlands in the Louisiana, Mississippi, California, Florida, and Ohio have been utilized for agriculture, urban development and resource extraction (Mitsch and Gosselink, 2007; Fraser and Keddy, 2005). The Everglades of Florida are a unique ecosystem recognized by the United Nations Educational, Scientific and Cultural Organization (UNESCO) as a world heritage site. Everglades hydrology is the most important factor in establishing and maintaining the capacity of the wetlands to support the vegetation, animals and microbes that are closely linked to its hydroperiod and water level fluctuations. Alteration of Everglades hydrology by drainage canal and dike construction and the manipulation of flows for flood control, irrigation and other water uses has changed wetland conditions. Furthermore, the Everglades have been the subject of a major ecological restoration effort on the part of a coalition of government and non-government institutions. The fundamental goal of the project is to control the timing, quantity and quality of water flowing through the Everglades to replicate hydrologic conditions that existed prior to human intervention and development (USACE, 1999). For research and monitoring purposes, various Federal and State agencies have installed water stage gages throughout the Everglades. Data from all these sources are now collected operationally, distributed and converted to water depths through the Everglades Depth Estimation Network or "EDEN" (Tellis, 2006). While the gage network is unique given its density over such a large wetland area, gages may malfunction during extreme flood or drought conditions. Improved monitoring of Everglades water levels are needed for scientific and resource management purposes (Jones et. al., 2012). Information gathered through remote sensing can supplement processes to the understanding of development through field research to help restore and adaptively manage the Everglades (Jones, 2011).

Synthetic Aperture Radar (SAR) data comprises backscattering coefficient (called sigma naught; $\sigma 0$) as well as phase information. To-date, SAR backscatter coefficients from polarimetric or non-polarimetric spaceborne or airborne SAR platforms have mostly been employed for land cover classification. SAR interferometry (InSAR) using phase information has traditionally been used to detect horizontal and vertical displacements by catastrophic natural disasters of earthquakes and volcanoes throughout the world (Hanssen, 2001; Tong et al., 2010; Lu et al., 2007), and groundwater depletion around major metropolitan areas such as Phoenix and Las Vegas (Galloway and Hoffmann, 2007). However, innovative applications of InSAR to estimating hydrologic changes in

the wetlands have also been successful. Since Alsdorf et al. (2000 and 2001) mapped hydraulic flow in the Amazon basin using InSAR, Lu et al. (2005 and 2008) showed the feasibility of C-band interferometry over the wetland in the Louisiana, Wdowinski et al. (2004 and 2008) detected surface water level changes within water conservation area in the Everglades, and Kim et al. (2009) successfully combined radar altimetry and InSAR to estimate absolute water level changes in the swamp forests of the Atchafalaya basin. Interferometric coherence, a by-product of InSAR, may be the key component in distinguishing wetland types and other biogeological factors. Kim et al. (2013) analyzed the relation between interferometric coherence in the Everglades wetland, inherent SAR parameters of polarization, incidence angle, and wavelength, wetland types, and physical and temporal InSAR components. Furthermore, SAR backscattering coefficient is very useful for discriminating land cover types, and delineating inundated areas in the large river basins or wetland areas (Hess et al., 1990; Hess et al., 1995; Hess et al., 2003; Ramsey III, 1995; Wang et al., 1995; Kwoun and Lu, 2009). However, only a few studies have focused on the variation of radar backscatter associated with wetland water level changes (Smith, 1997). Hess et al. (1995) and Alsdorf et al. (2000, 2001) showed that variations in flood stages along the Brazilian Amazon influenced the radar backscatter signatures from the SIR-C instruments. Kasischke et al. (2003) studied the relationship of ERS C-band radar backscatter and several components including water level change, biomass, and soil moisture over the Big Cypress National Preserve in the Everglades. One obstacle to wider use of SAR/InSAR in wetland applications is the lack of water level gage data inside wetland for example, to provide vertical datum constraints. Most gages are located in open water and near-shore, where SAR produces little backscatter and it is therefore difficult to establish any concrete relationship between hydrologic change and backscatter. However, given the EDEN's relatively numerous and extensive water monitoring stations, the Everglades is an ideal place for the study to correlate wetland water level changes with SAR backscatter.

In this study, we analyzed relationships between SAR backscatter coefficient, InSAR differential interferograms, and in situ water level changes. Thirty-eight gages installed in the Everglades freshwater marshes provide daily water level data, which can be used to compare with possible water level changes inferred by the backscattering coefficients and interferograms derived from L-band PALSAR Fine-Beam mode (FB) and ScanSAR data, and C-band Radarsat-1 SAR data. Here we will compare the respective temporal and spatial variations on water level changes using the different types of SAR backscatters with different frequencies in the Everglades.

3.2 Characteristics of study region and data

3.2.1 Characteristics of study region

The Florida wetlands south of Lake Okeechobee (Figure 3.1(a)) are collectively referred to as the Everglades. Historically, this "river of grass" flowed from Lake Okeechobee south/southwestward to the Florida Bay (Douglas, 1947). Beginning in the

19th Century, canals, levees, and roads were constructed to drain sawgrass prairie for agricultural uses, control flooding from the Lake, supply water for irrigation, industry and residential use and afford population growth and commerce. Now these canals, levees, roads and other administrative boundaries divide the Everglades into water conservation areas (WCAs), the Big Cypress National Preserve, the Biscayne National Park, the Everglades National Park, and the Florida Panther National Wildlife Refuge (among others). The Everglades consists of herbaceous and woody wetlands also called freshwater marshes and swamps (Doren et al., 1999; Kim et al., 2013). As shown in Figure 3.2, the dominant plant species of WCAs and Everglades National Park is sawgrass and graminoid-prairie (cattail; *typha*). Hardwood forests, pineland savannas, and cypress forests comprise the woody wetlands. The freshwater marsh is dotted with tree islands composed of mixed shrubs in a slightly high elevation, and the mixed shrubs functioning as a shelter for wildlife are in less frequent flooding. The regions in the west of the WCAs are occupied by freshwater swamp, which is characterized by seasonally inundated Cypress forests reaching the height of tens of meters. The coastal regions around the Florida Bay and Gulf of Mexico are covered by Mangrove swamps. In this study, we concentrated on the WCAs, because they include a large number of water monitoring stations, the paths of various satellite SAR systems overlap there, and the region is one of planned road/levee alteration for ecosystem restoration (USACE, 1999). Individual WCAs are dissected by control structures resulting in such as WCA2, WCA2B, WCA3A, and WCA3B. Because WCA3A is separated by large canals, we divided the WCA3A into WCA3A-1~4 for better description. The density of installed gages varies by WCA section. WCA1, WCA3A-3, and WCA3B have densely spaced gages compared to other WCA subsections.

The yellow box in Figure 3.1(a) outlines our specific interest area, which is shown at larger scale as Figure 3.1(b). The dominant vegetation cover in the Water Conservation Areas (WCA1~3) and Stormwater Treatment Areas (STA2~6) is *Cladium Jamaiscense* or "sawgrass" (Zweig and Kitchens, 2008). Due to the water flow manipulation via the South Florida Water Management District (SFWMD) control system, each WCA and even subsections within them can show very different hydrologic patterns even given similar weather conditions. Some areas can undergo increases in water levels, whereas other sections are experiences water level decreases or no change. The 38 gages we analyzed are also highlighted in Figure 3.1(b). Although data from more gages are available, gages within canals are only representative of water levels within the relatively narrow control structures and were therefore excluded from the analysis.

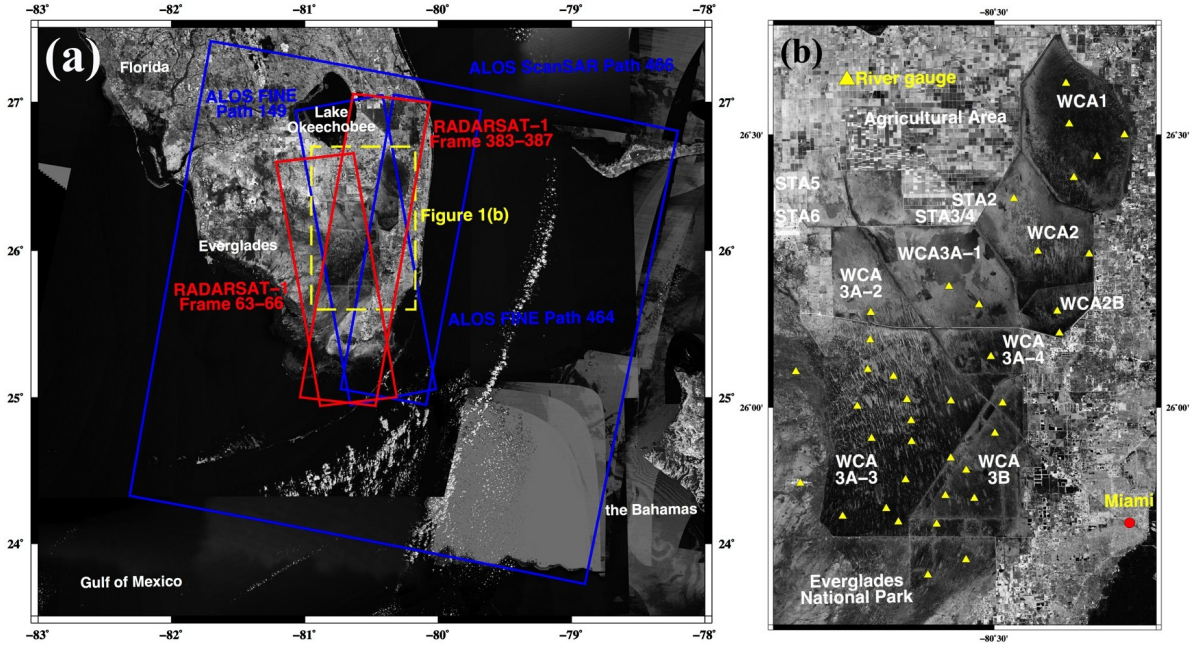

Figure 3.1 (a) Landsat image including the research region shows the coverage of ALOS Fine-beam and ScanSAR mode (blue boxes) and RADARSAT-1 imagery (red boxes) (b) Detailed images in yellow box of Figure 3.1(a) represent the location of thirty-eight gauges (yellow triangles) and each section of Water Conservation Areas (WCA1, WCA2, WCA2B, WCA3A-1~4, WCA3B) and Stormwater Treatment Area (STA2~6).

3.2.2 Data

ALOS PALSAR L-band and RADARSAT-1 C-band SAR data were used for this study. To provide a combination of more frequent coverage of a large area and some fine spatial detail, seven ALOS PALSAR ScanSAR and 18 FB scenes were analyzed. ScanSAR images provide large coverage (350km x 350km) that is important over vast wetland areas while the high resolution (30m) of FB data affords detailed information within the wetlands. Combining the two modes helps to overcome the relatively infrequent observations of ALOS (revisiting date: 46 day). Another intriguing advantage given the use of different beam modes is that ScanSAR and FB data are acquired using descending and ascending tracks, respectively. Because they observe the same area with different perspectives, the radar backscatter can be affected by different penetration and backscattering within a resolution cell. Different or even independent signatures from identical land surfaces may add diagnostic information. In addition to the ALOS PALSAR data, 33 FB Radarsat-1 images were also analyzed. Their spatial resolution is approximately 30 m following multi-look processing and geocoding. The coverage of ALOS PALSAR (blue box) and Radarsat-1 (red box) are also delineated in Figure 3.1(a). ALOS ScanSAR has the largest coverage among all used scenes. Only the third and fourth subswaths among the total five available from ScanSAR needed to be merged into a single SAR backscatter image, because both have enough coverage over the Everglades. The FB scenes of ALOS and Radarsat-1 either partially or completely cover our research region. Table 3.1 provides detailed information on all used SAR scenes. PALSAR scenes from path 149 (FB) were observed from ascending track, and those from path 464 (FB) and 466 (ScanSAR) were acquired from descending track. Radarsat-1 scenes were obtained from both descending and ascending tracks. This study utilized only HH-polarized ALOS PALSAR and Radarsat-1 SAR images. Previous studies (Kim et al., 2009; Kim et al., 2013) suggest that HH polarization is best for wetland SAR/InSAR application. The HH-polarized radar signal is strongly double-bounce scattered by tree-trunks in swamp forests and grass stems in freshwater marsh. Also, the HH-polarized signal is less attenuated by vertical stems or trunks in the wetlands due to larger Fresnel reflection of HH than that of VV. In addition, in terms of high coherence in InSAR and the sensitivity to the flooded and unflooded conditions in SAR radar backscatter, HH-polarization is preferred over other polarized SAR data for SAR/InSAR.

The land cover data (SFWMD, 2004) shown in Figure 3.2 were used to identify vegetation types and verify that all water level gauges were located within the wetland and not within a canal. The land cover data was created and revised by the SFWMD using visual interpretation of color infrared digital orthophotoquads produced from imagery acquired from November 2004 through March 2005. While the original data include urban, transportation, water, and other vegetation classes, all but wetland type were regrouped into a single "non-wetland" class. Water level gage data at locations (yellow triangles) in Figure 3.1(b) assembled and quality assured through the EDEN were acquired from U.S. Geological Survey (USGS) National Water Information system for Florida (http://waterdata.usgs.gov/fl/nwis). EDEN uses the North American Vertical Datum of 1988 (NAVD 88). Table 3.2 lists the inland wetland water gages used for this

study. Their general locations and their land cover classification as derived using the data shown in Figure 3.2. The gages are located in the mixed shrubs, graminoid prairie marsh, and sawgrass marsh of the WCAs. Note that the mixed shrubs-covered wetland is within the freshwater swamp, while most gages are in the freshwater marsh. Additional geospatial data such as the Shuttle Radar Topography Mission (SRTM) digital elevation model (DEM) and Landsat Thematic Mapper (TM) data were used for geocoding.

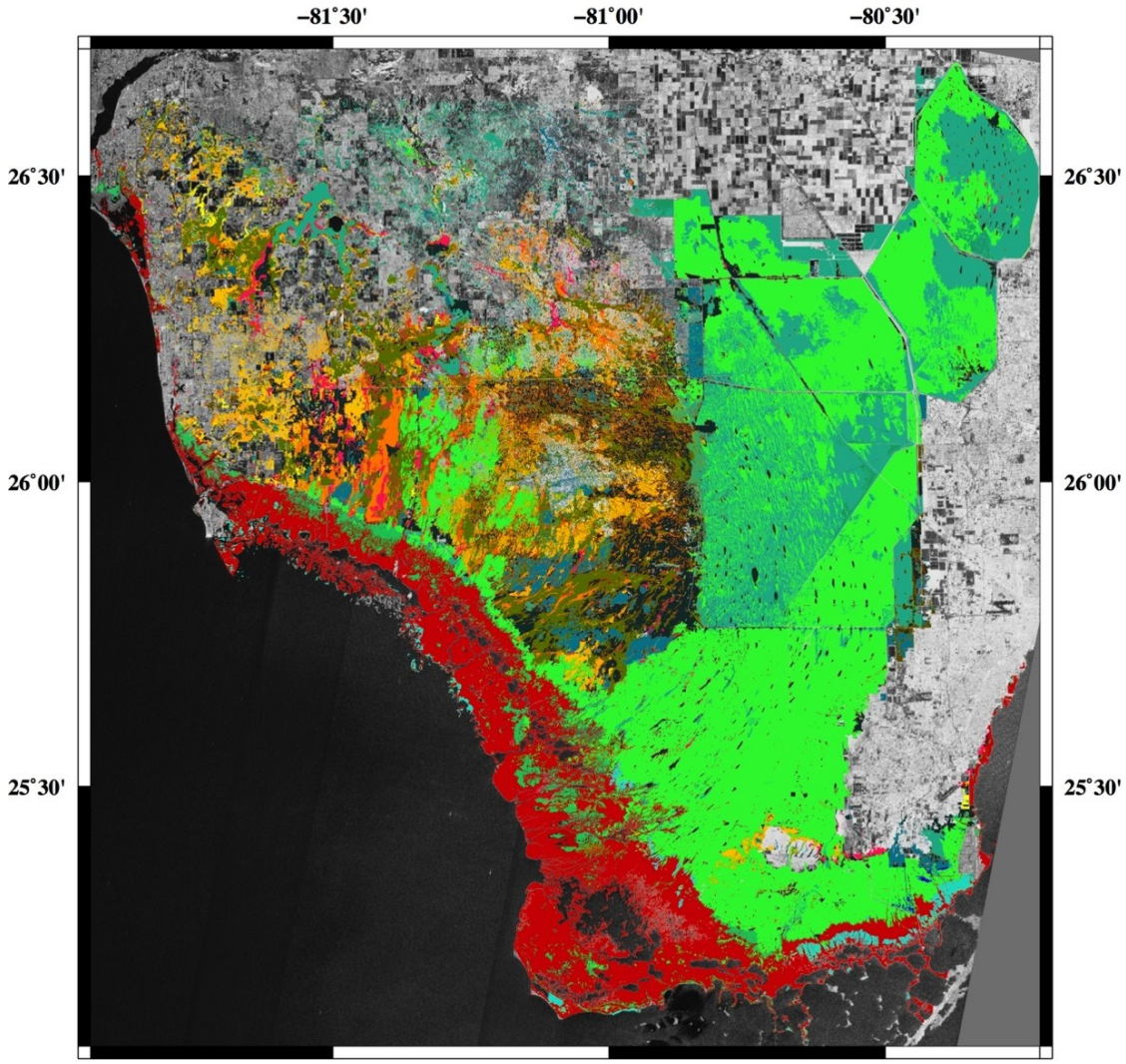

Figure 3.2. Land classification map in the wetlands of the Everglades, Florida. Each colored region represents vegetation types and the classification map includes inland and coastal marshes, and swamp forests. Background gray image is an intensity data from ALOS PALSAR ScanSAR mode.

Date	Sensor	Path	Beam	Band	Direction
2007.01.11	PALSAR	149	Fine	L-band	Ascending
2008.01.14	PALSAR	149	Fine	L-band	Ascending
2008.05.31	PALSAR	149	Fine	L-band	Ascending
2009.10.19	PALSAR	149	Fine	L-band	Ascending
2010.01.19	PALSAR	149	Fine	L-band	Ascending
2010.04.21	PALSAR	149	Fine	L-band	Ascending
2010.06.06	PALSAR	149	Fine	L-band	Ascending
2010.09.06	PALSAR	149	Fine	L-band	Ascending
2010.12.07	PALSAR	149	Fine	L-band	Ascending
2011.01.22	PALSAR	149	Fine	L-band	Ascending
2011.03.09	PALSAR	149	Fine	L-band	Ascending
2007.11.02	PALSAR	464	Fine	L-band	Descending
2009.11.04	PALSAR	464	Fine	L-band	Descending
2008.12.20	PALSAR	464	Fine	L-band	Descending
2009.03.22	PALSAR	464	Fine	L-band	Descending
2009.11.07	PALSAR	464	Fine	L-band	Descending
2010.02.07	PALSAR	464	Fine	L-band	Descending
2010.03.25	PALSAR	464	Fine	L-band	Descending
2010.01.26	PALSAR	466	ScanSAR	L-band	Descending
2010.03.13	PALSAR	466	ScanSAR	L-band	Descending
2010.04.28	PALSAR	466	ScanSAR	L-band	Descending
2010.07.29	PALSAR	466	ScanSAR	L-band	Descending
2010.09.13	PALSAR	466	ScanSAR	L-band	Descending
2010.12.14	PALSAR	466	ScanSAR	L-band	Descending
2011.01.29	PALSAR	466	ScanSAR	L-band	Descending
2007.01.24	Radarsat-1	383~387	Fine-5	C-band	Descending
2007.02.17	Radarsat-1	383~387	Fine-5	C-band	Descending
2007.03.13	Radarsat-1	383~387	Fine-5	C-band	Descending
2007.04.30	Radarsat-1	383~387	Fine-5	C-band	Descending
2007.05.24	Radarsat-1	383~387	Fine-5	C-band	Descending
2007.06.17	Radarsat-1	383~387	Fine-5	C-band	Descending
2007.07.11	Radarsat-1	383~387	Fine-5	C-band	Descending
2007.08.04	Radarsat-1	383~387	Fine-5	C-band	Descending
2007.08.28	Radarsat-1	383~387	Fine-5	C-band	Descending
2007.09.21	Radarsat-1	383~387	Fine-5	C-band	Descending

Continued

Table 3.1. List of used ALOS PALSAR and Radarsat-1 scenes.

Table 3.1. continued

Date	Sensor	Path	Beam	Band	Direction
2007.10.15	Radarsat-1	383~387	Fine-5	C-band	Descending
2007.11.08	Radarsat-1	383~387	Fine-5	C-band	Descending
2007.12.02	Radarsat-1	383~387	Fine-5	C-band	Descending
2007.12.26	Radarsat-1	383~387	Fine-5	C-band	Descending
2008.01.19	Radarsat-1	383~387	Fine-5	C-band	Descending
2007.02.12	Radarsat-1	383~387	Fine-5	C-band	Descending
2008.03.07	Radarsat-1	383~387	Fine-5	C-band	Descending
2008.03.31	Radarsat-1	383~387	Fine-5	C-band	Descending
2008.04.24	Radarsat-1	383~387	Fine-5	C-band	Descending
2007.01.18	Radarsat-1	63~66	Fine-5	C-band	Ascending
2007.03.07	Radarsat-1	63~66	Fine-5	C-band	Ascending
2007.03.31	Radarsat-1	63~66	Fine-5	C-band	Ascending
2007.05.18	Radarsat-1	63~66	Fine-5	C-band	Ascending
2007.06.11	Radarsat-1	63~66	Fine-5	C-band	Ascending
2007.07.05	Radarsat-1	63~66	Fine-5	C-band	Ascending
2007.08.22	Radarsat-1	63~66	Fine-5	C-band	Ascending
2007.09.15	Radarsat-1	63~66	Fine-5	C-band	Ascending
2007.10.09	Radarsat-1	63~66	Fine-5	C-band	Ascending
2007.11.26	Radarsat-1	63~66	Fine-5	C-band	Ascending
2008.02.06	Radarsat-1	63~66	Fine-5	C-band	Ascending
2008.03.01	Radarsat-1	63~66	Fine-5	C-band	Ascending
2008.03.25	Radarsat-1	63~66	Fine-5	C-band	Ascending
2008.04.18	Radarsat-1	63~66	Fine-5	C-band	Ascending

	Gauge name	Longitude	Latitude	Land cover
1	EDEN 1 Cypress	80°53'42.5" W	25°51'37.7" N	Mixed Shrubs
2	EDEN 6 Cypress	80°54'14" W	26°03'55" N	Mixed Shrubs
3	SITE 7 NO.1	80°20'50" W	26°31'10" N	Graminoid Prarie
4	SITE 8T NO.1	80°14'04.9" W	26°29'58.5" N	Graminoid Prarie
5	SITE 9 NO.1	80°17'25.9" W	26°27'35.3" N	Graminoid Prarie
6	North LOXAHATCHEE No.1	80°21'13.9" W	26°35'37.6" N	Graminoid Prarie
7	South LOXAHATCHEE No.1	80°20'16.3" W	26°25'17.0" N	Sawgrass
8	EDEN 11 2A	80°27'35" W	26°22'58" N	Sawgrass
9	SITE 17 2A	80°24'40" W	26°17'11" N	Graminoid Prarie
10	SITE 19 2A	80°18'23.9" W	26°16'53.3" N	Sawgrass
11	EDEN 13 2B	80°22'17" W	26°10'35" N	Sawgrass
12	SITE 99 2B	80°22'01.5" W	26°08'11.2" N	Graminoid Prarie
13	3A-5 3A	80°42'19" W	26°03'24" N	Graminoid Prarie
14	EDEN 4 3A	80°30'25" W	26°05'36" N	Graminoid Prarie
15	EDEN 5 3A	80°45'10" W	26°07'25" N	Graminoid Prarie
16	EDEN 8 3A	80°40'50" W	25°52'00" N	Graminoid Prarie
17	EDEN 9 3A	80°35'32" W	26°13'19" N	Sawgrass
18	EDEN 12 3A	80°35'17"W	26°00'42" N	Graminoid Prarie
19	EDEN 14 3A	80°45'27" W	26°04'10" N	Sawgrass
20	W-2 3A	80°48'32" W	25°47'59" N	Graminoid Prarie
21	W-5 3A	80°41'43" W	25°47'21" N	Graminoid Prarie
22	W-11 3A	80°45'00" W	25°56'34" N	Graminoid Prarie
23	W-14 3A	80°40'06" W	25°56'14" N	Graminoid Prarie
24	W-15 3A	80°40'40" W	26°00'51" N	Graminoid Prarie
25	W-18 3A	80°46'44" W	26°00'07" N	Sawgrass
26	SITE 62 3A	80°45'05.9" W	26°10'27.4" N	Graminoid Prarie
27	SITE 63 3A	80°31'51.9" W	26°11'18.1" N	Sawgrass
28	SITE 64 3A	80°40'10" W	25°58'31" N	Graminoid Prarie
29	SITE 65 3A	80°43'11.4" W	25°48'50.0" N	Graminoid Prarie
30	EDEN 7 3B	80°29'55" W	25°57'08" N	Sawgrass
31	EDEN 10 3B	80°37'02" W	25°47'07" N	Sawgrass
32	SITE 69 3B	80°35'19.6" W	25°54'24.0" N	Sawgrass
33	SITE 71 3B	80°33'25" W	25°53'04" N	Sawgrass
34	SITE 76 3B	80°28'57.9" W	26°00'28.0" N	Sawgrass
35	TI-8 3B	80°32'26.6" W	25°49'58.4" N	Sawgrass
36	TI-9 3B	80°35'57.6" W	25°50'15.7" N	Sawgrass
37	NE_SHARK_RVR_SLOUGH_NO2	80°33'26" W	25°43'11" N	Sawgrass
38	NE_SHARK_RVR_SLOUGH_NO1_NR	80°38'05.9" W	25°41'29.6" N	Sawgrass

Table 3.2. List of used gauge data within wetlands.

3.3 Data processing and methodology

Raw ALOS PALSAR and Radarsat-1 signal data was converted into geocoded intensity imagery through signal processing and geocoding. For ALOS ScanSAR scenes, the full aperture algorithm was used (Cumming and Wong, 2005). It fills gaps between bursts by zero padding, and implements conventional stripmap processors including focusing and range migration compensation. The intensity images from ALOS and Radarsat-1 FB were generated from the stripmap processor, which is also called the Range-Doppler Algorithm (RDA) (Curlander and McDonough, 1991). The geocoding of intensity was performed by estimating polynomial coefficients from high correlation points between SAR intensity images and geocoded products of SRTM 1-arcsec DEM and 30m resolution Landsat Mosaic image (USGS, 2012). In case of ALOS ScanSAR image, each subswath was geocoded, and then merged into a single image by considering the difference of backscattering coefficients between overlaps of geocoded subswath. Each intensity image was calibrated by temporal filtering to suppress speckle noise. Pixel values of ScanSAR 3rd subswath were compared to those of other subswath images within the area of overlap, because the 3rd subswath had a similar incidence angle with FB mode. Based on the overlapped areas between ScanSAR 3rd and 4th subswath, the calibration factor is applied to other ScanSAR scenes. Orthographic correction of the SAR imagery was deemed unnecessary, because overall topographic gradient within the study region is on the order of 1-3 meters (Jones, 2012). To minimize any remaining speckle noise, Lee filtering (Lee, 2009) was applied to the geocoded intensity images. Finally, filtered intensity images were easily converted into decibel (dB) value corresponding to the backscattering coefficient, which is also called sigma naught (σ^0).

Dimensionless, sigma naught is affected by physical properties of the radar collection process, such as incidence angle and polarization, and the characteristics of target surface within a resolution element. Radar satellites measure range in the near-nadir or off-nadir direction, with the near-nadir observation having almost zero incidence angle. Near-nadir observing radar satellite sensing, also known as radar altimetry, has been the best method to measure mean sea level and estimate geoid heights in oceanic regions. But radar altimeters are sampling, not imaging instruments. Therefore their products include point-wise information on range from radar to a target surface and backscatter coefficients. Radar altimetry can be applied to measuring water level changes in wetlands. In the Everglades, high backscatter of radar altimetry is returned from higher water level, when the altitude of satellite is stable. It depends on the characteristics of near-nadir observing radar altimetry, which receives most signals from wetlands at boresight (Figure 3.3(a)). In contrast to radar altimetry, off-nadir observing SAR satellites typically have 30~40 degree incidence angles, which enables us to capture various signatures given scattering processes, acquire larger cover areas by enlarged illumination, and generate high-resolution images by longer integration time and large Doppler bandwidth. However, as incidence angle increases, the radar backscatter from a ground element gradually decreases. Given high incidence angles and a water substrate, double-bounce scattering is one of the most prominent scattering mechanisms from vegetation-covered wetlands. The radar echo from tree trunks provokes backscatter, and the tree trunks function as a corner reflector similar to buildings in urban areas. The vegetation

height is a crucial factor that controls the effect of double-bounce scattering. For example, in a freshwater swamp dominated by Cypress that is tens of meters in height, double-bounce scattering becomes enhanced during high water season (Figure 3.3(b)). In contrast, the scattering mechanism is weakened over freshwater marsh covered by sawgrass that is only as tall as several meters during the same high water period (Figure 3.3(c)). In contrast, the inverse occurs when the height difference between vegetation canopy and water elevation is small. Many radar echoes are reflected away from the radar given surface scattering. Previous studies confirmed that C-band or L-band SAR returns exhibit an inverse relationship with coastal and inland marsh flooding (Ramsey III, 1995; Ramsey III et al., 2011). But more study is needed to verify the association between SAR radar backscatter and actual water level from gages. Polarization and wavelength is also an influential factor in double-bounce scattering, and HH-polarized L-band SAR platforms receive the radar echo from flooded wetlands as enhanced by double-bounce scattering. However, the SAR backscatter associated wetland targets is not simply defined by a single parameter. Rather, it is a result of a complicated mixture of soil moisture, biomass, canopy opening, vegetation density, tree height and water surface roughness induced by wind. This study hypothesizes that water level can be a defining factor of freshwater marsh scattering mechanisms because flooding condition in a short grass gradually converts double-bounce scattering into surface scattering. This study expects parameters of canopy opening and vegetation density that largely affect backscatter in a freshwater swamp are less influential in a freshwater marsh. Accordingly, exploring the relationship between SAR backscatter coefficient and hydrologic change at gages in the Everglades might help to unravel the elaborate processes of radar backscatter.

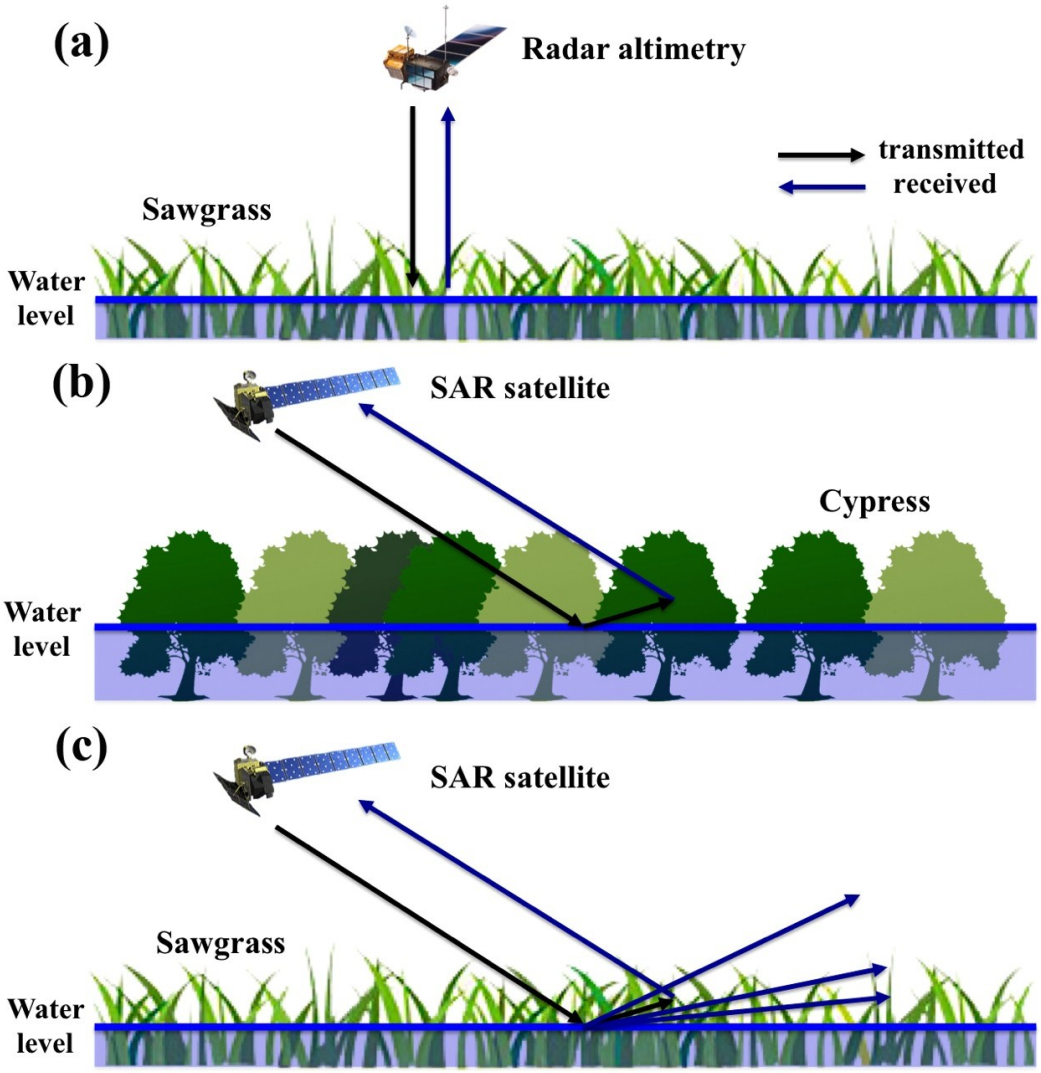

Figure 3.3 (a) Nadir observation of Radar altimetry over sawgrass-covered freshwater marsh (b) Double bounce scattering of SAR signal over swamp forests (c) Double bounce and surface scattering of SAR return over freshwater marsh (not to scale).

3.4. Results and discussion

3.4.1. Relationship between SAR backscatter coefficient and water level in the freshwater marshes

The SAR backscatter coefficient is affected by several features of the wetland surface (i.e., the dielectric constant, vegetation type, vegetation density, and water level beneath the vegetation canopy), and radar wavelength and polarization. In case of swamps (i.e., forested wetlands), high water reinforces double-bounce scattering to amplify the backscatter coefficient. However, water level fluctuations and backscattering coefficients are not highly correlated in swamps. In addition, when water levels increase in forested and herbaceous wetlands, C-band VV polarized SAR backscatter is decreased and the correlation between water level and SAR intensity becomes low (Kasischke et al., 2003). Therefore to-date, water level has been mostly estimated using in-situ gage data, and, backscatter coefficient has only been used to characterize and quantify vegetation distribution or land cover change.

With herbaceous marshes such as the sawgrass-dominated areas of the Everglades WCAs and using longer wavelength SAR with horizontal polarization, water levels and backscatter coefficients appear to be correlated. This relationship is revealed by comparison of SAR backscatter and EDEN gage data. Figure 3.4(a) ~ (f) shows the relationship between water height from multiple gages and backscatter coefficient from ALOS PALSAR intensity images. The inverse linear relationship shows that increased water height lowers the SAR backscatter coefficient from freshwater marshes. These SAR images are from both FB (path 149 and 464) and ScanSAR (path 466) modes.

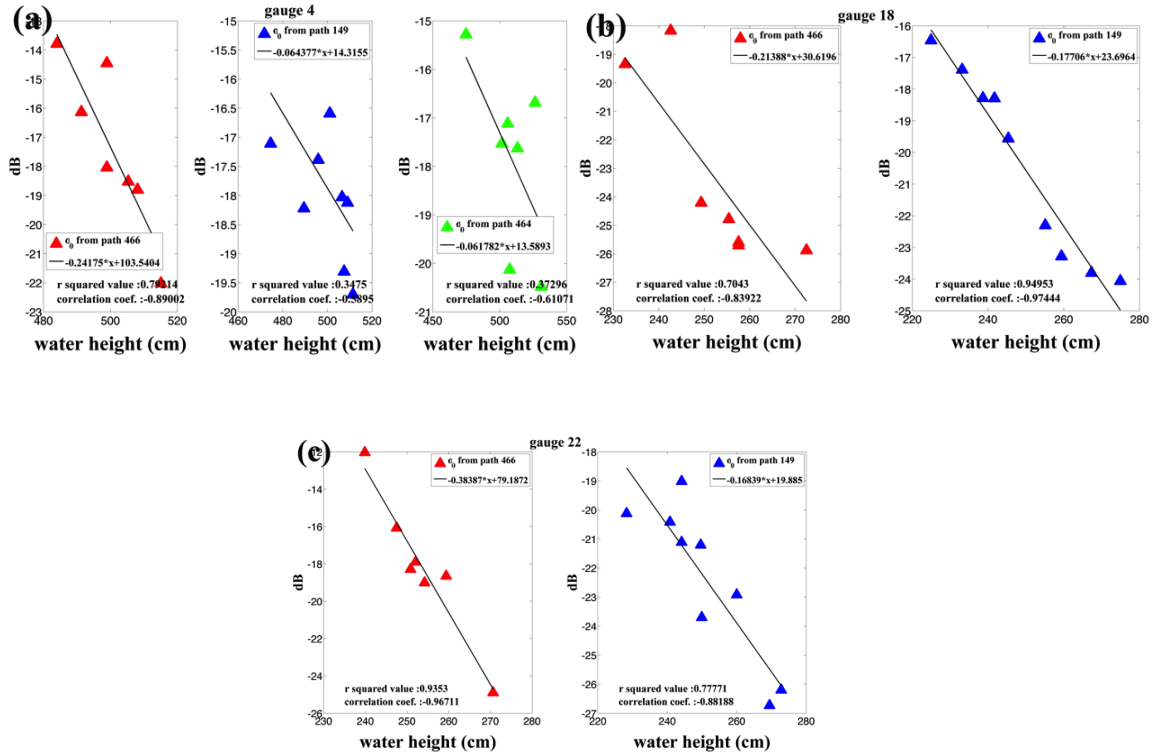

Continued

Figure 3.4. Comparison between ALOS PALSAR backscattering coefficients from path 466, 149, and 464 and water height from gauge No. 4(a), 18(b), 22(c), 23(d), 30(e), and 37(f).

Figure 3.4 continued

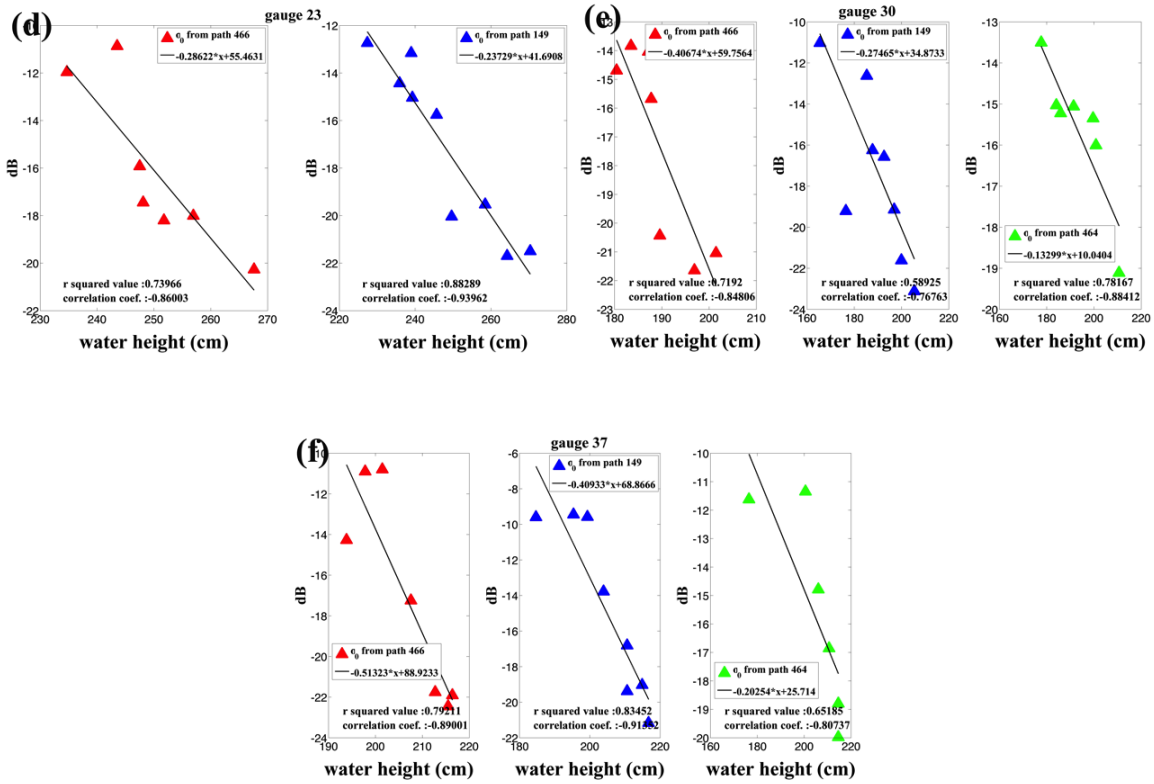

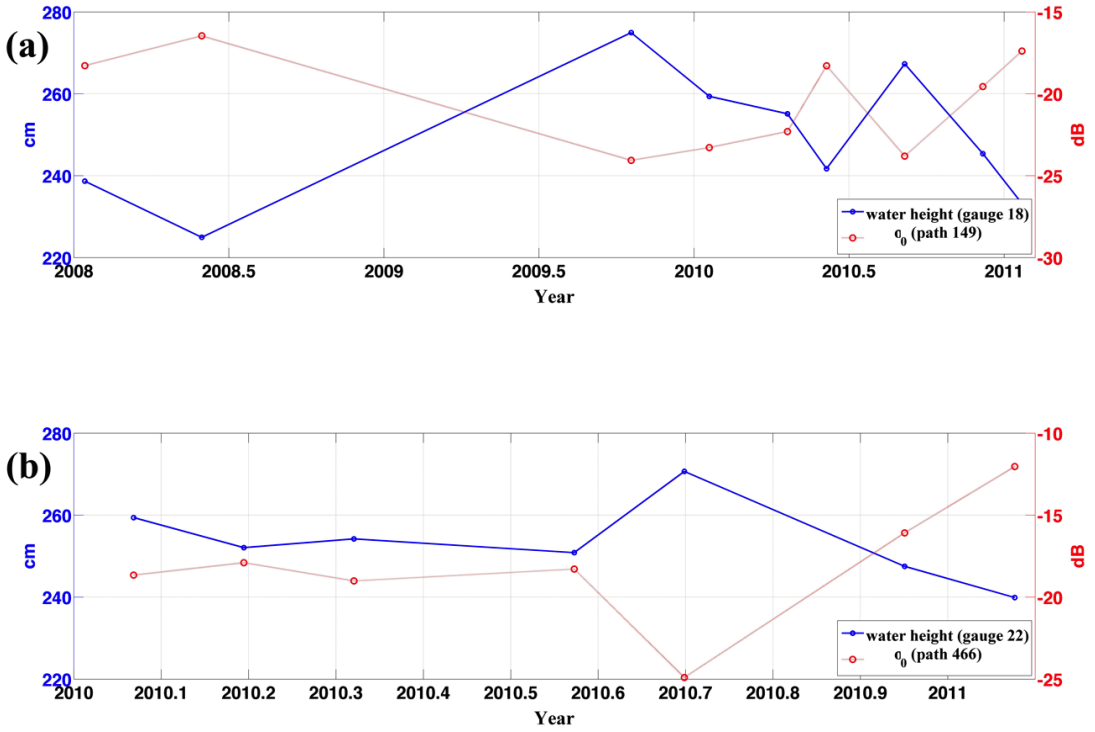

Figure 3.5. (a) Temporal change of backscatter coefficients from ALOS PALSAR Fine-beam mode path 149 and water height at gauge No. 18 corresponding to the location of SAR intensity (b) Temporal change of backscatter coefficient from ALOS ScanSAR path 466 and water height at gauge No. 22 corresponding to the location of SAR intensity.

Backscatter coefficients from path 149 and 466 produced highly negative correlation coefficients with water height (-0.9 to -0.7). However, products from path 464 generated a relatively low correlation coefficient of about -0.6. It is difficult to determine the exact cause of this lower correlation, but this study suspects that the relatively low number of observations from ALOS PALSAR path 464 given its limited coverage over our interest areas, and its large incidence angle from the far-range observation both contribute to this correlation. Because intensity images from path 466 and 149 exhibited highly negative correlations with water height, these data were the focus of additional further analysis. The fact that the data of path 466 and 149 are respectively from ScanSAR and FB mode implies that differences in resolution and satellite flight direction of SAR dataset are not contributing factors. In Figure 3.5(a) and (b), water level and SAR backscatter coefficients exhibit nearly exact opposite pattern. These figures also suggest that high water reduces backscatter from freshwater marsh. While this study observes that different data acquisition methods of FB and ScanSAR do not impact the relationship between water levels and backscatter, the SAR wavelength does. Figure 3.6(a) ~ (f) shows that backscatter from the shorter wavelength (5.6 cm) of C-band Radarsat-1 has a much lower correlation coefficient (~ −0.1) with gaged water heights than the longer

wavelength L-band ALOS data. This reaffirms previous findings that suggested C-band backscatter coefficients do not have meaningful relationship with water level.

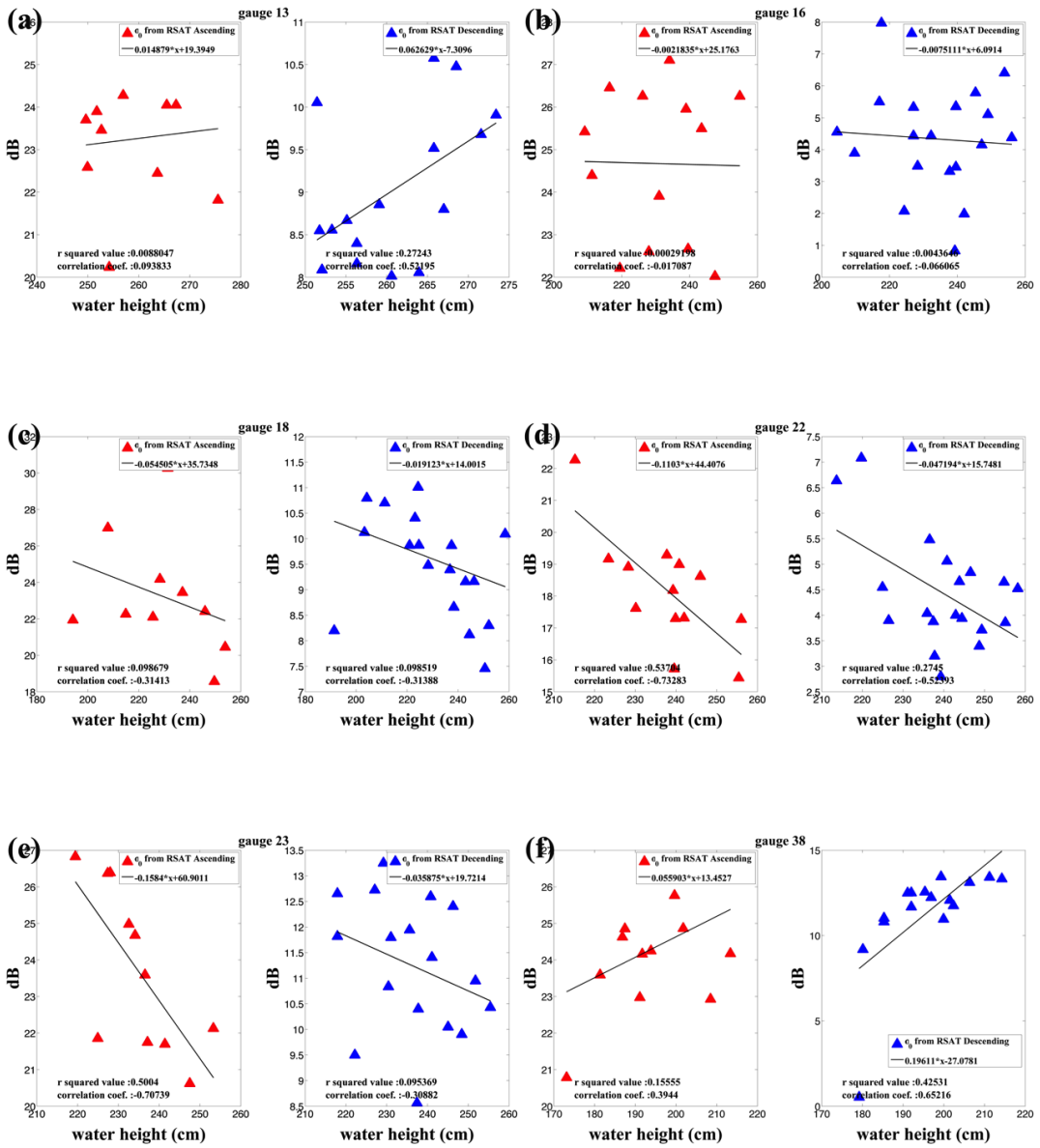

Figure 3.6. Comparison between Radarsat-1 backscattering coefficients from ascending and descending track and water height from gauge No. 13(a), 16(b), 18(c), 22(d), 23(e), and 38(f). Red and blue triangles show decibel from SAR intensity and water height at gauges in the location. Each solid line represents linearly fit line from two components, and r squared value and correlation coefficient indicates the strength of linear relationship.

Table 3.3 summarizes results of comparisons among backscatter and water level at 38 EDEN gage sites as a function of land cover type (i.e., mixed shrubs, graminoid prairie and sawgrass) and multiple radar configurations (two modes of ALOS PALSAR and Radarsat-1). Although the number of observations within some land cover classes is low, backscatter and water levels exhibit different relationships as a function of land cover. Low correlations (~ −0.1) occurred over mixed shrubs. These wetland areas have conditions similar to swamp forests, in which woody stems contribute to non-proportional scattering characteristics between radar backscatter and water level. However, for the graminoid and sawgrass marshes, backscatter coefficients from ALOS PALSAR images produce relatively high mean r-squared values of approximately 0.5 ~ 0.6 and correlation coefficients of −0.69 ~ −0.63 in path 466 (ScanSAR) and 149 (FB). As previously shown in Figure 3.4 and 3.6, data from path 464 (FB) and C-band Radarsat-1 produced low r-squared values (0 ~ 0.3) and correlation coefficients (-0.3 ~ 0). Thus one sees that two different vegetation types of graminoid prairie dominated by cattail and sawgrass do not have a large effect on the relationship between backscatter coefficients and water height, while radar-operating band has a major impact on this relationship. Scattering mechanisms between C-band radar signal and target surface are not dominated by the single source of water level change, but instead are affected by multiple sources including vegetation composition.

The L-band radar signal from ALOS PALSAR appears to be largely influenced by water level beneath vegetation in Everglades marshes. However, other factors such as seasonal variation in vegetation cover may still influence backscatter. Figure 3.7 shows the relationship between water heights at all gages and backscatter coefficients from ALOS PALSAR path 466 and 149 as averaged by SAR acquisition date. High and negative correlations (-0.7 ~ -0.6) between water level and backscatter continue to suggest it is possible to estimate water height from L-band SAR backscatter coefficients. The figure confirms that when water level increases in the freshwater marsh, the backscatter coefficient of both fine-beam and ScanSAR mode SAR data is linearly decreased. However, large variations in backscatter coefficient (standard deviation of about 3 dB) within SAR acquisitions suggest that there are limits to high-accuracy water height estimation using only SAR backscatter coefficient given complicated wetland conditions. L-band SAR radar backscatter is somewhat affected by seasonal variation of wetland vegetation. Figure 3.8(a) and (b) represents the seasonal variation of backscattering coefficient from fine-beam (P149) and ScanSAR (P466) in the sawgrass and graminoid prairie marshes over the study period. Usually, radar echoes from graminoid prairie marsh (blue square) are stronger than those from sawgrass-covered marsh (red cross) because of nearly 3dB difference between two mean radar backscatter coefficients.

Nearly 80% of the annual precipitation in the Everglades occurs in the wet season (May to October) and often drought conditions prevail in the dry season (November to April). In most years, water level reaches its peak in the fall (September) while lowest levels occur during spring (March and April) (Kasischke et al., 2003). The water levels measured at the inland EDEN gages followed this annual cycle, as shown in Figure 3.9(a) (However drought conditions during the dry season of 2009 led to many missing values as water levels are not recorded when below the ground surface). For better comparison,

the mean water level at inland water gages and backscatter coefficient from path 149 between late 2009 and early 2011 are shown in Figure 3.9(b). Again, when water levels increases or peaks, the backscatter coefficient in the freshwater marshes (sawgrass and graminoid prairie) decreases. That is, the backscatter coefficient in the marshes tends toward the opposite direction of water level changes. Seasonal variation of the backscatter coefficient is largely affected by hydrologic variation, not biomass, soil moisture, or phenologic changes in vegetation. But it is important to note that in this regarding the Everglades may present a best-case condition in terms of water level variation as a dominant scattering mechanism. Leaf-on and leaf-off conditions of grasses in Everglades marshes may not have as strong a seasonal component or as large an impact on the scattering of long wavelength radar signal than might be the case in other more temperate herbaceous wetlands.

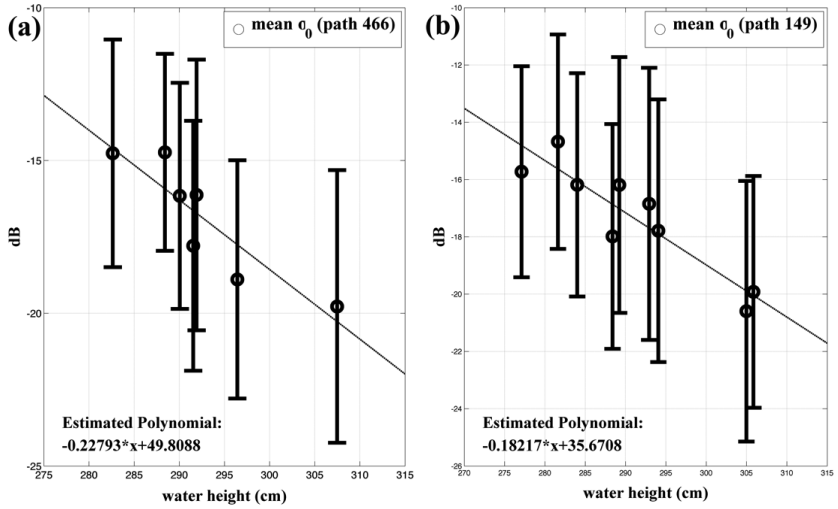

Figure 3.7. Mean backscattering coefficient ((a) path 466 and (b) 149) and water height from each SAR date. Black circles represent averaged backscatter coefficient and length of error bars mean a standard deviation. Dotted lines are a linearly fit line from mean backscatter coefficient and water height.

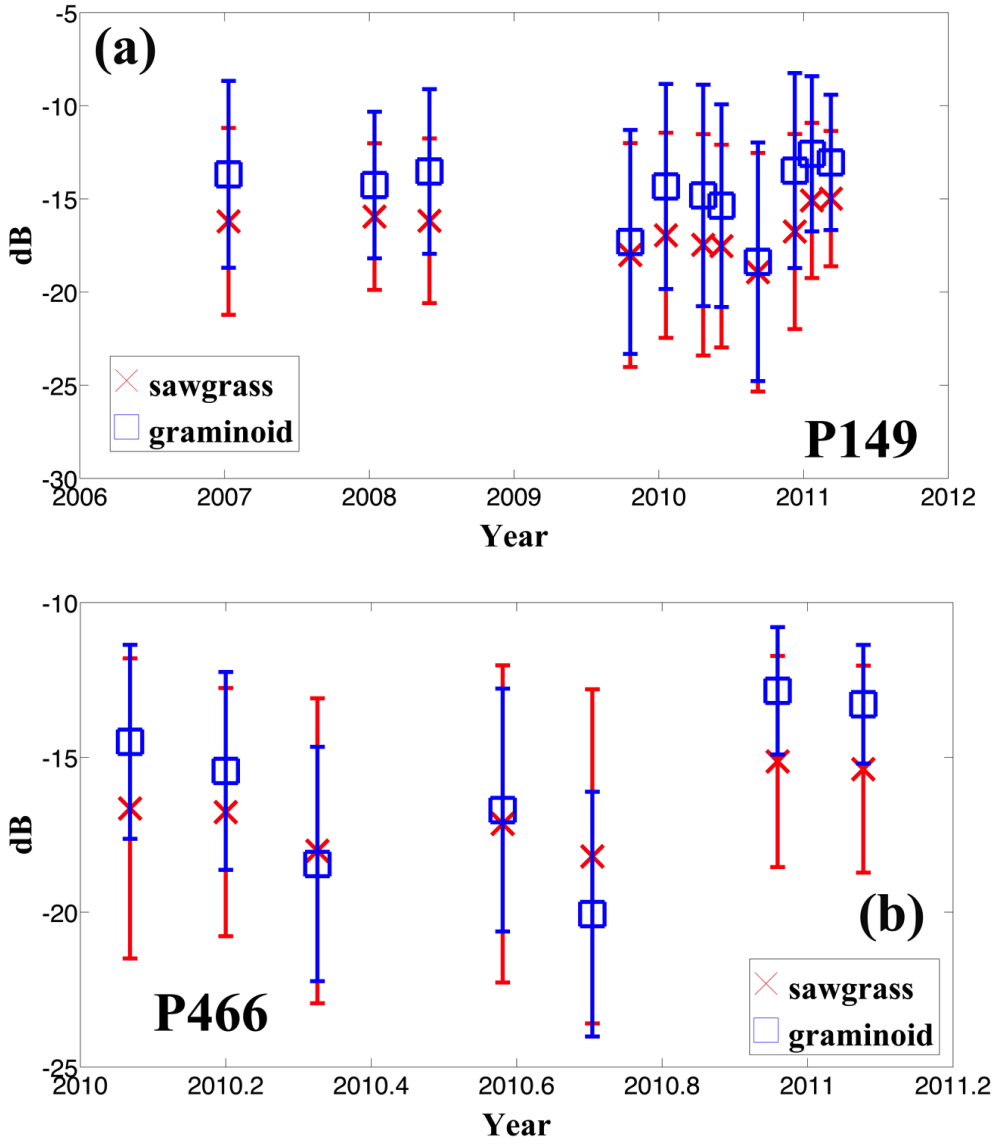

Figure 3.8. Mean backscatter coefficient of ALOS PALSAR Fine-beam mode P149 (a) and ScanSAR mode P466 (b) in the freshwater marshes of sawgrass (red) and graminoid (blue) between 2006 and early 2011 (P466 between 2010 and early 2011). Red cross and blue square markers represent the mean value and error bars show a standard deviation of each backscatter coefficient in time span.

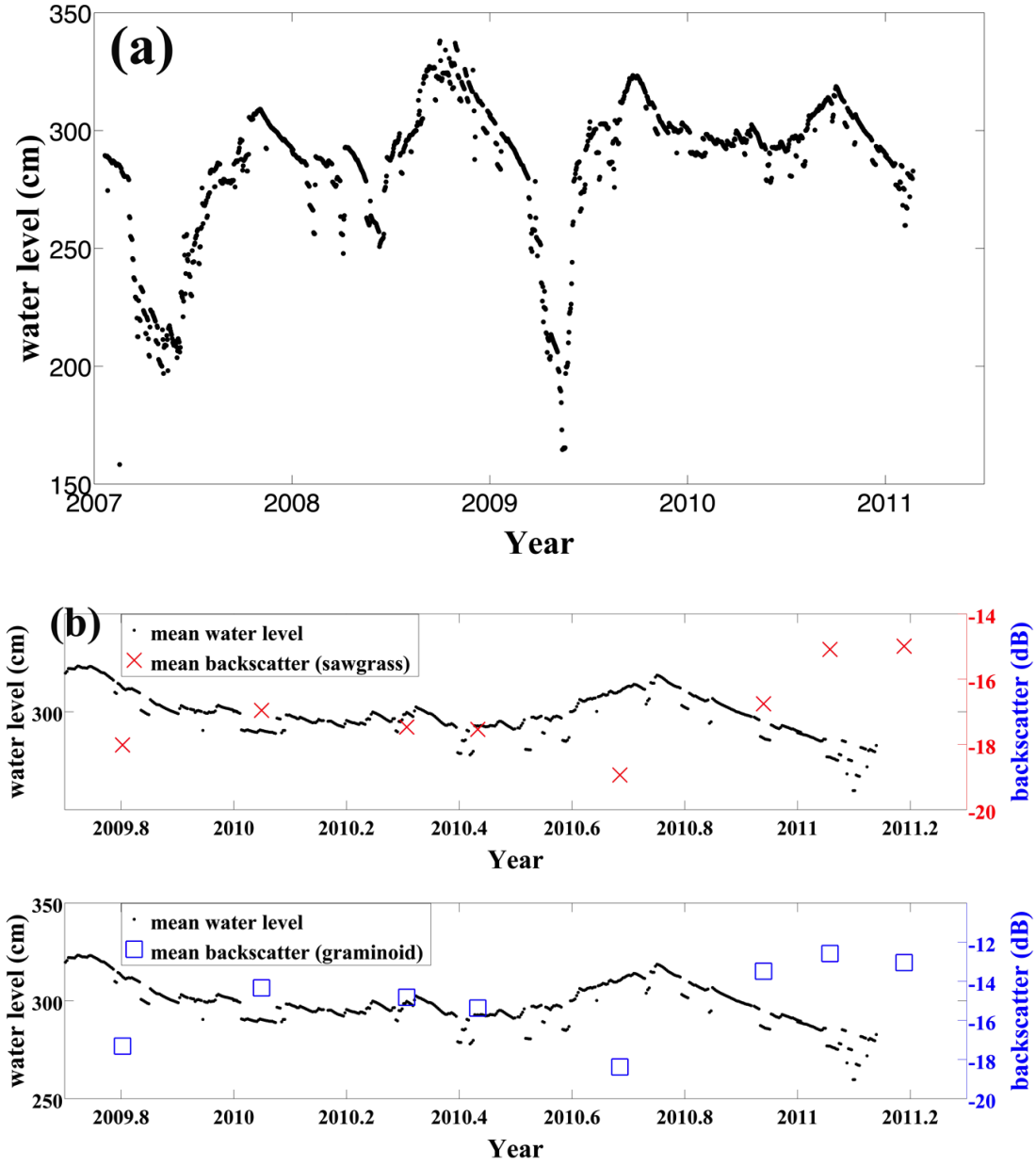

Figure 3.9. (a) Mean water level from wetland water level gauges in the freshwater marshes of sawgrass and grminoid prairie between 2007 and early 2011. (b) Mean water level from wetland water level gauges in Figure 3.9(a) and mean backscatter coefficient of sawgrass (red cross) and graminoid prairie (blue squares) marshes in Figure 3.8(a) between late 2009 and early 2011.

Gauge number	Land cover	ALOS PALSAR						Radarsat-1			
		P466		P149		P464		Ascending		Descending	
		r-squared	cor. coef.	r-squared	cor. coef.	r-squared	cor. coef.	r-squared	cor. coef.	r-squared	cor. coef.
1	Mixed Shrubs	0.030	-0.174	-	-	-	-	0.015	-0.121	-	-
2	Mixed Shrubs	0.022	0.150	-	-	-	-	0.000	-0.012	-	-
Mean (Mixed Shrubs)		**0.026**	**-0.012**	**-**	**-**	**-**	**-**	**0.007**	**-0.066**	**-**	**-**
Std (Mixed Shrubs)		**0.006**	**0.229**	**-**	**-**	**-**	**-**	**0.010**	**0.077**	**-**	**-**
3	Graminoid Prarie	0.822	-0.906	0.006	-0.079	0.165	-0.406	-	-	0.063	0.251
4	Graminoid Prarie	0.792	-0.890	0.348	-0.589	0.373	-0.611	-	-	0.009	0.097
5	Graminoid Prarie	0.026	0.160	0.313	-0.560	0.366	0.605	-	-	0.237	-0.486
6	Graminoid Prarie	0.172	0.414	0.530	-0.728	0.061	-0.247	-	-	0.796	-0.892
9	Graminoid Prarie	0.848	-0.921	0.505	-0.710	0.367	-0.606	-	-	0.001	-0.031
12	Graminoid Prarie	0.000	0.021	0.115	-0.338	0.008	0.090	-	-	0.043	-0.208
13	Graminoid Prarie	0.586	-0.766	0.322	-0.567	-	-	0.009	0.094	0.272	0.522
14	Graminoid Prarie	0.505	-0.710	0.145	-0.381	0.000	0.006	-	-	0.675	-0.821
15	Graminoid Prarie	0.674	-0.821	0.798	-0.894	-	-	0.066	-0.258	-	-
16	Graminoid Prarie	0.702	-0.838	0.550	-0.741	-	-	0.000	-0.017	0.004	-0.066
18	Graminoid Prarie	0.704	-0.839	0.950	-0.974	-	-	0.099	-0.314	0.099	-0.314
20	Graminoid Prarie	0.211	-0.459	0.593	-0.770	-	-	0.281	-0.530	-	-
21	Graminoid Prarie	0.424	-0.651	0.818	-0.904	-	-	0.004	0.065	0.231	-0.481
22	Graminoid Prarie	0.935	-0.967	0.778	-0.882	-	-	0.537	-0.733	0.274	-0.524
23	Graminoid Prarie	0.740	-0.860	0.883	-0.940	-	-	0.500	-0.707	0.095	-0.309
24	Graminoid Prarie	0.802	-0.896	0.756	-0.869	-	-	0.130	-0.360	0.337	0.581
26	Graminoid Prarie	0.842	-0.918	0.695	-0.834	-	-	0.097	0.311	-	-
28	Graminoid Prarie	0.686	-0.828	0.855	-0.925	-	-	0.056	-0.236	0.203	0.450
29	Graminoid Prarie	0.212	-0.461	0.299	-0.546	-	-	0.279	-0.528	0.207	0.455
Mean (Graminoid Prarie)		**0.562**	**-0.639**	**0.540**	**-0.696**	**0.191**	**-0.167**	**0.171**	**-0.268**	**0.222**	**-0.111**
Std (Graminoid Prarie)		**0.298**	**0.404**	**0.286**	**0.240**	**0.174**	**0.437**	**0.187**	**0.330**	**0.229**	**0.473**

Continued

Table 3.3. r-squared value and correlation coefficient between water height from gauges and backscatter coefficients from SAR.

Table 3.3. continued

Gauge number	Land cover	ALOS PALSAR						Radarsat-1			
		P466		P149		P464		Ascending		Descending	
		r-squared	cor. coef.	r-squared	cor. coef.	r-squared	cor. coef.	r-squared	cor. coef.	r-squared	cor. coef.
7	Sawgrass	0.741	-0.861	0.521	-0.722	0.719	0.848	-	-	0.255	0.505
8	Sawgrass	0.583	-0.764	0.283	-0.532	0.232	-0.482	-	-	0.039	-0.197
10	Sawgrass	0.681	-0.825	0.759	-0.871	0.318	-0.564	-	-	0.009	0.092
11	Sawgrass	0.490	-0.700	0.638	-0.799	0.849	-0.922	-	-	0.229	0.478
17	Sawgrass	0.924	-0.961	0.483	-0.695	-	-	-	-	0.104	0.322
19	Sawgrass	0.772	-0.878	0.957	-0.978	-	-	0.029	-0.171	-	-
25	Sawgrass	0.039	-0.196	0.249	-0.499	-	-	0.008	0.087	-	-
27	Sawgrass	0.176	0.419	0.253	0.503	0.106	-0.325	-	-	0.489	0.699
30	Sawgrass	0.719	-0.848	0.589	-0.768	0.782	-0.884	-	-	0.201	0.448
31	Sawgrass	0.696	-0.834	0.518	-0.720	0.689	-0.830	0.079	0.281	0.219	0.468
32	Sawgrass	0.444	0.666	0.095	-0.309	0.077	-0.277	0.007	0.082	0.666	0.816
33	Sawgrass	0.763	-0.874	0.485	-0.696	0.619	-0.787	0.583	-0.763	0.017	0.130
34	Sawgrass	0.891	-0.944	0.278	-0.527	0.118	-0.343	-	-	0.309	0.556
35	Sawgrass	0.569	-0.754	0.700	-0.837	0.498	-0.706	-	-	0.009	-0.093
36	Sawgrass	0.535	-0.732	0.580	-0.762	0.023	-0.153	0.009	0.096	0.025	0.159
37	Sawgrass	0.792	-0.890	0.835	-0.914	0.652	-0.807	0.011	-0.103	0.137	0.370
38	Sawgrass	0.414	-0.643	0.546	-0.739	0.081	0.285	0.156	0.394	0.425	0.652
Mean (Sawgrass)		**0.602**	**-0.625**	**0.516**	**-0.639**	**0.383**	**-0.355**	**0.110**	**-0.012**	**0.209**	**0.360**
Std (Sawgrass)		**0.238**	**0.474**	**0.230**	**0.338**	**0.304**	**0.499**	**0.198**	**0.355**	**0.197**	**0.291**

3.4.2. Relationship between interferometric phase, backscattering coefficients, and water level changes over the wetlands

Hydrologic variations in wetlands affect the phase of interferograms from C-band and L-band SAR datasets. But interferometric phase from differential interferograms must exclude signatures from topography, reduce baseline error, and suppress other noise to isolate the influence of water level changes within wetlands. In general, swamp forest regions have high coherence in interferograms (Kim et al., 2009), which enables phase unwrapping. This is a crucial process for estimating vertical displacement related to water level changes. However, interferograms in marsh regions are often disturbed by low coherence due to inconsistent scattering mechanisms and weak double-bounce scattering. Furthermore, because the temporal baseline of InSAR pairs over the freshwater marsh is a key factor in coherence, interferograms with temporal baselines larger than one revisiting cycle (46 days for ALOS PALSAR) rarely exhibit good coherence (e.g., > 0.2). For these reasons, InSAR pairs covering freshwater marsh require strong filtering to implement reliable phase unwrapping. Figure 3.10(a) shows a wrapped PALSAR interferogram for the study area produced from April, 21, 2010 and June, 06, 2010 images. Figure 3.10(b) was generated by subtracting backscatter coefficients from two similar types of PALSAR images collected across the period of transition between dry and wet seasons. The figure is cyclically colored by 10.0 dB to allow comparison with the wrapped interferogram. The interferogram in Figure 3.10(a) exhibits high coherence (~0.4) over wetland regions, but many parts of interferogram that cover freshwater marsh in the WCA 2 and 3A-3 lack the coherence. Only the high coherence (>0.2) areas are good enough for further InSAR analysis. At first glance, the two products of Figure 3.10(a) and (b) look similar in terms of spatial color changes and they suggest that water level changes in the wetlands have a notable effect on both backscatter coefficient as well as interferometric phases of SAR pairs.

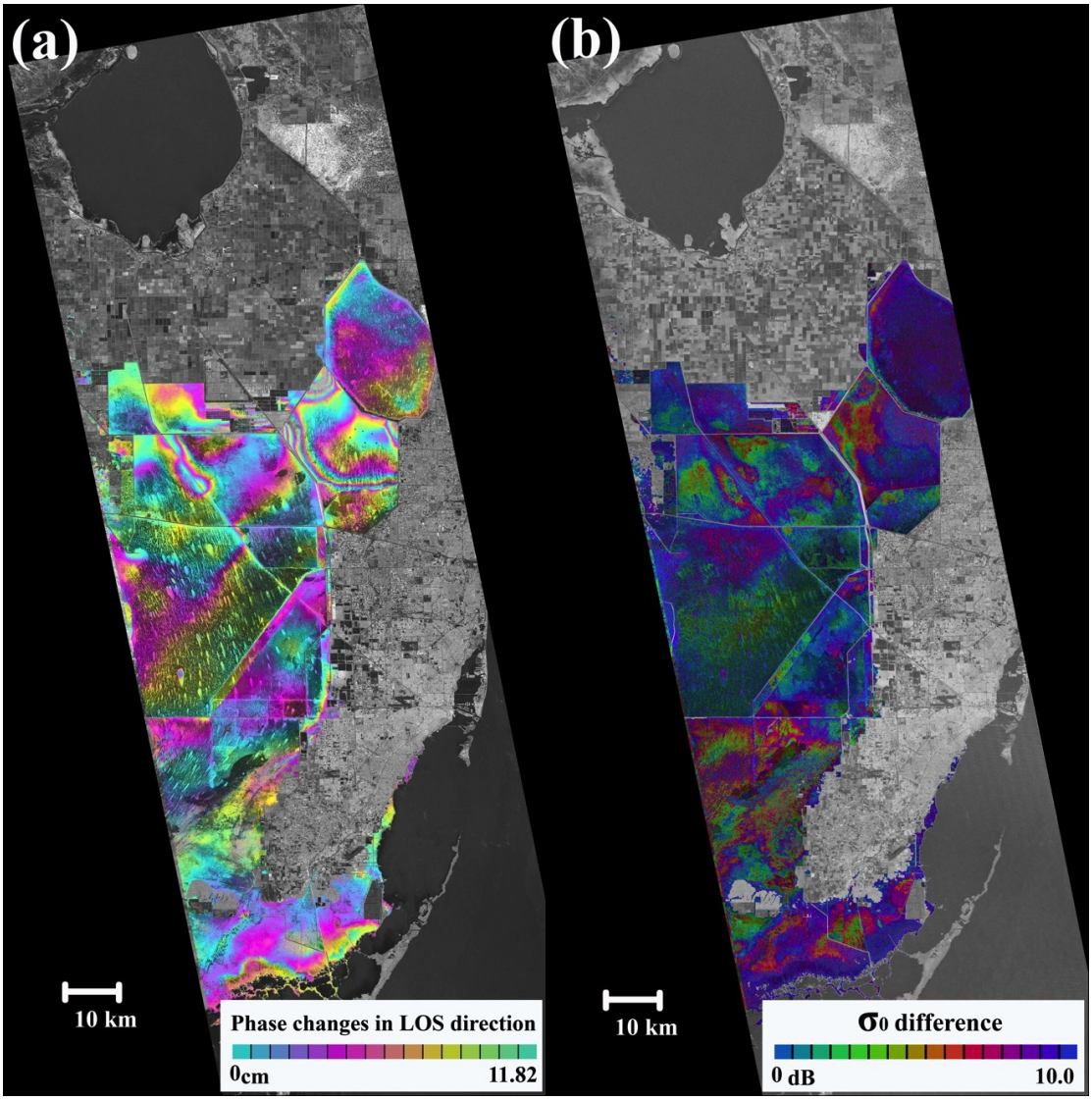

Figure 3.10. (a) Wrapped interferogram from ALOS PALSAR SAR data and (b) Difference of ALOS PALSAR Fine-beam mode backscatter coefficients in the Everglades, Florida, between 2010.04.21 and 2010.06.06. Due to inverse relationship of hydrologic change and backscatter in the marshes, Figure 3.10 (a) and (b) show similar pattern of spatial color change.

The Everglades subsection-by-subsection comparison in Figure 3.11 provides a more helpful view for evaluating similarities and differences in techniques. The wrapped interferograms in Figure 3.11 are from two pairs, April, 21, 2010 ~ June, 06, 2010 and June, 06, 2010 ~ September, 06, 2010. Their perpendicular baselines are 148.7242 and 208.2613 (m) respectively. These relatively small baselines enable high coherence over wetlands in the Everglades. The same two pairs of images were used to generate the differences of backscatter coefficients corresponding to the interferograms as shown in

Figure 3.11. The interferogram and backscatter coefficients are cyclically colored by interval of 11.82 cm and 10.0 dB.

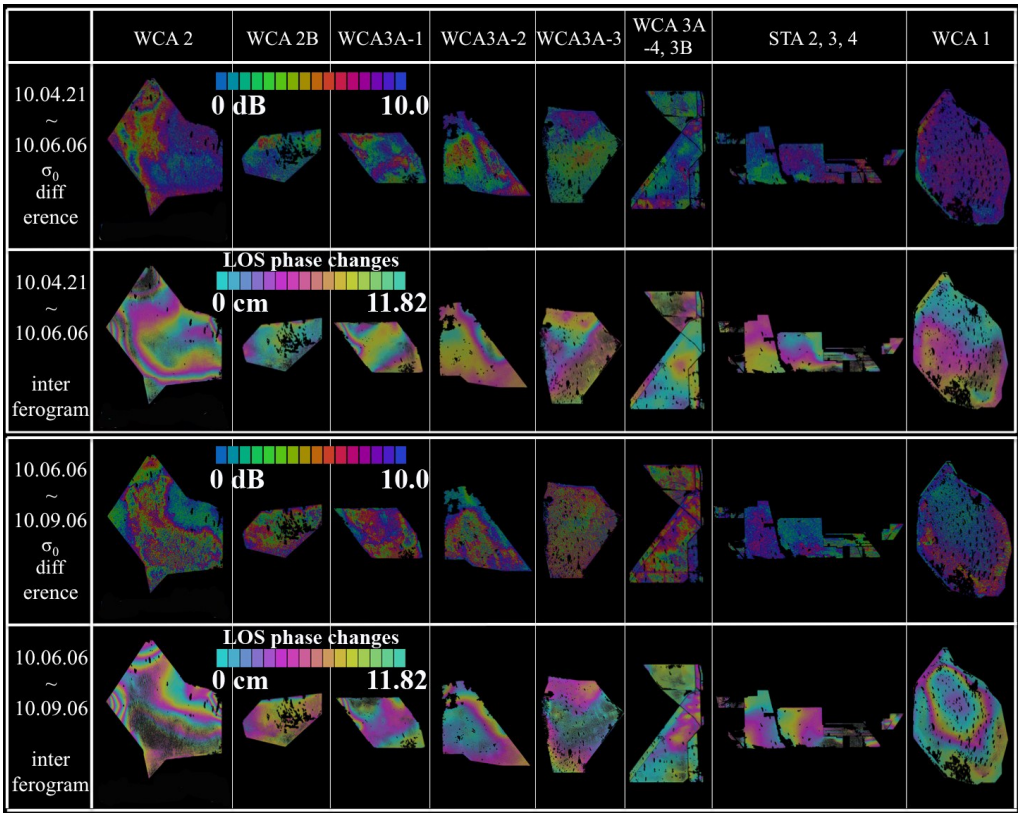

Figure 3.11. Difference of backscatter coefficient and wrapped interferogram over each section of Water Conservation Areas and Stormwater Treatment Areas from two ALOS Fine-beam mode pairs, 2010.04.21 ~ 2010.06.06 and 2010.06.06 ~ 2010.09.06.

The two approaches show similar types of color changes most sections. However, figures in sections of WCA 1 and WCA 3A-3 are notable for their lack of similarity due to the loss of coherence, different magnitudes of water level change, and differences in vegetation type (Figure 3.2). Many portions of WCA 1 and WCA 3A-3 where vegetation is mixed and dense do not reflect water level change patterns through differences of backscattering coefficients. However, phase information still includes water level variation in cases of high coherence. Given such conditions, interferograms are helpful for estimating high-resolution water level changes between two particular dates. However, while SAR interferometry detects hydrologic changes, it has a number of restrictions. InSAR pairs with large temporal or perpendicular baselines produce low coherence interferograms, and fringes for meaningful hydrologic changes may not be properly generated. Furthermore, ScanSAR-ScanSAR interferometry from ALOS PALSAR is not often feasible, because the bursts of ScanSAR are not fully synchronized in a revisiting date. The misalignment results in total decorrelation of SAR

interferograms. However, in such cases, our results suggest that difference of backscatter coefficients could help to estimate spatial water level change, replacing inadequate interferograms to a certain degree. In Figure 3.12, the differencing of backscatter coefficients and wrapped interferogram from a pair of PALSAR ScanSAR image from September, 13, 2010 and January, 29, 2011 shows similar patterns of changes. This is especially evident in WCA 2. The SAR pair has a perpendicular baseline of 426.6521 (m), and PALSAR ScanSAR-ScanSAR interferometry is available due to the synchronization of SAR bursts meaning enough overlaps between SAR observations. The burst synchronization is very rarely happening in PALSAR ScanSAR, and the other pair of July, 29, 2010 and September, 13, 2010 in Figure 3.12 does not generate a proper interferogram due to the loss of coherence. The difference of backscatter coefficient is always available, and approximate water level changes within wetlands of the Everglades can be estimated from differences in ScanSAR backscatter coefficients as shown in the lowest part of Figure 3.12.

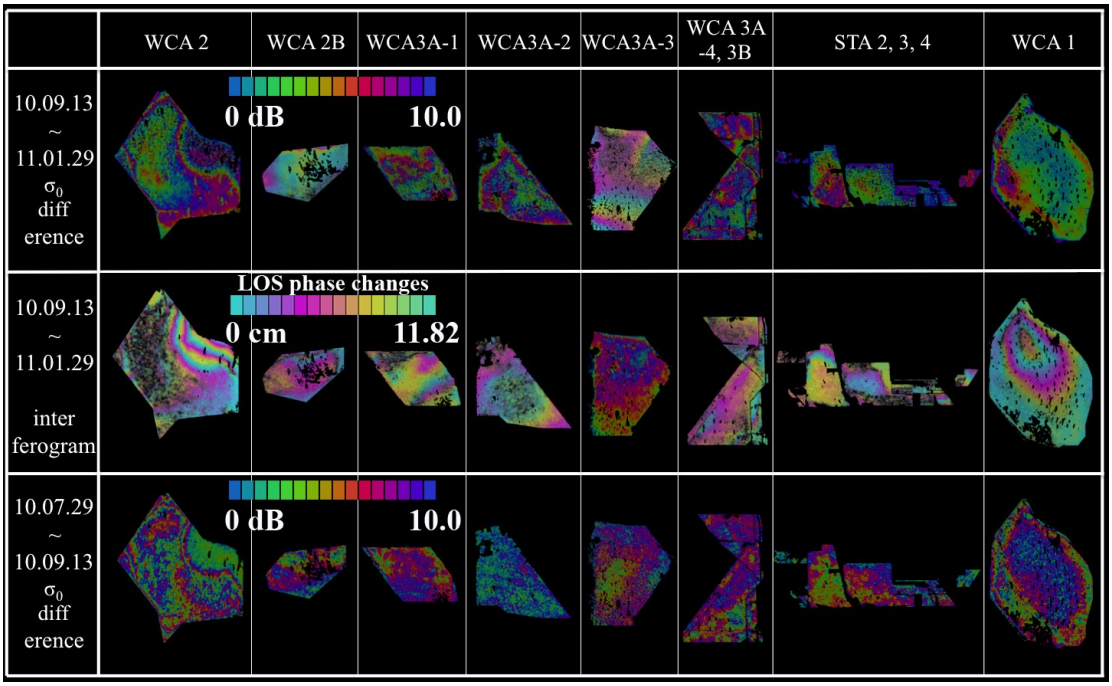

Figure 3.12. Difference of backscatter coefficient and wrapped interferogram over each section of Water Conservation Areas and Stormwater Treatment Areas from two ALOS ScanSAR pairs, 2010.09.13 ~ 2011.01.29 and 2010.07.29 ~ 2010.09.13. Also, an interferogram from one pair, 2010.07.29 and 2010.09.13, is missing, because ScanSAR-ScanSAR interferometry is not available due to a burst misalignment.

3.4.3. Complementarity of InSAR and SAR backscatter coefficient to estimate water level changes in the wetlands

The complementary uses of unwrapped interferometric phases and difference of backscatter coefficients are highlighted through their comparison with water level at EDEN gages of Figure 3.13. Unwrapped interferometric phases from two SAR pairs (red crosses) are sparser than differences of backscatter coefficients (blue dot) in the figure, because only high coherence pixels from an interferogram were unwrapped by avoiding errors by phase jumps. As water levels increase both unwrapped interferometric phases and difference of backscatter coefficient are decreased. It is the nature of interferometric phases that increases in water level decreases the relative distance between satellite and target as well as phase difference between nearby pixels of an unwrapped interferogram. Therefore, it makes sense that water level changes and unwrapped phase are highly correlated, as shown in Figure 3.13(a) and (b). Although water level change and difference of backscatter coefficients are relatively less correlated, the two parameters have an inverse linear relationship to a certain degree. Figure 3.13(a) and (b) support our assertion that it is possible to estimate water level changes at specific locations of freshwater marsh from differences in backscatter coefficient, in places or at times when L-band SAR interferometry is not possible.

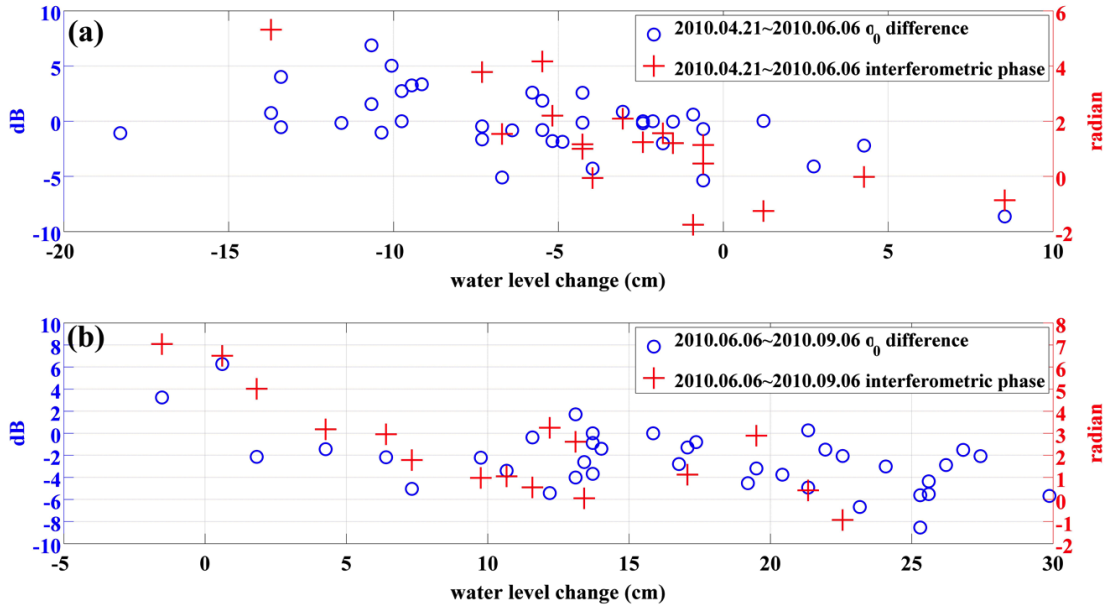

Figure 3.13. Comparison of difference of backscattering coefficient and unwrapped interferometric phase between (a) 2010.04.21 and 2010.06.06 and (b) 2010.06.06 and 2010.09.06. Blue circles are from difference of SAR intensity and its dimension is decibel. Moreover, red crosses are from unwrapped interferometric phase and its dimension is radian.

Use of backscatter coefficient and its differencing is not a total substitute for interferometry. Rather, InSAR can be used for deriving the reference water level change to obtain absolute water level change within the freshwater marsh as the fusion of radar altimetry and InSAR technology can be utilized for absolute water level change within swamp forests (Kim et al., 2009). Unfortunately, in the Everglades, the radar altimetry does not cross the major wetlands of the water conservation area or the Everglades National Park. Therefore the altimetry data cannot be used for a reference water level change. Additionally, while gage data have been used with InSAR for detailed estimation of water level changes, gages may often fall in the low coherence areas, making the combination of gage data and InSAR infeasible. However, because of a close relationship between L-band radar backscatter and water level in the freshwater marsh, the hydrologic change estimated from the backscatter coefficient can be used for a reference water level change (Kim et al., 2005). This study used two pairs from FB interferometry (2010.04.21 ~ 2010.06.06) and ScanSAR-ScanSAR interferometry (2010.09.13 ~ 2011. 01. 29) to test this possibility combining the InSAR pair and the backscatter coefficient for this purpose. Two wrapped differential SAR interferograms were unwrapped using the minimum cost flow (MCF) algorithm, while excluding low-coherence area with values smaller than 0.2. In each section of water conservation area, the data with the highest r-squared value at the location of wetland gages (Table 3.3) was used. Also, the linear fitted equations between water level and backscatter coefficient were utilized for estimating hydrologic change in the SAR acquisition dates. The estimated water level and its subtraction between two SAR acquisition dates are approximated as water level change during the period of the InSAR pair, which represents high-resolution water level change within wetlands. The integration of unwrapped InSAR pair and a reference water level change at gages was validated using other wetland gages. The map of absolute water level change in Figure 3.14 was generated through this process. Each section of water conservation area in Figure 3.14 shows a different magnitude of water level change, because the segments are dissected by levees or canals (Jones et. al. 2012). The spatial hydrologic change in the map is induced by the sensitivity of InSAR to the movement of the water surface. The low-coherence area was not included in the generation of absolute water level change map to avoid the phase jumps and inaccurate reconstruction of actual water level change. When the wetland gages (WCA 1 for Fine pair and WCA 1, 2, and 3A-2 for ScanSAR pair) are located in the low-coherence region, the closest point of interferograms is used for the integration. Also, because there is no available wetland gage data for STA, the section was not included in Figure 3.14. The accuracy of absolute water level change from integration of SAR backscatter coefficient and interferograms was validated at other gages, and the result is shown in Table 3.4. The accuracy varies along with each section, and the range is between 1.2726 cm and 6.2981 cm. Moreover, there is no significant difference between two SAR observation modes acquired from descending and ascending track. The results suggest that the integration of SAR intensity and phase information to estimate absolute water level change is feasible. Also, the different condition of each section in water conservation area, such as biomass and density, affects the accuracy for the integration. A long history of L-band backscatter coefficient in the freshwater marsh can enhance the accuracy because of better derivation of linear relationship between radar backscatter and water level.

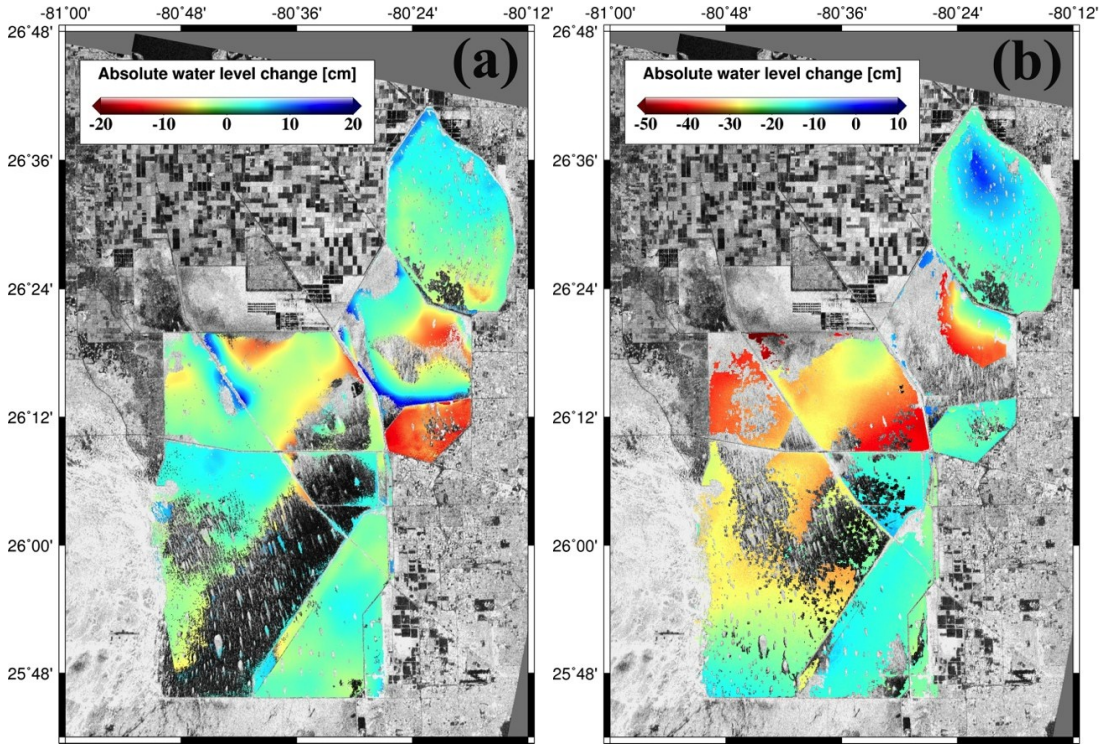

Figure 3.14. Absolute water level change using ALOS PALSAR InSAR pair ((a) Fine-beam mode 2010.04.21~2010.06.06 (b) ScanSAR mode 2010.09.13 ~ 2011.01.29) and reference water level change estimated from the relationship between backscatter coefficient and water level measured in wetland water level gauges.

Period	Beam mode	Section	RMSE (cm)
2010.04.21 ~ 2010.06.06	Fine	WCA 2	-
2010.04.21 ~ 2010.06.06	Fine	WCA 2B	2.5421
2010.04.21 ~ 2010.06.06	Fine	WCA 3A-1	6.2981
2010.04.21 ~ 2010.06.06	Fine	WCA 3A-2	1.2726
2010.04.21 ~ 2010.06.06	Fine	WCA 3A-3	3.9526
2010.04.21 ~ 2010.06.06	Fine	WCA 3A-4, 3B	2.3423
2010.04.21 ~ 2010.06.06	Fine	WCA 1	2.6158
2010.09.13 ~ 2011.01.29	ScanSAR	WCA 2	-
2010.09.13 ~ 2011.01.29	ScanSAR	WCA 2B	2.8023
2010.09.13 ~ 2011.01.29	ScanSAR	WCA 3A-1	4.7518
2010.09.13 ~ 2011.01.29	ScanSAR	WCA 3A-2	-
2010.09.13 ~ 2011.01.29	ScanSAR	WCA 3A-3	1.3665
2010.09.13 ~ 2011.01.29	ScanSAR	WCA 3A-4, 3B	3.7117
2010.09.13 ~ 2011.01.29	ScanSAR	WCA 1	1.5403

Table 3.4. Results of combining InSAR pairs and SAR backscatter coefficient validated at multiple water gauges within wetlands ("-" means that there is no available gauge data due to low coherence).

3.5. Conclusion

The adaptive management of Everglades restoration requires efficient and accurate monitoring of wetland hydrology at the highest temporal and finest spatial resolutions possible. Many scientists have worked to develop methods of combining the EDEN gage network with radar remote sensing technology to understand Everglades wetland hydrology. However, few have explored relationships among hydrologic variation and SAR backscatter coefficients.

To compare SAR backscatter coefficients and Everglades water levels, this study combined ALOS PALSAR L-band and Radarsat-1 C-band data with daily mean water heights derived from the EDEN. While the various wavelengths and polarizations of these sensors are affected differently by various potential scattering mechanisms, we found that L-band SAR backscatter coefficients are closely related to water level in freshwater marshes of the Everglades. C-band radar does not produce a reasonable relationship with the fluctuation of water level, because components other than hydrologic change, such as vegetation composition, structure and density affect the radar backscattering. However, L-band backscatter coefficients in the freshwater marsh of the Everglades are dominated by the single factor of water level fluctuation. A close relationship between L-band SAR backscatter coefficients and water level implies that approximate water level can be estimated from L-band SAR backscatter coefficients.

SAR interferometry provides detailed hydrologic information when coherence is maintained and interferometric phases are able to unveil relative water level changes

between particular dates. But low coherence often occurs in the InSAR pairs with large temporal and spatial baseline or without enough double-bounce scattering. Comparison with interferograms, which were assumed to provide measures of real spatial water level change, made it clear that hydrologic changes affect the difference of backscatter coefficients as well as interferometric phase. Integrating water level change derived from L-band backscatter and InSAR pairs can estimate absolute water level change in the freshwater marsh. The accuracy of absolute water level change estimated from our integration of FB and ScanSAR mode ALOS PALSAR data, suggests meaningful hydrologic monitoring is possible. Further, it may be feasible and appropriate to use L-band SAR backscatter coefficients in place of SAR interferometry when low coherence disturbs the generation of a proper interferograms or ScanSAR-ScanSAR interferometry is not available.

Although our research shows that SAR backscatter coefficients can be useful for understanding wetland hydrology in the Everglades, it should be recognized that SAR intensity data is noisy and backscatter coefficients still include numerous effects of non-hydrological changes. Even well-known filtering techniques of lee, gamma, frost, and median filter cannot eliminate all the noise. It is not easy to distinguish hydrologic change signatures from others such as seasonal variation of vegetation and weather conditions. Thus, better filtering of SAR intensity and discriminating water level changes on backscatter coefficients from others requires a further study. For all these reasons, broader application of radar backscatter coefficient analysis for the purpose of mapping temporal and spatial changes in Everglades wetland water levels is feasible.

CHAPTER 4: Ground Subsidence in Tucson, Arizona, Monitored by Time-series Analysis Using Multi-sensor InSAR Datasets from 1993 to 2011

4.1 Introduction

In arid lands, the groundwater is a major source for supplying drinking water to residents, irrigating plants for agriculture, and flowing into lakes or rivers. The rain water, snowmelt, and inflow from upper watershed leads into the recharge of groundwater, and the discharge is made by natural flow and human demands for industrial, municipal, and agricultural purpose. Natural condition is balancing between recharge and discharge, but the balance has been threatened by extreme consumption of groundwater for developing arid areas of Phoenix and Nevada in the United States, Libya, and India. The groundwater depletion caused the disappearance of a crucial water resource as well as the aquifer-system compaction and ground subsidence. More than 80 percent of the identified subsidence in the United States is caused by human activities on subsurface water (Galloway et al., 2000). To conserve the groundwater and circumvent more rapid consumption from the subsurface, the elaborate resource management and intensive governmental efforts are required.

In Tucson, Arizona, the groundwater has been a critical resource for urban and rural communities, and the rapid urbanization and growing population has been heavily dependent on groundwater because of the lack of surface water. The excessive consumption of groundwater led to the decrease of water table as much as 14 meters between 1989 and 2005, and the declined water level before 1989 was much bigger than the number (Carruth et al., 2007). The groundwater pumping in excess of natural recharge was the major cause of aquifer-system compaction and associated land subsidence in Tucson area (Pool and Anderson, 2007). Since the Arizona's 1980 Groundwater Management Act, the temporal variations of groundwater table, soil compaction, and land subsidence have been monitored by gauges in wells, borehole extensometers, and annual GPS survey at multiple stations (Carruth et al., 2007; Pool and Anderson, 2007). The methods provide a good precision of measurement on subsurface condition, but each has limitation in detecting land-surface motion over large areas associated with groundwater depletion. For example, the water level at wells is not highly correlated with surface deformation in many cases, and the extensometers cannot measure the compaction occurring below the anchor depth of the devices. The annual GPS survey in sparse stations, which is labor-intensive, does not measure the surface displacement with high accuracy like continuous GPS. In contrast, the spatially detailed images of ground displacements generated from SAR interferometry (InSAR) can help to monitor the ground subsidence in Tucson.

The InSAR is an invaluable tool for measuring displacements over a large area with high accuracy of sub-centimeter and high spatial resolution of 30 meter after spatial averaging and geocoding. The InSAR processing for detecting displacements after

removing topographic, atmospheric, and orbital error phase is particularly called the differential InSAR (DInSAR). The DInSAR (Hanssen, 2001) has been used for detecting horizontal and vertical displacements by catastrophic natural disasters of earthquakes (Tong et al., 2010) and volcanoes (Lu et al., 2007), anthropologic deformation caused by mining and oil/gas extraction, and deformation by melting of permafrost (Samsonov et al., 2011).

In particular, the DInSAR was demonstrated for measuring the surface displacement related to aquifer system compaction and uplift accompanying groundwater discharge and recharge (Lu and Danskin, 2001; Galloway and Hoffman, 2007). Several researchers (Galloway et al., 1998; Hoffmann et al., 2003) mapped aquifer-system compaction and subsidence in the Antelope Valley, California, by integrating DInSAR, GPS and extensometers, and successfully estimated the groundwater flow, storage change, and compaction over large areas. The water decline and clay thickness map in Las Vegas Valley was analyzed with subsidence map based on DInSAR, GPS, and leveling (Amelung et al., 1999; Bell et al., 2002) and inelastic and elastic deformation by seasonal variation was detected by DInSAR time-series analysis. *Schmidt* and *Burgmann* (Schmidt and Burgmann, 2003) used the DInSAR for surface subsidence by groundwater extraction in Santa Clara Valley, California and found the Silver Creek Fault to disrupt the groundwater flow and cause steep displacement gradients. The recent advance in the DInSAR technology can improve the accuracy of surface deformation measurements. The small baseline subset (SBAS) algorithm (Berardino et al., 2002) uses multi-temporal InSAR images of small baselines to enhance the understanding of the underlying deformation process in the groundwater-withdrawn region with dense temporal interval. The SBAS resolve time-series displacement from the inversion of a set of matrix including interferometric and incremental phases. The advantage of SBAS technique is that it could minimize the atmospheric phase in InSAR pairs, capture the pattern of deformation in time and space, and estimate non-linear time series of deformation during a long time span by analyzing DInSAR pairs with short perpendicular baselines (Berardino et al. 2002; Lanari et al., 2004; Samsonov et al., 2011).

In this study, the SBAS InSAR technology was applied for detecting ground subsidence in Tucson, caused by groundwater depletion. Using sufficient SAR data archive from early 1990s to 2011, the spatial extent and magnitude of surface deformation in Tucson has been estimated. Our study utilized ERS-1/2, ENVISAT, and ALOS PALSAR, and the results of multi-sensor SBAS InSAR processing are analyzed in spatio-temporal scale with supplementary data from gauges, extensometers, and GPS survey.

4.2 Methodology

Before performing SBAS InSAR processing, a standard DInSAR processing with small perpendicular baselines is required. The N interferograms are generated from M SAR images by multiplying master complex image with a conjugate of slave complex SAR data. The interferometric phase of each interferogram is composed of a phase component by deformation, topography, orbital error, atmosphere, and random noise

term, respectively. The phase components besides deformation are reduced by digital elevation model (DEM), least-square fitted 2nd order polynomial, and filtering. Because topography provided by DEM sources has relative error terms and atmospheric phase is not easy to be removed from a single InSAR pair, the deformation phase cannot be obtained reliably. If there is no phase unwrapping error, the observed interferometric phase ϕ_{ifgs}^{k} of kth differential interferogram consists of deformation ϕ_{def}^{k}, topographic ϕ_{topo}^{k}, and atmospheric ϕ_{atm}^{k} (Samsonov, 2010),

$$\phi_{ifgs}^{k} = \phi_{def}^{k} + \phi_{topo}^{k} + \phi_{atm}^{k} \tag{4.1}$$

In Equation 4.1, both topographic phase and atmospheric phase terms are related to errors and residuals in DInSAR processing. The residual topographic phase term is estimated as (Berardino et al., 2002),

$$\phi_{topo}^{k} = \frac{B_{\perp} \cdot \triangle z}{R \cdot \sin\theta} \tag{4.2}$$

where R is the line-of-sight distance between a satellite and a target, θ is an incidence angle, $B_{\perp}$ is a perpendicular baseline, and $\triangle z$ is topographic error term. The atmospheric phase can be classified into turbulent mixing and vertical stratification contributions (Hanssen, 2001). The turbulent contributions are considered as a random phase both in space and time while the vertical stratification contribution is correlated with elevation (Delacourt et al., 1998; Beauducel et al., 2000; Chaabane et al., 2007; López-Quiroz et al., 2009). Removing the effect by vertical stratification is relatively easy step by using a linear correlation between interferometric phase from each interferogram and elevation from DEM, and the turbulent contribution can be reduced by computing a least square solution from many interferograms acquired under favorable conditions (Samsonov et al., 2013). The key feature of SBAS InSAR is that it can reduce the random atmospheric phase from many InSAR pairs as well as estimating topographic error terms related to the perpendicular baseline.

To integrate the InSAR pairs from multi-sensor, additional process is needed to correct the effect by the different wavelengths. As proposed by a previous study (Pepe et al., 2005), ERS and ENVISAT SAR sensors have different center frequency (5.30 GHz for ERS-1/2 and 5.33 GHz for ENVISAT ASAR) and it is impossible to generate interferogram from ERS/ENVISAR pairs under normal conditions. Instead, the ENVISAT InSAR pairs can be integrated into SBAS algorithm, by multiplying the correction term ($\lambda_{ENVISAT} / \lambda_{ERS}$, λ_{ERS}=5.656 cm and $\lambda_{ENVISAT}$=5.624 cm). If the track of ENVISAT and ERS is identical, the incidence angle of ERS and ENVISAT is similar in most cases.

The fundamental equation for SBAS can be expressed as the following form,

$$Bv = \Phi_{ifgs} \tag{4.3}$$

where *B* matrix has dimensions of *N* by *M-1* (*N* and *M* are the numbers of interferograms and SAR images, respectively), Φ_{ifgs} $(N \times 1)$ is a vector of observed interferometric phase ϕ_{ifgs}^{k}, and *v* vector consists of *M-1* velocities to be calculated. The *v* vector is unknown as,

$$v^T = \begin{pmatrix} v_1 = \dfrac{\phi_1^{inc}}{t_2 - t_1} & \cdots & v_k = \dfrac{\phi_k^{inc}}{t_{k+1} - t_k} & \cdots & v_{M-1} = \dfrac{\phi_{M-1}^{inc}}{t_M - t_{M-1}} \end{pmatrix} \tag{4.4}$$

where ϕ_k^{inc} is an incremental phase from t_k to t_{k+1}. In *B* matrix, if a k[th] interferogram spans the time represented by the column *n*, then the b_n^k term is equal to the time interval between the consequent images, otherwise zero (Berardino et al., 2002; Samsonov, 2010). In order to correct the topographic error, a perpendicular baseline of each interferogram should be attached to the right side of the *B* matrix. Additionally, in low coherence areas, the interferometric phase is set to zero, and the phase value should be excluded for SBAS analysis.

For example, if this study assumes that four SAR images are acquired at time of $t_1, \rightleftharpoons, t_4$ five interferograms are generated from intervals $t_2 - t_1$, $t_3 - t_1$, $t_3 - t_2$, $t_4 - t_2$, $t_4 - t_3$, and the interferometric phase at a pixel of a particular pair (here, $t_2 \sim t_3$) is zero due to low coherence, which could be improperly estimated as non-deformation, the SBAS equation can be formulated as ($\Phi_{ifgs=} TBv = \tilde{B}v$ (4.5)),

$$\begin{pmatrix} \phi_{ifgs}^{1-2} \\ \phi_{ifgs}^{1-3} \\ \phi_{ifgs}^{2-3} \\ \phi_{ifgs}^{2-4} \\ \phi_{ifgs}^{3-4} \end{pmatrix} = \begin{pmatrix} 1 & 0 & 0 & 0 & 0 \\ 0 & 1 & 0 & 0 & 0 \\ 0 & 0 & 0 & 0 & 0 \\ 0 & 0 & 0 & 1 & 0 \\ 0 & 0 & 0 & 0 & 1 \end{pmatrix} \begin{pmatrix} t_2 - t_1 & 0 & 0 & B_\perp^{1-2} \\ t_2 - t_1 & t_3 - t_2 & 0 & B_\perp^{1-3} \\ 0 & t_3 - t_2 & 0 & B_\perp^{2-3} \\ 0 & t_3 - t_2 & t_4 - t_3 & B_\perp^{2-4} \\ 0 & 0 & t_4 - t_3 & B_\perp^{3-4} \end{pmatrix} \begin{pmatrix} v_1 \\ v_2 \\ v_3 \\ \dfrac{\triangle z}{R \cdot \sin\theta} \end{pmatrix} \tag{4.6}$$

If pixels of all interferoms have high coherence and their phase unwrapping is properly performed, *T* matrix will be same as I $(N \times N)$ identity matrix. When interferometric phase of k[th] interferogram is set to zero due to low coherence, $k \times k$ diagonal term of *T* matrix will be zero. Due to the introduction of *T* transformation matrix, changing the size of design matrix *B* is not needed for pixels of all interferograms. Another problem of $\tilde{B}$ $(N \times M)$ matrix is a rank deficiency, because critical links of InSAR networks are often missing due to low coherence of many InSAR pairs. In addition, the InSAR images might be divided to separate networks due to the baseline configuration (Berardino et al., 2002). The SVD inversion of $\tilde{B}$ matrix enables to solve Equation 4.5 and obtain the unknown v vector, but the incremental phase delay of *v* vector is set to zero by SVD, which biases the subsidence temporal behavior and

subsidence rate (López-Quiroz et al., 2009). The solution for the problem is using Tikhonov regularization (Tikhonov and Arsenin, 1977) or low-pass filtering in the time domain (Samsonov and d′Oreye, 2012). Another solution is considering the quadratic behavior of the incremental phase delay and adding constrains to design matrix $\tilde{B}$. The solution supposes that deformation increases or decreases with second order polynomials in time. Applying Gaussian filter in time to estimated incremental phase smoothes deformation with avoiding the effect by rank-deficiency and residual atmospheric error. This study added the following constraint to the inversion as proposed by previous study (López-Quiroz et al., 2009),

$$\sum_{k=1}^{m} \phi_k^{inc} = a(t_m - t_1) + b(t_m - t_1)^2 + c \tag{4.7}$$

where a, b, c terms are constants describing the quadratic behavior of incremental phase terms of v vector at time of m. After the constraint is added to Equation 4.5, the matrix system becomes $\Phi_{ifgs}^{c} = B^{c} v^{c}$

$$\begin{pmatrix} \phi_{ifgs}^{1} \\ \vdots \\ \phi_{ifgs}^{N} \\ 0 \\ \vdots \\ 0 \end{pmatrix} = \begin{pmatrix} & & & & & & & & & \\ & & & & & \left(\tilde{B}\right) & & & & \\ & & & & & & & & & \\ \gamma \cdot & & & & & & & & & \\ & & & & & & & & & \end{pmatrix} \begin{pmatrix} v_1 \\ \vdots \\ v_{M-1} \\ \frac{\triangle z}{R \cdot \sin\theta} \\ a \\ b \\ c \end{pmatrix} \tag{4.8}$$

where the weight γ is additional scaling matrix of B^{c} of dimension $(N + M - 1) \times (M + 3)$, and should be small not to affect the inversion of a major design matrix $\tilde{B}$. The inversion of $B_c^T B_c$ calculates the incremental phase delay included in v vector, and its integration corresponds to cumulative deformation phase at particular time.

4.3 Data processing

4.3.1 Characteristics of study region

Our study region is Tucson city in Arizona of southwest USA (Figure 4.1). The city's elevation ranges from 600 to 1300 meter, and most residential areas in downtown

are located between 800 m and 900 m at a relatively flat area compared to mountains in the west (Tucson mountains) and north (Santa Catalina mountains).

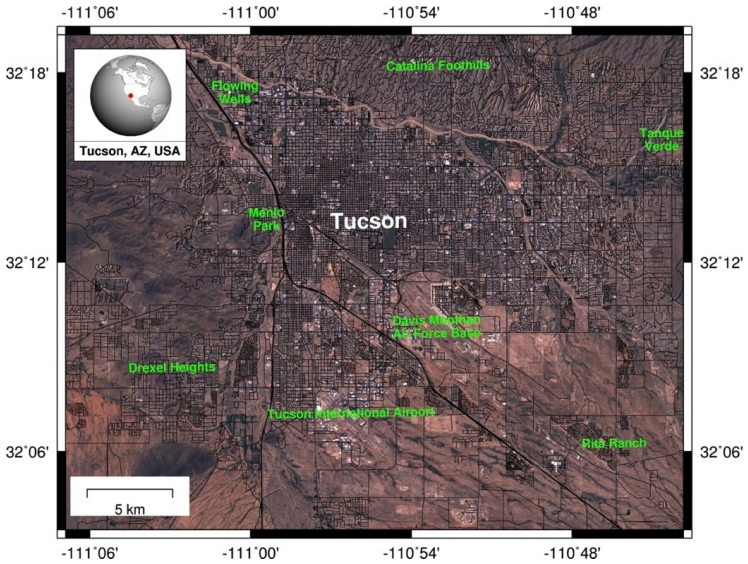

Figure 4.1. Tucson metropolitan area located in Pima county, Arizona.

The Santa Cruz River, which flowed along the west side of the Tucson, was a perennial river, but now a dry river bed for most of the year except flooding by seasonal rains. Since the Santa Cruz River became dry and the surface water had been gradually vanished, the city has been dependent on the pumping of groundwater for residential use and agricultural irrigation. Consequently, the water level measured in wells has been dramatically dropped as much as 30 meters since 1900s. The land subsidence and earth fissure occurred in Tucson and southern Arizona and damaged the roads and civilian properties, but the phenomenon is depending on the geological condition. The aquifer-compaction and land subsidence is associated with many parameters including soil composition, clay thickness, and soil consolidation. The groundwater withdrawal in dry lands does not necessarily mean ground subsidence, because regions with over-consolidated and incompressible soil, or relatively thin aggregate clay thickness are less sensitive to the variation of water table in aquifer. In areas with thick aquitards, the subsidence is often delayed after water table is decreased (Galloway and Hoffmann, 2007). As shown in Figure 4.2, the geological composition in Tucson can be grouped into three stratigraphic units (lower, middle, and upper) and stream-channel alluvium. The lower stratigraphic unit consists of conglomerate, sandstone, mudstone, and gypsiferous mudstone. The middle stratigraphic unit consists of clayey silt, mudstone, and gravel conglomerate. The upper stratigraphic unit consists of gravel, clayey silt, and thin surficial alluvial deposits (Carruth et al., 2007). Among three stratigraphic units, the upper stratigraphic unit is more subject to land subsidence by groundwater extraction and, therefore, the Tucson regions with upper stratigraphic unit has been more exposed to land subsidence. To recover the groundwater storage and stop water level declines during the last several decades, the Central Arizona Project pumped significant artificial

recharge into the aquifer. As a result, the recent groundwater withdrawal has been decreased, and the water level in many wells indicates the increase of water table (Pool, 2005; Carruth et al., 2007).

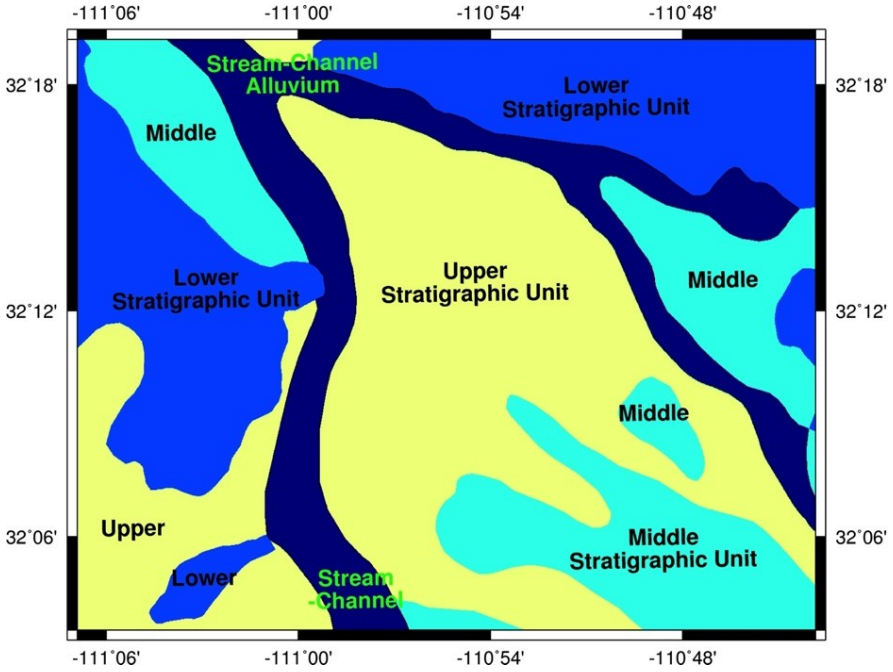

Figure 4.2. Generalized geological map in Tucson metropolitan area. The geological composition consists of upper, middle, and lower stratigraphic units. The area with upper stratigraphic unit is subject to ground deformation.

4.3.2 SBAS data processing

For this study, 17 ERS-1/2, 24 ENVISAT ASAR, and 8 ALOS PALSAR images, covering the Tucson metropolitan area (Figure 4.1), were utilized as shown in Table 4.1. ERS-1/-2 images including two ERS-1/2 tandem pairs of January, 11, 1996 ~ January, 12, 1997 and April, 25, 1996 ~ April, 26, 1996 were acquired from 1993 to 2002. ENVISAT ASAR images are obtained between 2004 and 2010. Both ERS and ENVISAT ASAR images are from the same descending track of 456, meaning a similar radar geometry, but ERS/ENVISAT InSAR pair cannot be generated due to the difference in center frequency. There is no temporal overlap of ERS and ENVISAT SAR data, causing a data gap between 2002 and 2004. The ALOS PALSAR images were acquired from ascending track, and the ALOS images covers a relatively short time period from late 2009 to 2011 in contrast to C-band sensors.

Date	Path	Center Frequency (GHz)	Direction	Incidence Angle (deg)
19930622	456	5.300	Descending	23.2711
19931109	456	5.300	Descending	23.2711
19960111	456	5.300	Descending	23.2711
19960112	456	5.300	Descending	23.2711
19960425	456	5.300	Descending	23.2711
19960426	456	5.300	Descending	23.2711
19961122	456	5.300	Descending	23.2711
19970131	456	5.300	Descending	23.2711
19970307	456	5.300	Descending	23.2711
19970829	456	5.300	Descending	23.2711
19991008	456	5.300	Descending	23.2711
19991112	456	5.300	Descending	23.2711
20000121	456	5.300	Descending	23.2711
20000714	456	5.300	Descending	23.2711
20000818	456	5.300	Descending	23.2711
20000922	456	5.300	Descending	23.2711
20020405	456	5.300	Descending	23.2711
20040130	456	5.331	Descending	22.7884
20040409	456	5.331	Descending	22.7884
20040514	456	5.331	Descending	22.7884
20040723	456	5.331	Descending	22.7884
20041105	456	5.331	Descending	22.7884
20041210	456	5.331	Descending	22.7884
20060310	456	5.331	Descending	22.7884
20060414	456	5.331	Descending	22.7884
20060623	456	5.331	Descending	22.7884
20061110	456	5.331	Descending	22.7884
20070223	456	5.331	Descending	22.7884
20070608	456	5.331	Descending	22.7884

Continued

Table 4.1. SAR images used for ERS, ENVISAT and ALOS SBAS processing.

Table 4.1. continued

Date	Path	Center Frequency (GHz)	Direction	Incidence Angle (deg)
20070712	203	1.270	Ascending	38.7249
20070817	456	5.331	Descending	22.7884
20071026	456	5.331	Descending	22.7884
20080112	203	1.270	Ascending	38.7249
20080208	456	5.331	Descending	22.7884
20080413	203	1.270	Ascending	38.7249
20080523	456	5.331	Descending	22.7884
20080905	456	5.331	Descending	22.7884
20090403	456	5.331	Descending	22.7884
20090717	456	5.331	Descending	22.7884
20090925	456	5.331	Descending	22.7884
20091017	203	1.270	Ascending	38.7249
20091202	203	1.270	Ascending	38.7249
20100117	203	1.270	Ascending	38.7249
20100212	456	5.331	Descending	22.7884
20100419	203	1.270	Ascending	38.7249
20100423	456	5.331	Descending	22.7884
20100528	456	5.331	Descending	22.7884
20100604	203	1.270	Ascending	38.7249
20100910	456	5.331	Descending	22.7884
20101205	203	1.270	Ascending	38.7249
20110120	203	1.270	Ascending	38.7249
20110307	203	1.270	Ascending	38.7249

For SBAS processing, ERS and ENVISAT InSAR pairs with a perpendicular baseline smaller than 500 meter are generated. Furthermore, InSAR pairs with a good coherence should be selected for reliable DInSAR processing including phase unwrapping. Figure 4.3(a) shows temporal baselines and dates of C-Band InSAR pairs of 29 ERS (red lines) and 134 ENVISAT (blue lines) interferograms with a small perpendicular baseline and good coherence. 28 ALOS InSAR pairs (Figure 4.3(b)) are created from all 8 SAR images, because L-band InSAR pairs in Tucson are less influenced by temporal and spatial decorrelation related to a large perpendicular baseline and a long time interval.

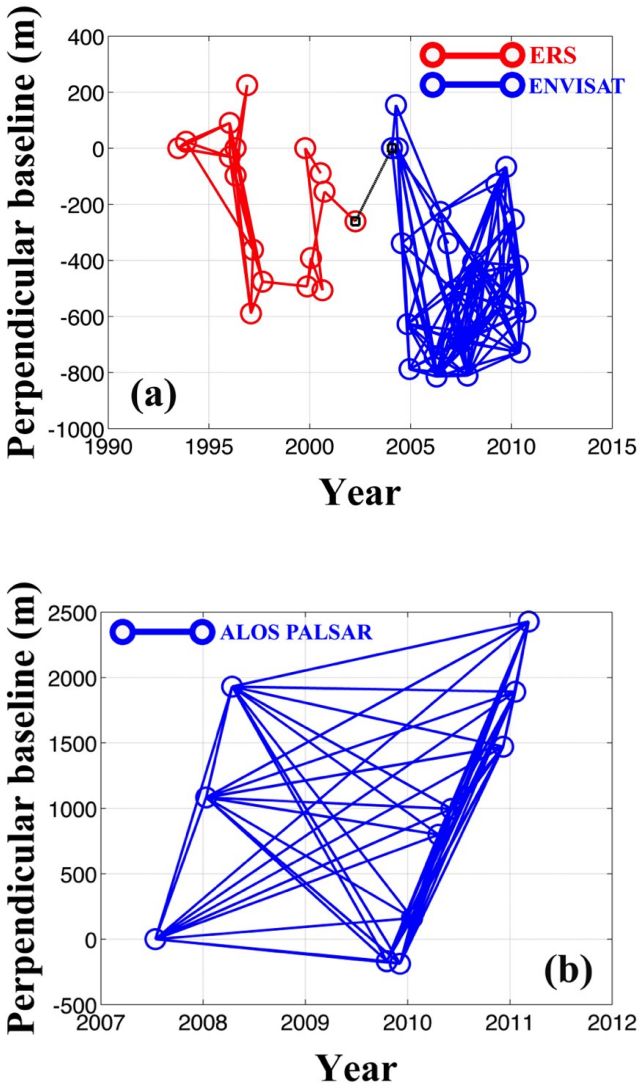

Figure 4.3. Diagram of a perpendicular baseline and InSAR pairs ((a) ERS and ENVISAT InSAR pairs; red circles and lines are ERS pairs, and blue circles and lines are ENVISAT pairs. Dotted black line represents simulated temporary InSAR pair to fill up data gap. (b) ALOS PALSAR InSAR pairs).

1-arcsec national elevation dataset (NED) is used to remove topographic contributions in DInSAR processing of ERS, ENVISAT and ALOS pairs. The precise orbit information of ERS and ENVISAT is provided by Delft institute for earth-oriented space research (DEOS). But some InSAR pairs of ERS, ENVISAT, and ALOS are deteriorated by orbital fringes, which are then removed by 2nd order polynomial estimation in range and azimuth direction. Some examples of differential interferograms from ERS, ENVISAT, ALOS are shown in Figure 4.4, 4.5, and 4.6. From the figures, one can recognize that there are only few fringes in ALOS InSAR images (Figure 4.6), as the

L-band sensor (wavelength of ~24 cm) is less sensitive to slow-developing deformation by groundwater extraction in Tucson. Also, it is recognizable that C-band interferograms of Figure 4.4 and 4.5 shows obvious signatures by ground subsidence in downtown of Tucson, but most interferograms are affected by atmospheric artifacts, particularly turbulent contributions that do not correlate in time. For example, Figure 4.5(a) spans a short period, but many areas in the interferogram contain atmospheric artifacts. The co-registration of all InSAR pairs is required for SBAS processing, and phase unwrapping after smoothing interferograms is applied by minimum cost flow (MCF) algorithm.

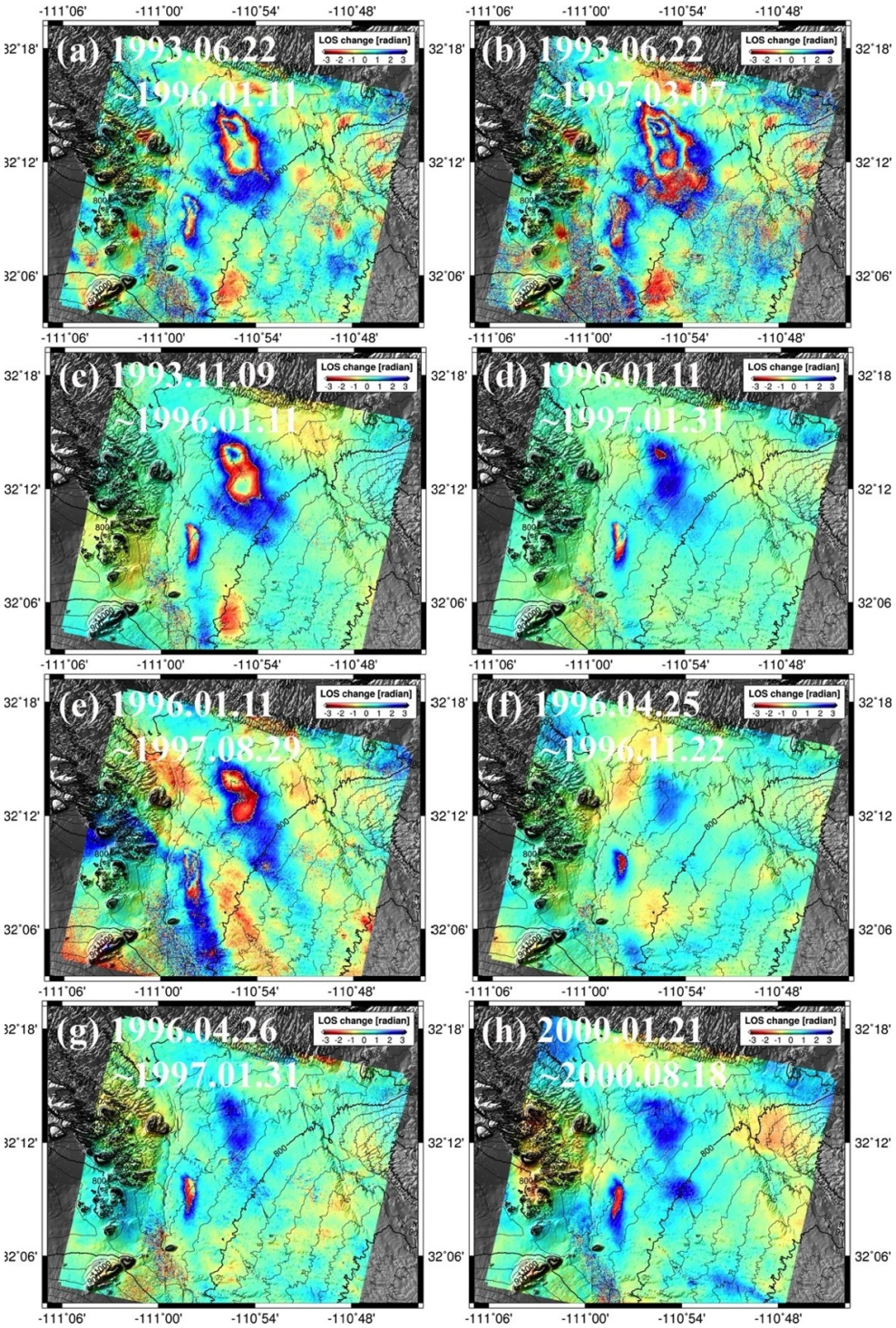

Figure 4.4. ERS-1/2 differential interferogram from (a) 1993.06.22~1996.01.11, (b) 1993.06.22~1997.03.07, (c) 1993.11.09~1996.01.12, (d) 1996.01.11~1997.01.31, (e) 1996.01.11~1997.08.29, (f) 1996.04.25~1996.11.22, (g) 1996.04.26~1997.01.31, and (h) 2000.01.21~2000.08.18.

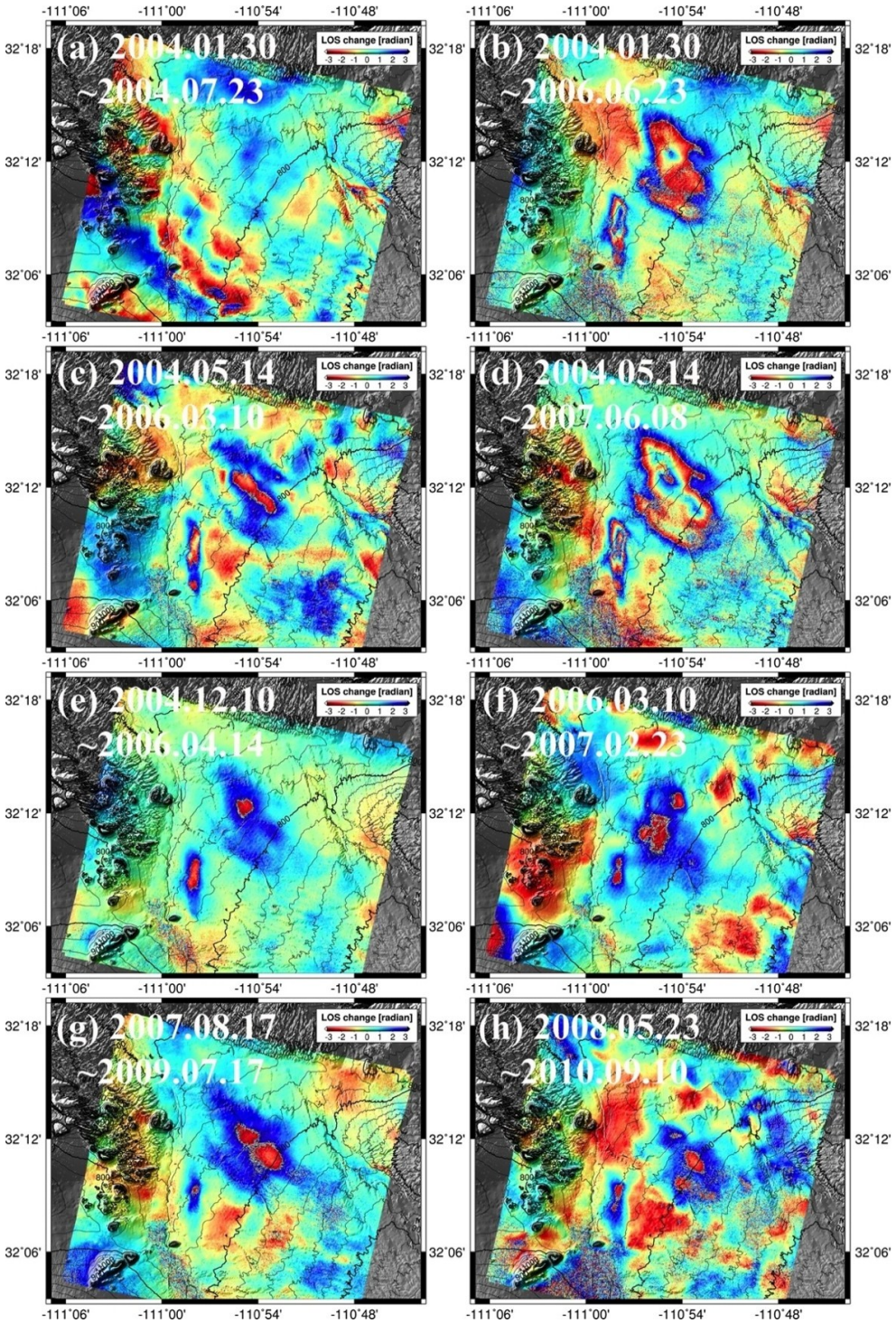

Figure 4.5. ENVISAT differential interferogram from (a) 2004.01.30~2004.07.23, (b) 2004.01.30.2006.06.23, (c) 2004.05.14~2006.03.10, (d) 2004.05.14~2007.06.08, (e) 2004.12.10~2006.04.14, (f) 2006.03.10~2007.02.23, (g) 2007.08.17~2009.07.17, and (h) 2008.05.23~2010.09.10.

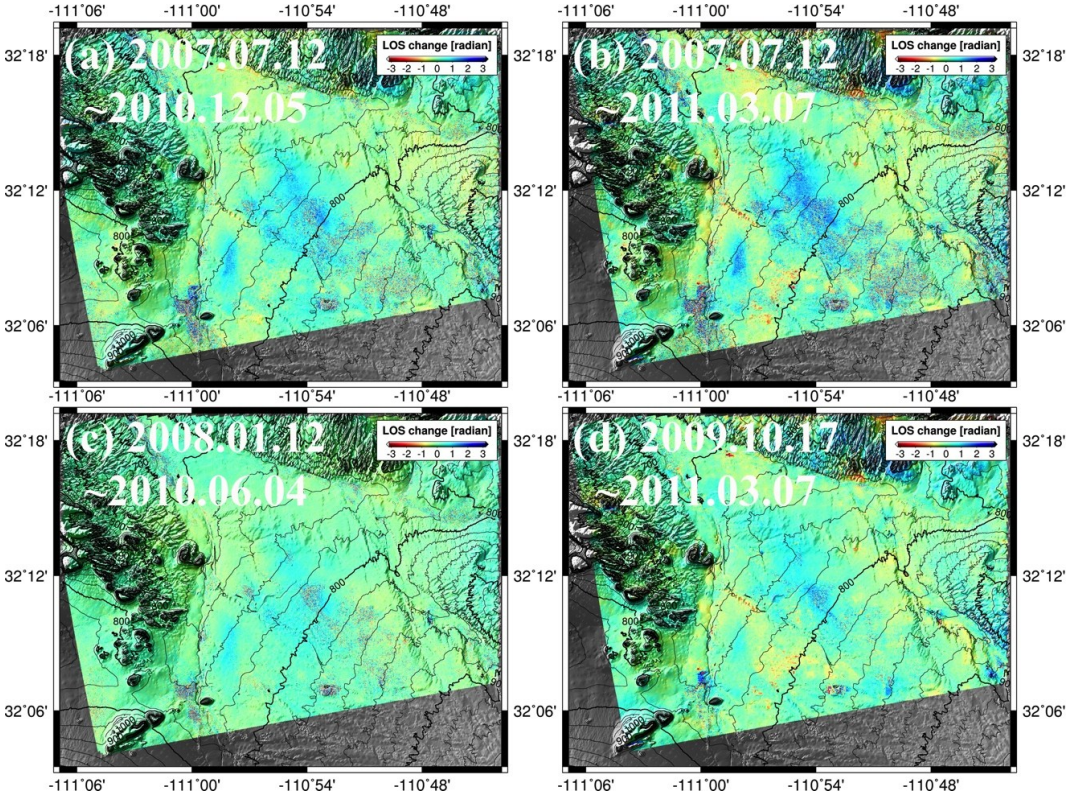

Figure 4.6. ALOS PALSAR differential interferogram from (a) 2007.07.12~2010.12.05, (b) 2007.07.12~2011.03.07, (c) 2008.01.12~2010.06.04, and (d) 2009.10.17~2011.03.07.

One problem in integrating ERS and ENVISAT to SBAS algorithm in our dataset is a data gap between two groups of InSAR pairs in Figure 4.3(a), and the gap causes a rank deficiency in SBAS processing owing to missing a critical link. To solve the problem, the linear deformation rate is estimated from each ERS and ENVISAT SBAS processing, and simulated temporary interferogram between a gap is generated from averaging two linear deformation rates:

$$\frac{1}{2}\left(\left(\frac{\sum \phi_k^{inc}}{\sum t_k}\right)_{ERS}+\left(\frac{\sum \phi_k^{inc}}{\sum t_k}\right)_{ENVISAT}\right)\cdot(gap\,days/yr) \quad (4.9)$$

The temporary interferogram is expressed as a dotted black line in Figure 4.3 (a). After SBAS processing from ERS/ENVISAT and ALOS, all outputs are filtered by Gaussian filter in time domain to suppress still-remaining atmospheric phase. The selected SBAS InSAR-derived deformation maps are shown in Figure 4.7, 4.8, and 4.9. Forty time-series of vertical displacements corresponding to each ERS and ENVISAT acquisition date are generated like Figure 4.7, and the number of C-band time-series is equal to M (number of SLC data)-1. Furthermore, seven time-series of vertical displacement corresponding to ALOS acquisition date is created in Figure 4.8. In Figure

4.9, a linear deformation rate is estimated from C-band and L-band SBAS processing. The C-band deformation rate is calculated from 1993 to 2010, and the L-band deformation rate is from late 2009 to 2011.

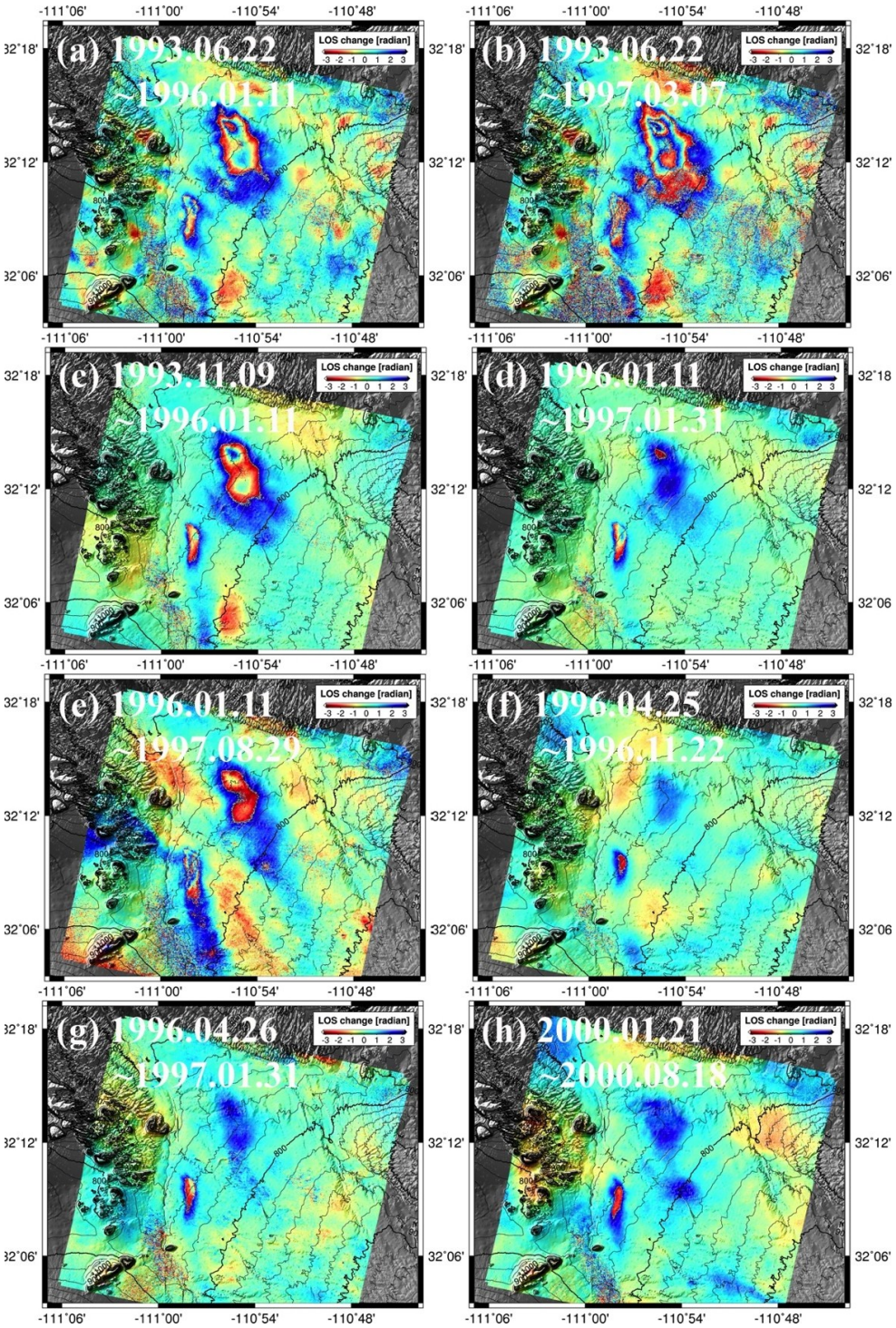

Figure 4.7. Time-series of vertical deformation from ERS/ENVISAT SBAS InSAR processing of (a) 1993.11.09, (b) 1996.11.22, (c) 1999.10.08, (d) 2000.08.18, (e) 2004.12.10, (f) 2007.10.26, and (g) 2008.09.05, and (h) 2010.09.10.

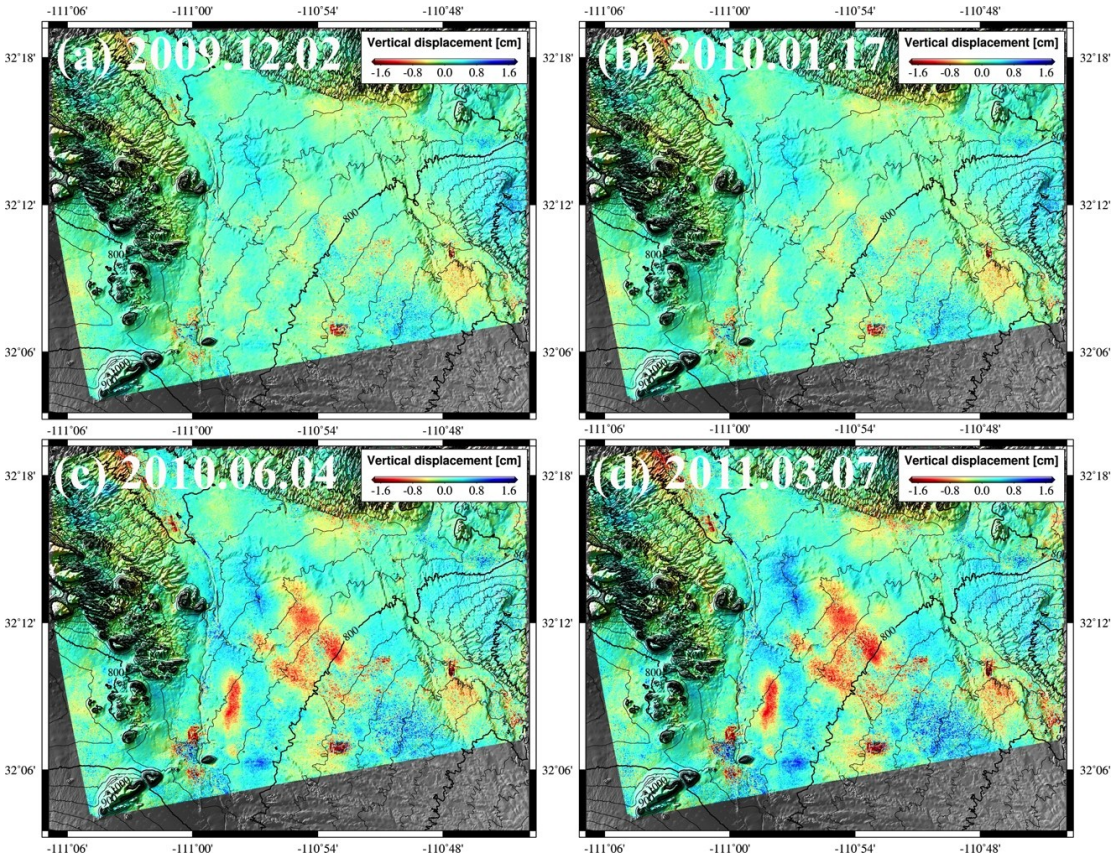

Figure 4.8. Time-series of vertical deformation from ALOS SBAS InSAR processing of (a) 2009.12.02, (b) 2010.01.17, and (c) 2010.06.04, and (d) 2011.03.07.

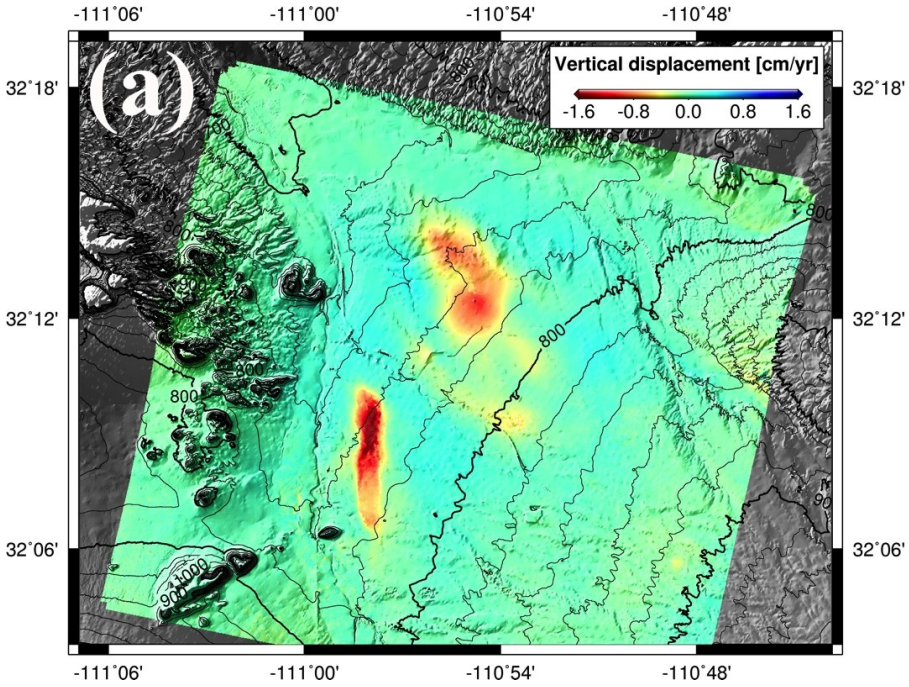

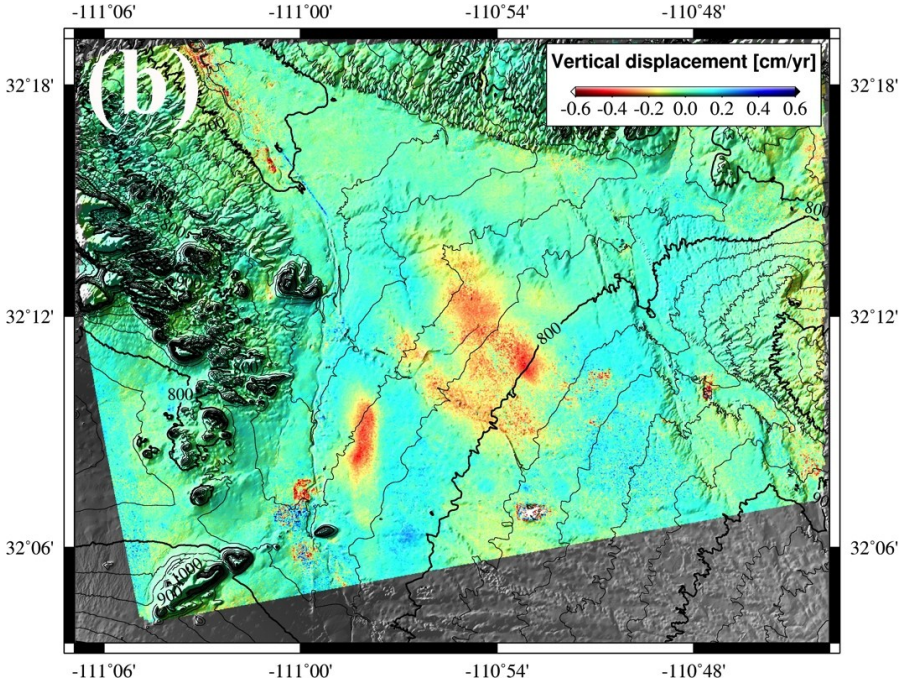

Figure 4.9. Linear vertical deformation rate (cm/yr) estimated from (a) ERS/ENVISAT and (b) ALOS SBAS processing. The red-colored region represents ground subsidence due to groundwater extraction.

4.4 Results

The water level in the subsurface has been monitored at wells densely located in Tucson (USGS Water Resources of Arizona). Because many wells were installed before 1980s, a long-term monitoring related to groundwater extraction is possible. Figure 4.10 (a), (b), and (c) shows 10-year interval measurement of groundwater level from 1980s to 2010s. The groundwater level from 1980s to 1990s in Figure 4.10 (a) was dramatically dropped as much as 25 meters, and the region of groundwater withdrawal was concentrated on a major residential area in Tucson. The amount of groundwater extraction was gradually reduced during 1990s in Figure 4.10(b), and the water level during 2000s in Figure 4.10(c) was recovered into a slight increase as a result of an artificial recharge into the aquifer-system. For 30 years between 1980s and 2010s in Figure 4.10(d), most of water decline occurred during the first 10 years: the maximum water decline exceeded 25 meters, and most parts except the southern area had water level decrease of approximately 12 meters.

The annual GPS survey campaign was conducted in multiple sites (red crosses in Figure 4.11(a)), and the extensometers (blue crosses) measured the compaction of aquifer-system. The GPS-survey technique estimated primarily the vertical deformation from measured ellipsoid heights, and the increased compaction measured by extensometers implies downward land surface motion between land surface and the depth at which the bottom of the extensometer is anchored (Carruth et al., 2007). The extensometer data was acquired from USGS monitoring sites, and the annual GPS survey data is from previous USGS report (Pool et al., 2007; Carruth et al., 2007). The green arrow in Figure 4.11 (b) describes the compaction at the extensometer monitoring sites, and the length of arrows describes the amount of compaction from October, 2010 to September, 2012. The contour and colored image in Figure 4.11(b) delineates the interpolated groundwater level change from 1980s to 2010s, and red and yellow regions describe the groundwater-withdrawn areas. Although there is a small number of extensometers, the region affected by large groundwater extraction indicate large compaction possibly leading to ground subsidence. The vertical deformation measured from annual GPS survey varies among station locations, and the maximum subsidence between 1998 and 2005 reached 9.14 cm (Figure 4.11(c)).

From the results of ERS/ENVISAT SBAS processing in Figure 4.7, a noticeable land subsidence occurred in the center of Tucson city, around Davis Monthan Air Force Base, and near the Tucson international airport. The deformation maps show the cumulative land surface motion with respect to the acquisition date of the first SAR image (June 22, 1993). The vertical deformation in the center of Tucson city is about 14 ~ 20 cm during 17-year period from 1993 to 2010, and the maximum subsidence of 24 cm occurred in the northern area of Tucson international airport. Moreover, as shown in Figure 4.8, ALOS SBAS InSAR processing has allowed us to obtain time-series of vertical deformation from the first ALOS acquisition date (October 17, 2009). The pattern of subsidence from ALOS InSAR pairs is similar to that from ERS/ENVISAR processing, and the subsidence is about 1.6 cm in the center of Tucson city and near the international airport between October 2009 and March 2011. The linear deformation rates are calculated from two SBAS InSAR processing, ERS/ENVISAT products in Figure

4.9(a) indicate the maximum subsidence rate of 1.6 cm/year during 17 years, and ALOS SBAS processed results in Figure 4.9(b) delineate slowed maximum subsidence rate of 0.6 cm/year between 2009 and 2011.

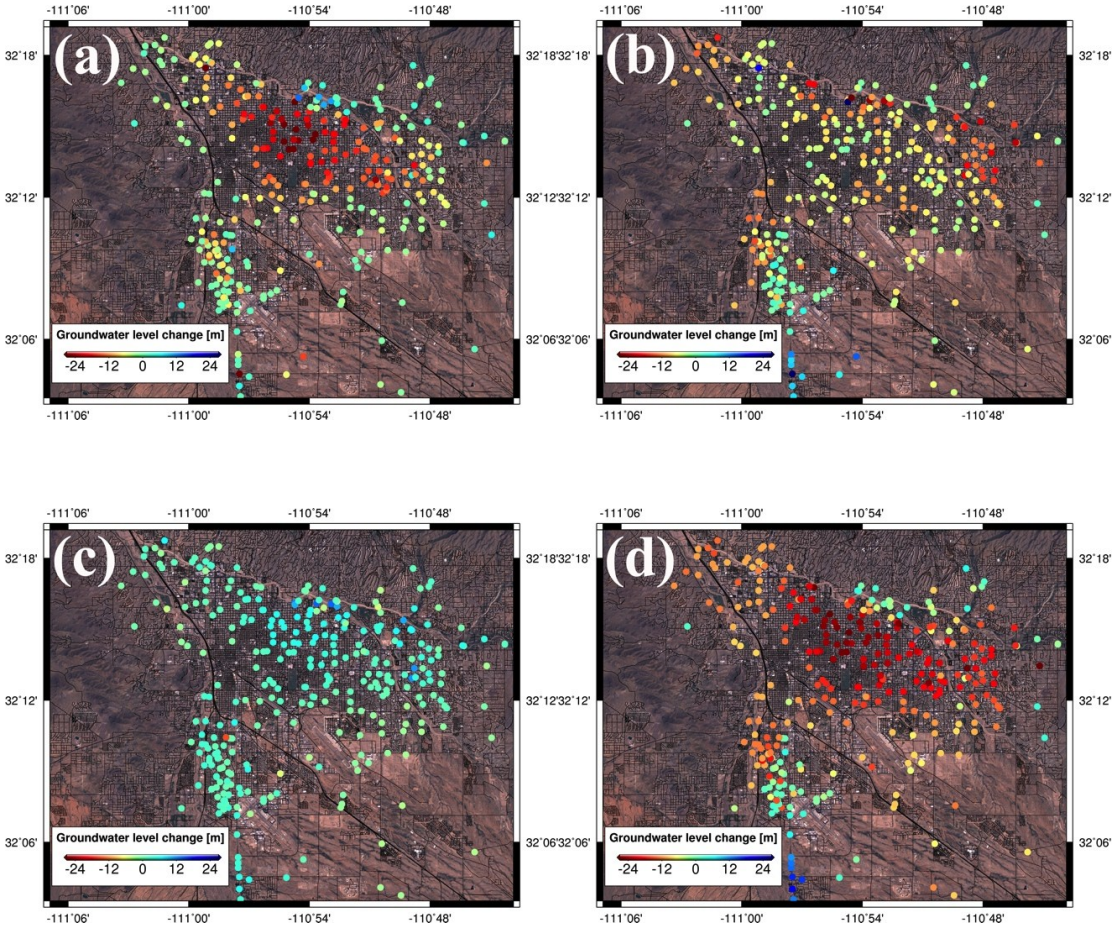

Figure 4.10. 10-year interval groundwater level changes measured at wells of (a) 1980s~1990s, (b) 1990s~2000s, and (c) 2000s~2010s, and 30-year water level changes of (d) 1980s~2010s. The red and blue colored dots mean the increase and decrease of water level at wells.

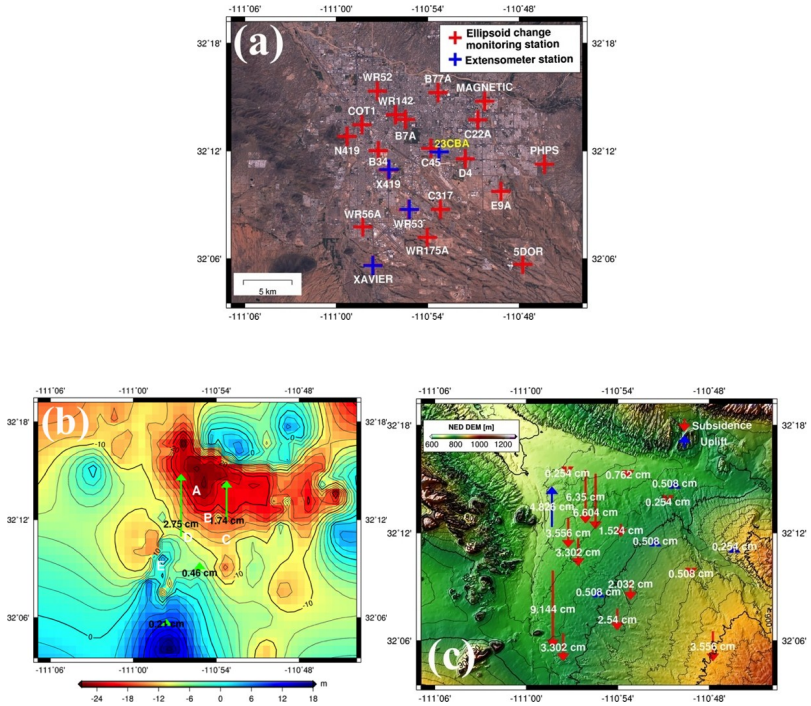

Figure 4.11. (a) Land subsidence monitoring and extensometer stations installed in Tucson, (b) Interpolated water level change from 1980s to 2010s (background), and each green arrows represent the compaction measured by extensometers from October, 2010 to September, 2012, and (c) Ellipsoid height changes measured in monitoring stations from 1998 to 2005; red and blue arrows represent subsidence and uplift at the sites, and the length of arrows expresses the amount of the ellipsoid height change.

When the compaction from extensometers (blue dots) and time-series of subsidence (red circles) from SBAS processing are compared in Figure 4.12, the results of land subsidence from 2006 to 2011 have general agreement at stations of WR53, X419, XAVIER, and 23CBA. The products of ALOS SBAS processing (red circles in lower panels of Figure 4.12 (a), (b), (c), and (d)) at WR53 and X419 show a similar pattern, though there is difference between estimated deformation and compaction at XAVIER and 23CBA. When one focuses on the ERS/ENVISAT SBAS InSAR-derived deformation (red circles in upper panels of Figure 4.12 (a), (b), (c), and (d)) in time-series, the subsidence in WR53 is about 0.8 cm during compaction of 0.5 cm, and the vertical surface motion and compaction has a similar amount. Because of a short time period and slowly growing subsidence in all monitoring sites, it is hard to determine the accuracy of SBAS InSAR processing. Yet, when considering the characteristics of the extensometers that cannot measure the subsurface change below the bottom of the device, the comparison is within a category of general agreement. In Figure 4.13, the vertical displacements from ERS/ENVISAT and ALOS SBAS InSAR processing and ellipsoid height change since 1998 (Pool et al., 2007) are compared. The accuracy of vertical measurement using GPS technology is assumed to be 2.032 cm (Carruth et al., 2007). In most monitoring stations, the results from GPS survey and SBAS InSAR shows a similar pattern over time, and the SBAS-derived deformations are within the uncertainties of GPS measurements. Also, though ALOS pairs span only a short time period, the results from both ERS/ENVISAT and ALOS SBAS InSAR processing are in a good agreement. In sites of B7A, WR56A, WR142, X419, and C45, both of GPS and SBAS InSAR-derived deformation describes the ground subsidence due to the groundwater extraction. However, in some places of MAGNETIC, WR53, and WR52, the ground is in uplift and it could be attributed to rebounding of ground surface after groundwater recovery. The temporal groundwater elevation measured at wells is also compared with ERS/ENVISAT SBAS-processed vertical displacement in Figure 4.14. The pattern of groundwater elevation change is shown in most wells of Tucson. The groundwater level was declining until 2003, and an artificial recharge and reduced consumption of groundwater brought out the recent increase of water table. At station WR56A, the ground subsidence is about 15 cm during observation period. In addition, the surface is still subsiding after 2003, and it implies that the subsidence could be affected by delayed compaction and inelastic behavior, while the deformation is not recovered, but permanent. In WR52, the land surface with increased groundwater level is in uplift. It indicates that the displacement in the location is elastic, while the increase of groundwater causes a recovery of subsurface.

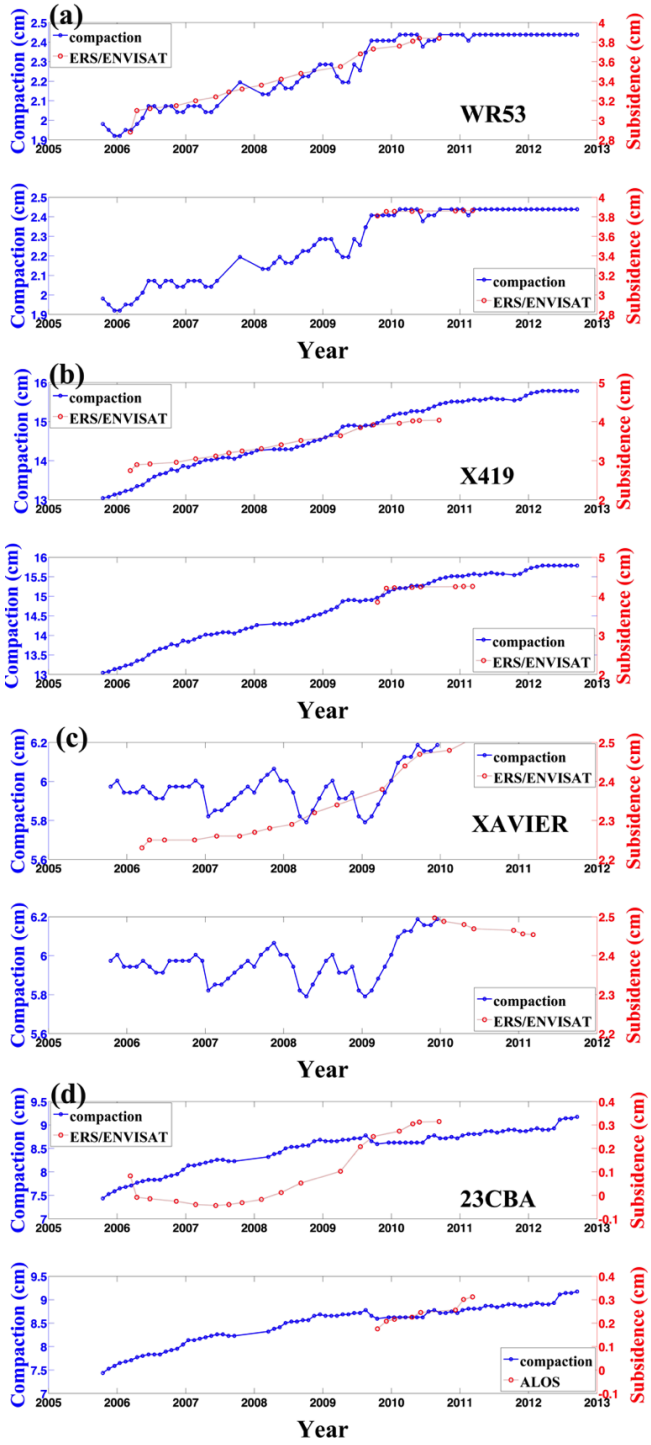

Figure 4.12. Monthly compaction (blue dots) from October, 2005 to September 2012, and subsidence (red circles) estimated from ERS/ENVISAT and ALOS SBAS processing at monitoring stations of (a) WR53, (b) X419, (c) XAVIER, and (d) 23CBA.

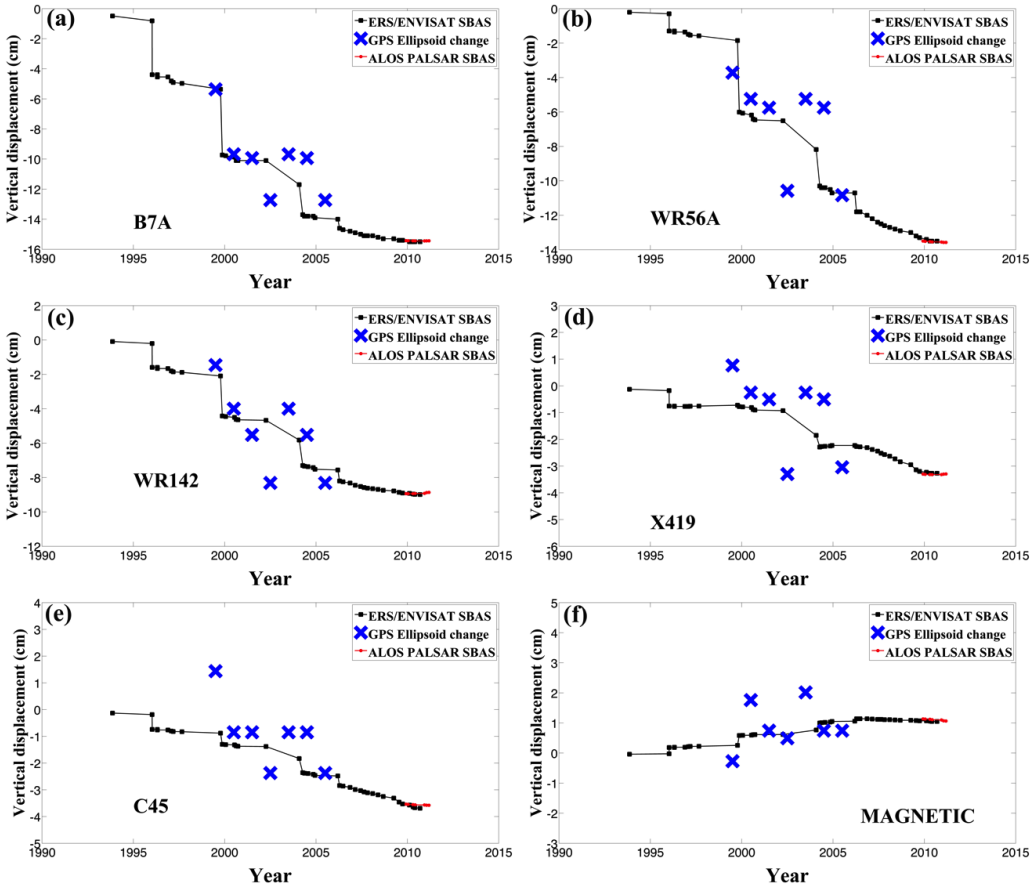

Figure 4.13. Vertical displacements from ERS/ENVISAT (black squares) and ALOS (red dots) SBAS processing, and GPS ellipsoid height change (blue circles) from 1999 to 2005 at stations of (a) B7A, (b) WR56A, (c) WR142, (d) X419, (e) C45, (f) MAGNETIC, (g) WR53, and (h) WR52.

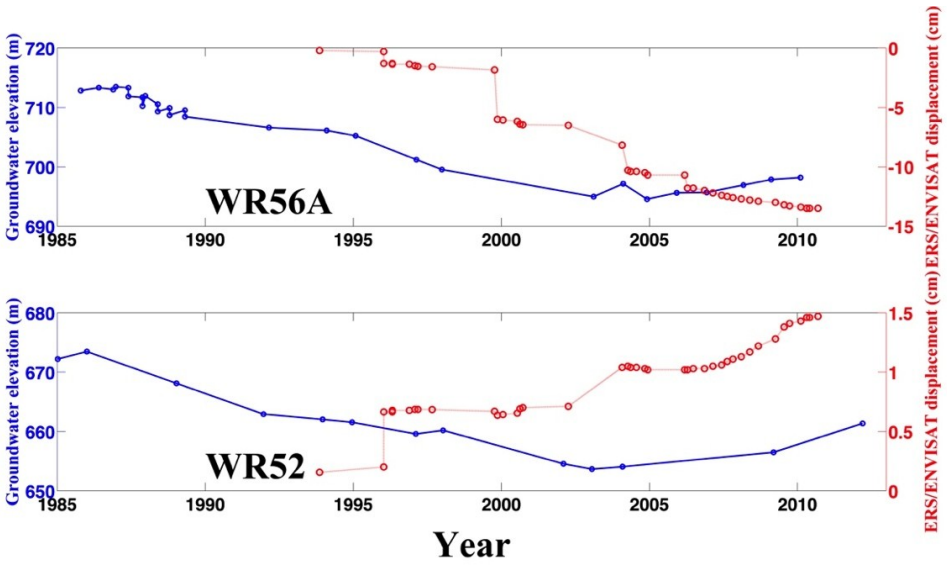

Figure 4.14. Time-series vertical deformation (red circles and lines) from ERS/ENVISAT SBAS processing and groundwater elevation (blue dots and lines) measured in WR56A and WR52.

Figure 4.15(a) and (b) represents the vertical deformation estimated from ERS/ENVISAT SBAS InSAR processing from 1993 to 2010 in three dimension and plain views. The contour and vertically exaggerated deformation map delineates several major subsidized region affected by groundwater extraction. A, B, and D regions are near the center of Tucson city, C is close to Davis Monthan Air Force Base, and E region is around the northern part in Tucson International Airport. A and B regions have the subsidence of about 14 cm, and C and D areas are affected by 4 cm subsidence. E regions have the maximum subsidence exceeding 20 cm during 17-year span. When comparing the water level change map in Figure 4.11(b) and the subsidence map (Figure 4.16 (b)), A and B regions are in the areas of maximum water level changes since 1980s. C and D areas are overlapped with a region of relatively small water level change. Because the change of groundwater and surface motion is correlated, the result explains that the groundwater level change caused the ground deformation in A, B, C, and D. On the other hand, other areas with large water level change do not have a significant subsidence. The reasonable assumption is that clay thickness is not sufficient for sensitive response to the change of aquifer-system in the subsurface, or a soil layer is over-consolidated and incompressible and the surface is very stabilized. E region with maximum subsidence is another exception, because the groundwater level change and subsidence is not highly correlated. As shown in Figure 4.10 (d) and 4.11 (b), the E region is in the mix of increase and decrease of groundwater level, and the change of aquifer-system may not be a major cause of large subsidence. Possibly, the human construction of roads, buildings, and airport can cause a large vertical deformation in E region. However, currently, it is not clear which factors mostly affected the vertical deformation in E area.

One of great advantages of SBAS InSAR processing is that it could estimate vertical deformation between two particular acquisition dates. The difference of cumulative deformations of two particular dates can delineate temporal evolution of subsidized areas in Tucson. Images in Figure 4.16 are generated from the difference of deformation maps (Figure 4.7) with about three-year interval, estimated from ERS/ENVISAT SBAS InSAR processing. Red-colored regions in Figure 4.16 mean ground subsidence, and dark red color is approximated as maximum subsidence. Between 1996 and 1999, A, B, and E region shows maximum subsidence exceeding 1.6 cm. During the span of 1999 and 2002, the maximum subsidence (dark red) of A, B, and E embraces the largest area in Tucson. In Figure 4.16(e) between 2004 and 2007, the subsidence rate of A and B is slowed down, but the C region has enlarged subsidence area since 1999. The recent observation in Figure 4.16(f) indicates a slowing subsidence in most regions of Tucson. The subsidence in A region is almost disappeared, and B region shows only a small subsidence less than 1 cm. The C region near Davis Monthan Air Force Base shows still growing subsidized region from 1999 to 2010. The subsidence area in E region between 2007 and 2010 is much smaller than the areas during other periods. The Figure 4.16(f) is well fitted to the result from ALOS SBAS InSAR processing in Figure 4.9(b), characterizing a major subsidence in B, C, and E region. The whole images in Figure 4.16 represent that the subsidence is gradually slowing down due to the recharge of groundwater.

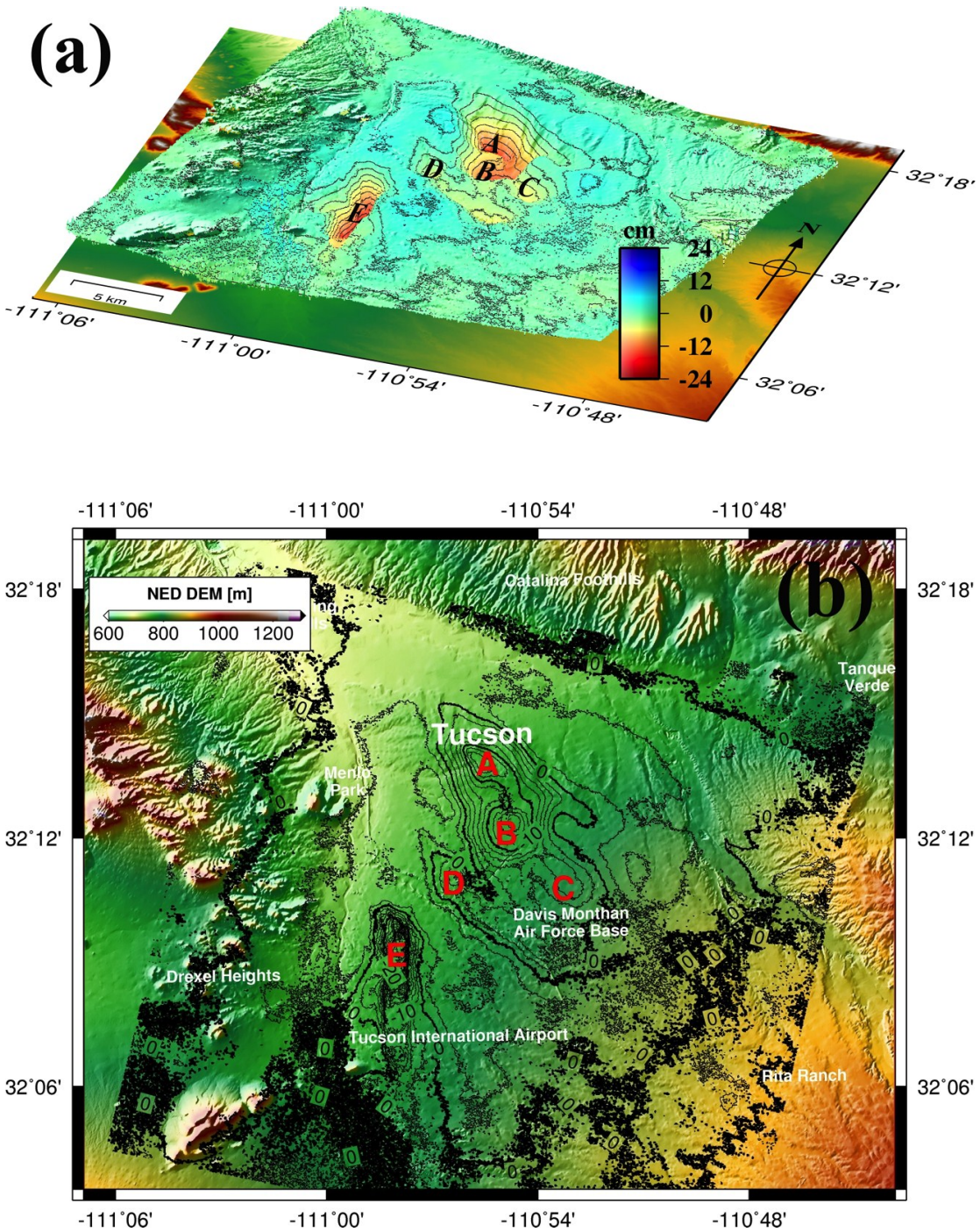

Figure 4.15. (a) Three-dimensional view of vertical deformation from 1993 to 2010. (The scale is exaggerated in vertical dimension) (b) Contour in a plain view of vertical deformation during 17-year span (A, B, C, D, and E regions are mostly affected by ground subsidence).

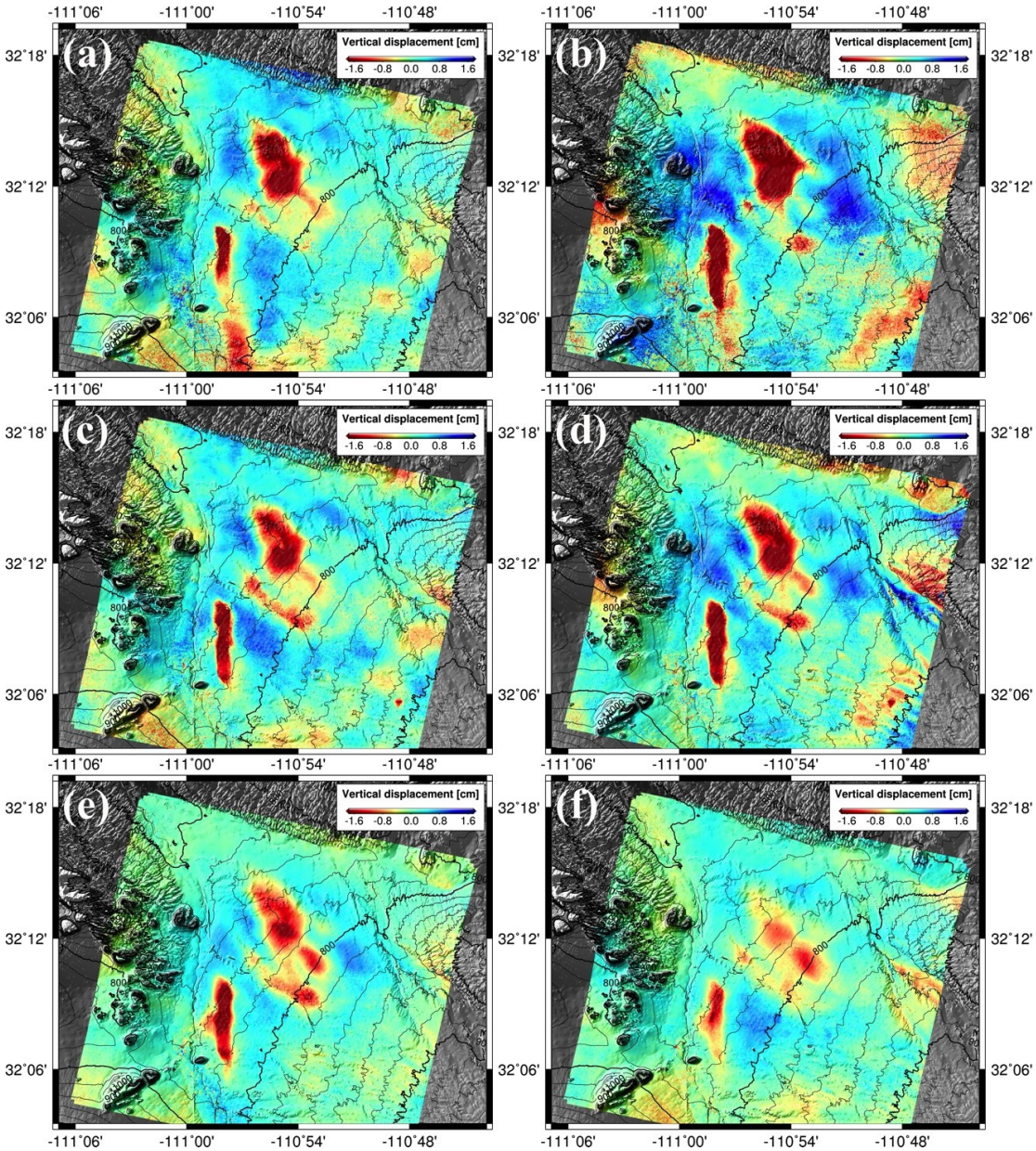

Figure 4.16. Three-year interval vertical deformation of (a) 1993.11.09 ~ 1996.11.22, (b) 1996.1122 ~ 1999. 11. 12, (c) 1999.11.12 ~ 2002.04.05, (d) 2002.04.05 ~ 2004.12.10, (e) 2004.12.10 ~ 2007.10.26, and (f) 2007.10.26 ~ 2010.09.10.

4.5 Conclusion

Since late 1800s, the Tucson in the southern Arizona has been developed for human residence and agriculture. After the surface water from a nearby river of the Santa Cruz River gradually disappeared, the region was lack of drinking water for urban development and planting water for agricultural irrigation. Therefore, the water supply in Tucson has been heavily dependent on the use of groundwater for 100 years, by pumping the groundwater into the water distribution of residential areas. The massive consumption of groundwater resources caused the visible ground subsidence and earth fissures in many Tucson areas. The groundwater level has been monitored by gauges installed in many wells, a few extensometers operated by USGS measure the compaction of aquifer-system, and the absolute and relative gravity in multiple sites was measured to estimate the storage change and groundwater budget in the subsurface (Pool et al., 2007). The InSAR technology has a great advantage of detecting the ground deformation over large areas with high accuracy and spatial resolution. Particularly the SBAS InSAR processing can capture the temporal evolution of deformation for a long time period while suppressing atmospheric artifacts. The rank deficiency is an obstacle for better reliable SBAS InSAR processing, and this study used the constraint related to quadratic behavior of the incremental phase delay to solve the problem of rank deficiency, based on the assumption that the land surface increase or decrease with first or second-order polynomials in time span.

Our multi-sensor SBAS InSAR processing delineates a long-term development of the vertical deformation from 1993 to 2011, though ALOS InSAR pairs cover a relatively short time period between late 2009 and 2011 and most analysis is focused on products from ERS/ENVISAT SBAS processing. The linear subsidence rate from C-band InSAR pairs was about 1.6 cm per year in the center of Tucson city and near Tucson International Airport, and the rate from L-band InSAR pairs indicate a slowing-down subsidence of about 0.5 cm per year after 2007. Although there is no a "real" ground-truth reference in our interest area, the compaction from extensometer shows a similar pattern with land subsidence estimated from SBAS processing and the annual GPS survey is in a good agreement with our estimated subsidence. The 3-year interval maps of vertical deformation reveal the areas of subsidence. The recent subsidence in Tucson is slowing down, and the subsidence is about to be ceased as estimated from the results between 2007 and 2010. The halting subsidence is attributed to an intense effort to conserve groundwater, because Tucson is recharging groundwater supplies by running part of its share of Central Arizona Project (CAP) water into various open portions of local rivers to seep into their aquifer (Pool et al., 2007). Our study has demonstrated that the SBAS InSAR processing is valuable for estimating slow subsidence caused by spatio-temporal responses of aquifer system. When dense temporal SAR observations are available, the integration of multi-band SAR data with X-, C-, and L-band is possible for measuring small ground deformation related to aquifer-system compaction and our study can be applied to other regions.

CHAPTER 5: Conclusion and Future Study

We live in the world flooded by much data and information. Understanding natural phenomena requires wisely choosing and analyzing necessary data. However, utilizing a single type of data restricts our knowledge and often face problems caused by data availability. Therefore, the fusion and integration of multiple sensors is a major trend in various scientific fields. The radar technology, which has all-weather and day-or-night capability, has been essential for many applications of military (surveillance and targeting), urban and agriculture management (land classification), natural resource management (forest mapping and change detection), and natural hazard monitoring (earthquake and volcanism). Particularly, SAR has provided high-resolution imagery acquired from airborne and spaceborne sensors. The SAR backscatter processed from SAR raw signal characterizes the roughness, slope, dielectric constant, and soil moisture of ground elements, and the phase components of SAR images are related to a range between a satellite and a ground target. For wetland applications, the SAR backscatter has been frequently used for discriminating vegetation type, the salinity of marshes, and vegetation density, and InSAR technology exploiting phase components has been useful for detecting relative water level changes inside the wetlands. In the arid areas, ground subsidence caused by groundwater depletion has been successfully detected by InSAR technology, while measuring the line-of-sight change from a satellite to a ground element. However, InSAR technology for wetland studies cannot measure the absolute water level change inside the wetlands, because phase differences between nearby pixel values of interferograms represent the relative movement of water surface between two particular dates. Therefore, additional data providing the reference datum are required for estimating absolute water level changes. Also, the conventional InSAR technology does not generate time-series displacement maps, which are important for a short- and long-term monitoring of ground displacement in arid areas.

First of all, this study focused on estimating absolute water level changes in the swamp forest of the Louisiana and the freshwater marsh of the Everglades. Two methods to provide the reference datum of water level changes were used. The first method was to utilize the data from radar altimetry, which gathers the absolute water level changes with temporal interval between acquisitions. The integration of radar altimetry and InSAR results enables one to estimate the absolute water level changes in the swamp forest. The map of absolute water level changes has high resolution and accuracy. However, the track of radar altimetry does not always cross the region of interest over the wetlands. In the Everglades, the radar altimetry does not acquire much data from the freshwater marsh, particularly water conservation area. In this case, an alternative method is required, and SAR backscatter can be useful for providing reliable information on the reference datum of absolute water level changes. The water level in the freshwater marsh of the Everglades has an inverse relationship with SAR backscatter, meaning that increased water level reduces the SAR backscatter. The SAR backscatter in highly correlated places was utilized as estimating the reference datum of water level changes.

The combination of SAR backscatter and InSAR results could generate the map of absolute water level changes in the freshwater marsh, and the integration evaluated at gages had high resolution of approximately 30 or 90 meters and high accuracy with RMSE less than 10 centimeters.

Secondly, this study estimated ground subsidence in Tucson, Arizona, and the ground displacement was caused by groundwater depletion. Although the conventional InSAR technology fails to fulfill time-series monitoring, SBAS InSAR technology has the capability to detect temporal development of ground deformation. The original SBAS InSAR processing suppresses turbulent mixing of multiple InSAR interferograms, which appears random in time and space, but the SBAS processing should be corrected for avoiding rank deficiency that causes the error in estimating ground displacement. The refined SBAS InSAR processing used the constraints considering the quadratic behavior of incremental phases, and it could avoid rank deficiency with additional filtering. The SBAS-derived displacement, mostly processed from C-band InSAR pairs of ERS and ENVISAT, showed that the ground subsided as much as 20 centimeters during 17 year span, and the ground subsidence in Tucson has slowed down due to the artificial recharge into the subsurface.

The SAR/InSAR and newly developed SBAS InSAR processing was a powerful tool for understanding the natural process in the wetlands and monitoring ground subsidence in the arid areas. However, SAR backscatter is not easily defined by a single parameter, but it is needed to analyze the backscatter coefficient with other parameters including biomass and density. Specially, exploring C-band SAR backscatter is more complicated, and detailed modeling of radar scattering on and beneath a canopy is necessary. Also, full polarimetric SAR data can be used for the modeling and Polarimetric InSAR (PolInSAR) technology enables one to estimate vegetation height and unravel the complex nature of scattering. Even when we utilize a single polarized SAR data, a long history of SAR backscatter can reduce the noise in the SAR scenes and enhances newly developed method to estimate water level changes in the wetlands. In Tucson, the SBAS InSAR processing was very feasible, but even refined SBAS InSAR processing has difficulty with detecting ground subsidence in low coherence areas, such as mountains or coastal region. As a future study, the PSInSAR and SBAS InSAR should be improved for suppressing low coherence and analyzing phases from consistent scatterers .

Bibliography

Alsdorf, D., Melack, J., Dunne, T., Mertes, L., Hess, L., & Smith, L. (2000). Interferometric radar measurements of water level changes on the Amazon floodplain. *Nature*, 404, 174-177.

Alsdorf, D., Smith, L., & Melack, J. (2001). Amazon floodplain water level changes measured with interferometric SIR-C radar. *IEEE Transactions on Geoscience and Remote Sensing*, 39, 423-431.

Amelung, F., Galloway, D. L., Bell, J. W., Zebker, H. (1999). Sensing the ups and downs of Las Vegas: InSAR reveals structural control of land subsidence and aquifer-system deformation. *Geology*, 27 (6), 483–486.

Bamber, J.L. (1994). Ice sheet altimeter processing scheme. *International Journal of Remote Sensing*, 15, 925-938.

Bell, J. W., Amelung, F., Ramelli, A. R., & Blewitt, G. (2002). Land subsidence in Las Vegas, Nevada, 1935–2000: New geodetic data show evolution, revised spatial patterns, and reduced rates. *Environ Eng Geosci*, 8 (3), 155–174.

Benveniste, J. (2002). ENVISAT RA-2/MWR product handbook, Issue 1.2, PO-TN-ESR-RA-0050, Frascati, Italy: European Space Agency.

Berardino, P., Fornaro, G., Lanari, R., & Sansosti, E. (2002). A new algorithm for surface deformation monitoring based on small baseline differential SAR interferograms. *IEEE Transactions on Geoscience and Remote Sensing*, 40 (11), 2375-2383.

Berry, P.A.M., Garlick, J.D., Freeman, J.A., & Mathers, E.L. (2005). Global inland water monitoring from multi-mission altimetry. *Geophysical Research Letters*, 32, L16401, doi:10.1029/2005GL022814.

Birkett, C.M. (1995). The contribution of TOPEX/POSEIDON to the global monitoring of climatically sensitive lakes. *Journal of Geophysical Research*, 100, 25179-25204.

Birkett, C.M. (1998). Contribution of the TOPEX NASA radar altimeter to the global monitoring of large rivers and wetlands. *Water Resources Research*. 34, 1223-1239.

Birkett, C.M., Mertes, L.A.K., Dunne, T., Costa, M.H., & Jasinski, M.J. (2002). Surface water dynamics in the Amazon Basin: Application of satellite radar altimetry. *Journal of Geophysical Research*, 107, doi:10.1029/2001JD000609.

Carruth, R. L., Pool, D. R., Anderson, C. E. (2007). Land subsidence and aquifer-system compaction in the Tucson Active Management Area, south-central Arizona, 1987–2005. U.S. Geological Survey Scientific Investigations Report 2007-5190, 27 p.

Costantini, M. (1998). A novel phase unwrapping method based on network Programming. *IEEE Transactions on Geoscience and Remote Sensing*, 36, 813-821.

Curlander, J. C., & McDonough R. N. (1991). Synthetic aperture radar: systems and signal processing, 1st edition. Wiley series in remote sensing and image processing, Publisher: Wiley-Interscience, Nov 1991.

Doren, R. F., Rutchey, K., & Welch, R. (1999). The Everglades: A perspective of the requirements and applications for vegetation map and database products, *Photogrammetric Engineering & Remote Sensing,* 65(2), 155-161.

Frappart, F., Calmant, S., Cauhopé, M., Seyler, F., & Cazenave, A. (2006). Preliminary results of ENVISAT RA-2-derived water levels validation over the Amazon basin. *Remote Sensing of Environment*, 100, 252-264.

Fraser, L.H. & Keddy, P.A. (2005). The world's largest wetlands: ecology and conservation. Cambridge University Press.

Freeman, A., & Durden, S.L. (1998). A three-component scattering model for polarimetric SAR data. *IEEE Transactions on Geoscience and Remote Sensing*, 36, 963-973.

Galloway, D. L., Hudnut, K. W., Ingebritsen, S. E., Phillips, S. P., Peltzer, G., Rogez F., & Rosen, P. A. (1998). Detection of aquifer-system compaction and land subsidence using interferometric synthetic aperture radar, Antelope Valley, Mojave Desert, California. *Water Resour Res*, 34, 2573–2585.

Galloway, D. L., Jones, D. R., & Ingebritsen, S. E. (2000). Measuring land subsidence from space. U.S. Geological Fact Sheet 051-00, 4 p.

Galloway, D. L., & Hoffmann, J. (2007). The application of satellite differential SAR interferometry-derived ground dis- placements in hydrogeology. *Hydrogeology Journal*, 15 (1), doi: 10.1007/s10040-006-0121-5, 133–154.

Goldstein, R.M., & Werner, C.L. (1998). Radar interferogram filtering for geophysical applications. *Geophysical Research Letters*, 25, 4035-4038.

Hanssen, R.F. (2001). Radar Interferometry: Data Interpretation and Error Analysis. Kluwer Academic Publishers.

Hess, L.L., Melack, J.M., & Simonett, D.S. (1990). Radar detection of flooding beneath the forest canopy: a review. *International Journal of Remote Sensing*, 11, 313-1325.

Hess, L.L., Melack, J.M., Filoso, S., & Wang, Y. (1995). Delineation of inundated area and vegetation along the Amazon floodplain with the SIR-C synthetic aperture radar. *IEEE Transactions on Geoscience and Remote Sensing*, 33, 896-904.

Hess, L.L., Melack, J.M., Novo, E.M.L.M., Barbosa, C.C.F., & Gastil, M. (2003). Dual-season mapping of wetland inundation and vegetation for the central Amazon basin. *Remote Sensing of Environment*, 87, 404-428.

Hoffmann, J., Zebker, H. A. (2003). Prospecting for horizontal surface displacements in Antelope Valley, California, using satellite radar interferometry. *J Geophys Res*, 108, (F1), 6011. http://dx.doi.org/10.1029/2003JF000055.

Jones, John W. (2011): Remote Sensing of Vegetation Pattern and Condition to Monitor Changes in Everglades Biogeochemistry, *Critical Reviews in Environmental Science and Technology*, 41:S1, 64-91.

Kasischke, E. S., Smith, K. B., Bourgeau-Chavez, L., L., Romanowicz, E. A., Brunzell, S., & Richardson, C. J. (2003). Effects of seasonal hydrologic patterns in south Florida wetlands on radar backscatter measured from ERS-2 SAR imagery, *Remote Sensing of Environment*, 88, 423-441.

Kim, J.-W., Lu, Z., Lee, H., Shum, C.K., Swarzenski, C. M., Doyle, T. W., Baek, S.-H. (2009). Integrated analysis of PALSAR/Radarsat-1 InSAR and ENVISAT altimeter data for mapping of absolute water level changes in Louisiana wetlands, *Remote Sensing of Environment*, 113 (11), 2356-2365, ISSN 0034-4257, 10.1016/j.rse.2009.06.014.

Kim, S.-W., Hong, S.-H., & Won, J.-S. (2005). An application of L-band synthetic aperture radar to tide height measurement, *IEEE Transactions on Geoscience and Remote Sensing*, 43(7), 1472-1478.

Kim, S.-W., Wdowinski, S., Amelung, F., Dixon, T. H., & Won, J.-S. (2013). Interferometric coherence analysis of the Everglades wetlands, south Florida, *IEEE Transactions on Geoscience and Remote Sensing*, in press.

Kwoun, O.-I. & Lu, Z. (2009). Multi-temporal RADARSAT-1 and ERS backscattering signatures of coastal wetlands in southeastern Louisiana, *Photogrammetric Engineering & Remote Sensing*, 75(5), 607-617.

Lanari, R., Mora, O., Manunta, M., Mallorquí, J. J., Berardino, P., & Snasosti, E. (2004). A small-baseline approach for investigating deformations on full-resolution defferential SAR interferograms. *IEEE Transactions on Geoscience and Remote Sensing*. 42 (7), 1377-1386.

Lee, H., Shum, C.K., Yi, Y., Braun, A., & Kuo, C.-Y. (2008). Laurentia crustal motion observed using TOPEX/POSEIDON radar altimetry. *Journal of Geodynamics*, 46, 182-193, doi:10.1016/j.jog.2008.05.001.

Lee, H., Shum, C.K., Yi, Y., Ibaraki, M., Kim, J.-W., Braun, A., Kuo, C.-Y., & Lu, Z. (2009). Louisiana wetland water level monitoring using retracked TOPEX/POSEIDON altimetry. *Marine Geodesy*, 32, 284-302.

López-Quiroz, P., Doin, M.-P., Tupin, F., Briole, P., & Nicolas, J.-M. (2009). Time series analysis of Mexico City subsidence constrained by radar interferometry, *Journal of Applied Geophysics*, 69, 1-15.

Lu, Z., & Danskin, W. (2001). InSAR analysis of natural recharge to define structure of a ground-water basin, San Bernardino, California, *Geophysical Research Letters*, 28, 2661-2664.

Lu, Z., Crane, M., Kwoun, O.-I., Wells, C., Swarzenski, C., & Rykhus, R. (2005). C-band radar observes water level change in swamp forests. *EOS*, 86, 141-144.

Lu, Z. (2007). InSAR imaging of volcanic deformation over cloud-prone areas – Aleutian Islands. *Photogrammatric Engineering & Remote Sensing*, 73, 245-257.

Lu, Z., & Kwoun, O.-I. (2008). Radarsat-1 and ERS InSAR analysis over southeastern coastal Louisiana: Implications for mapping water-level changes beneath swamp forests. *IEEE Transactions on Geoscience and Remote Sensing*, 46, 2167-2184.

Mitsch, W.J. & Gosselink, J.G. (2007). Wetlands, 4th ed. John Wiley & Sons, Inc., New York.

Morris, C.S., & Gill, S.K. (1994). Evaluation of the TOPEX/POSEIDON altimeter system over the Great Lakes. *Journal of Geophysical Research*, 99, 24527-24539.

Pepe, A., Sansosti, E., Berardino, P., & Lanari, R. (2005). On the generation of ERS/ENVISAT DInSAR time-series via the SBAS technique. *IEEE Geoscience and Remote Sensing Letters*, 2 (3), 265-169.

Pool, D. R. (2005). Variations in climate and ephemeral channel recharge in southeastern Arizona, United States. *Water Resources Research*, 41, W11403, doi:10.1029/2004WR003255, 24 p.

Pool, D. R., & Anderson, M. T. (2008). Ground-water storage change and land subsidence in Tucson Basin and Avra Valley, southeastern Arizona, 1998-2002. U.S. Geological Survey Scientific Investigations Report 2007-5275, 34 p.

Ramsey III, E.W. (1995). Monitoring flooding in coastal wetlands by using radar imagery and ground- based measurements, *International Journal of Remote Sensing*, 16(13), 2495-2502.

Ramsey III, E., Lu, Z., Suzuoki, Y., Rangoonwala, A., & Werle, D. (2011). Monitoring duration and extent of storm surge flooding along the Louisiana coast with Envisat ASAR data. *IEEE Geoscience and Remote Sensing*, 2:387-399.

Rosen, P., Hensley, S., Joughin, I.R., Li, F.K., Madsen, S.N., Rodriguez, E., & Goldstein, R.M. (2000). Synthetic aperture radar interferometry. Proceedings of IEEE, 88, 333-380.

Samsonov, S. (2010). Topographic correction for ALOS PALSAR interferometry. IEEE Transactions on Geoscience and Remote Sensing, 48(7), 3020-3027.

Samsonov, S., Beavan, J., Gonzalez, P., & Tiampo, K.J.F. (2011). Ground deformation in the Taupo Volcanic Zone, New Zealand observed by ALOS PALSAR interferometry. *Geophysical Journal International*, 187(1), 147–160.

Samsonov, S., & d′Oreye, N. (2012). Multidimensional time series analysis of ground deformation from multiple InSAR data sets applied to Virunga Volcanic Province. *Geophysical Journal International*, 191(3), 1095–1108.

Samsonov, S., d′Oreye, N., & Smets, B. (2013). Ground deformation associated with post-mining activity at the French-German border revealed by novel InSAR time series method. *International Journal of Applied Earth Observation and Geoinformation*, 23, 142-154.

Schmidt, D. A., & Bürgmann, R. (2003). Time-dependent land uplift and subsidence in the Santa Clara valley, California, from a large interferometric synthetic aperture radar data set. *Journal of Geophysical Research*, 108 (B9), 2416, doi:10.1029/2002JB002267.

SFWMD & FDEP (2012). South Florida environmental report: Volume 1. the South Florida Environment. Available at http://my.sfwmd.gov/portal/page/portal/pg_grp_sfwmd_sfer/portlet_prevreport/2012_sfer/v1/vol1_table_of_contents.html Accessed Oct 12, 2012.

Sheiber, R., & Moreira, A. (2000). Coregistration of interferometric SAR images using spectral diversity. *IEEE Transactions on Geoscience and Remote Sensing*, 38, 2179-2191.

Smith, L.C. (1997). Satellite remote sensing of river inundation area, stage, and discharge: a review. *Hydrological Processes*, 11, 1427-1439.

Tikhonov, A. N. & Arsenin, V. Y. (1977). Solution of Ill-Posed Problems, V. H. Winston and Sons, Washington, DC.

Tong, X., Sandwell, D. T., & Fialko, Y. (2010). Coseismic slip model of the 2008 Wenchuan earthquake derived from joint inversion of interferometric synthetic aperture radar, GPS, and field data, *Journal of Geophysical Research*, 115, B04314, doi:10.1029/2009JB006625.

Wang, Y., Hess, L.L., Filoso, S., & Melack, J.M. (1995). Understanding the radar back-scattering from flooded and nonflooded Amazonian forests: results from canopy backscatter modeling. *Remote Sensing of the Environment*, 54, 324-332.

Wdowinski, S., Amelung, F., Miralles-Wilhelm, F., Dixon, T., & Carande, R. (2004). Space-based measurements of sheet-flow characteristics in the Everglades wetland, Florida. *Geophysical Research Letters*, 31, L15503, doi:10.1029/2004GL020383.

Wdowinski, S., Kim, S.-W., Amelung, F., Dixon, T., Miralles-Wilhelm, F., & Sonenshein, R. (2008). Space-based detection of wetlands′ surface water level changes from L-band SAR interferometry, *Remote Sensing of Environment*, 112, 681-696.

Zweig, C. L. & Kitchens, W. M. (2008). Effects of landscape gradients on wetland vegetation communities: Information for large-scale restoration. *Wetlands*, 28 (4), 1086-1095.